

國立臺灣大學理工學院化學系

博士論文

Department of Chemistry

College of Science

National Taiwan University

Doctoral Dissertation

一維 II-VI 族半導體奈米材料

其形貌、自組裝與異質界面之合成及特性研究

Morphology, Self-Assembly, and Heterojunction of
One-Dimensional II-VI Semiconducting Nanocrystals



康佳正

Chia-Cheng Kang

指導教授：周必泰 博士

Advisor: Pi-Tai Chou, Ph.D.

中華民國 98 年 7 月

July, 2009

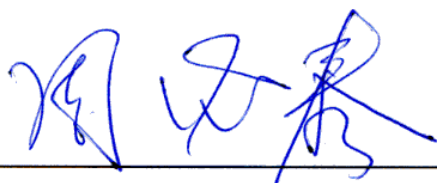
國立臺灣大學博士學位論文
口試委員會審定書

(論文中文題目) 一維 II-VI 族半導體奈米材料其形貌、自組裝與異質界面之合成及特性研究

(論文英文題目) Morphology, Self-Assembly, and Heterojunction of One-Dimensional II-VI Semiconducting Nanocrystals

本論文係 康佳正 君 (學號 F92223003) 在國立臺灣大學化學系完成之博士學位論文，於民國 98 年 7 月 23 日承下列考試委員審查通過及口試及格，特此證明。

口試委員：



(簽名)

(指導教授)

張 懿 平

林 萬 寧

傅 德 芝

蔣 景 中



系主任、所長

(簽章)

中文摘要

於奈米材料領域中，除零維奈米粒子（亦被稱為量子點）外，具有不同長寬比，且維度均在奈米尺度下之一維半導體奈米晶體亦受到大家的重視，原因在於這類一維奈米棒的光學以及電子特性均受到粒徑大小以及不同形狀的影響。在本論文中，於溶液態的環境下反應，可以在不外加方向控制手段的前提下合成大小為二平方微米之自組裝硫化鎘陣列。奈米棒的濃度、硫化鎘本身特性以及界面活性劑上的碳鍊均對自組裝陣列之形成有決定性的影響。另外，藉由控制界面活性劑之種類與反應溫度，可合成長寬比最大達到三百之硫化鎘奈米線。最後，引入金屬奈米粒子當作保護基，合成出軸向異質結構之鉑-硒化鎘-硫化鎘奈米棒。本論文之結果應可應用於設計及構築複雜性的異質奈米結構。

關鍵字：硒化鎘、硫化鎘、奈米線、奈米棒、異質結構。



Abstract

Besides zero dimensional semiconducting nanoparticles (also referred to as “quantum dots”), one dimensional semiconducting nanocrystals with dimensions in the range of nanometer and with different aspect ratios have also drawn much attention due to their fascinating size- and shape-dependent optical and electronic properties. In this study, by using a solution-based method, CdS self-bundled arrays with an area of as large as $2.0 \mu\text{m}^2$ could be produced in the absence of an external direction-controlling process. Matching in nanorod concentration, intrinsic properties of CdS, and the hydrocarbon chains of the surfactants between adjacent CdS rods play key roles in the self-assembly. Also, the self-bundled CdS nanorods exhibit optical emission nearly free from the defect-states. In addition, by optimizing the use of surfactants and temperature, the aspect ratio of CdS nanowires with diameter of 3.5 nm can be tuned up to 300. Finally, by applying metallic nanoparticles as a protecting group, nanorods with axial heterojunctions could be obtained with a mechanism different from that of the SLS model. Results of this study could serve as basic concepts in nanocrystal architecture.

Key words: CdSe, CdS, Nanorod, Nanowire, Heterostructure

Table of Contents

口試委員會審定書	i
中文摘要	ii
Abstract	iii
Table of Contents	iv
List of Figures	vii
Chapter 1. Growth Mechanism of One-Dimensional II-VI Semiconducting Nanomaterials	
1. Intorduction	1
2. Effective-Monomer and Selective-Adsorption Model	3
3. Oriented-Attachment Model	11
4. Solution-Liquid-Solid Model	13
5. Motivation	15
6. References	16
7. Figures	21
Chapter 2. Characterization Techniques	
1. Transmission Electron Microscopy (TEM)	33
2. Ultraviolet-visible spectroscopy (UV/Vis)	36
3. Steady-State Fluorescence	38
4. X-Ray Diffraction (XRD)	40
5. Confocal Microscopy	42
6. Pendant Drop Method	43
7. References	44
8. Figures	46

Chapter 3. 2D Self-Bundled CdS Nanorods with Micrometer

Dimension in the Absence of External Directing Process

TOC & Abstract	49
1. Intorduction	50
2. Experimental Section	54
3. Results and Discussion	56
4. Conclusion	68
5. Acknowledgment	69
6. References	69
7. Figures	73

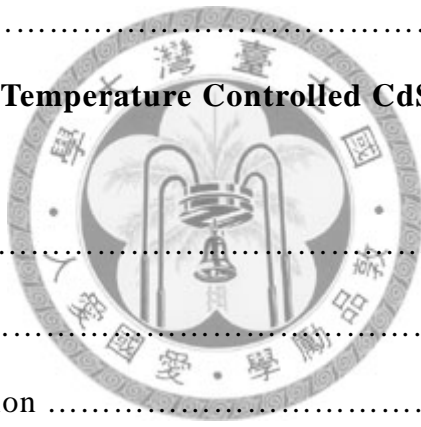
Chapter 4. Surfactant/Temperature Controlled CdS Nanowires

Formation

TOC & Abstract	87
1. Intorduction	88
2. Experimental Section	89
3. Results and Discussion	91
4. Conclusion	96
5. References	97
6. Figures	100

Chapter 5. Axial Heterostructured Pt-CdSe-CdS Semiconducting Nanorods

TOC & Abstract	104
1. Intorduction	105



2. Experimental Section	108
3. Results and Discussion	111
4. Conclusion	119
5. References	119
6. Figures	126
Chapter 6. Concluding Remarks.....	132



List of Figures

Chapter 1. Growth Mechanism of One-Dimensional II-VI Semiconducting Nanomaterials

- Figure.1** Top: Size-dependence of the surface atom ratio and the relative chemical potential of CdSe nanocrystals, assuming a spherical shape. Bottom: Shape-dependent chemical potential of CdSe quantum rods. The volume of all nanocrystals is set to the same value as of an 8 nm CdSe dot..... 21
- Figure.2** Influence of the history of Cd-TDPA complexes. Left panel: Without aging at room temperature. Right panel: Aged at room temperatures. TEM pictures were taken with the aliquots with the highest average aspect ratio in each reaction..... 22
- Figure.3** Schematic illustration of the size- and configuration-dependence of the relative chemical potential of crystals/clusters in the extremely small size regime. Inset: Structure of Cd₁₇. The magic sized nanocluster observed may likely possess a similar structure..... 23
- Figure.4** The temporal shape evolution of CdSe nanocrystals determined by TEM and the corresponding temporal variation of Cd monomer concentration in solution determined by ICP..... 24
- Figure.5** The three growth stages of elongated CdSe nanocrystals at different monomer concentration windows..... 25
- Figure.6** The unique chemical reactivity of the (001) facet of the wurtzite CdSe nanocrystals..... 25

Figure.7 TEM images of CdTe nanowires made from 3.4 (A) and 5.4 nm (B) nanoparticles. Bars, 100 nm.....	26
Figure.8 (A) TEM image of intermediate state of nanoparticle-nanowire transition for 5.4-nm nanoparticles. (B) The enlarged portion of the chain, with short rods marked by arrows. (C) The high-resolution TEM image of the adjacent nanoparticles in the chain. The "pearl necklace" aggregates were not observed in the standard dispersions of CdTe.....	27
Figure.9 High-resolution TEM of nanowires made from (A) orange- and (B) red-emitting CdTe quantum dots. The insets show the corresponding diffraction patterns for (001) and (100); vectors of the crystal lattice are indicated by thick arrows. Energy dispersive x-ray spectroscopy showed identical chemical composition in respect to Cd and Te for both nanoparticles and nanowires.....	28
Figure.10 (a) Structure of $\{t\text{-Bu}_2\text{In}[\text{P}(\text{SiMe}_3)_2]\}_2$; (b) under conditions allowing the imaging of the In-catalyst droplets (arrows); (c) from a higher-temperature synthesis employing added In catalyst.....	29
Figure.11 Growth mechanisms for pseudo-1D crystalline morphologies: (a) VLS mechanism proposed by Wagner and Ellis for growth under CVD conditions; (b) SLS mechanism proposed by Buhro and co-workers for analogous growth from solution.....	29
Figure.12 TEM images of near-monodisperse Bi nanoparticles obtained by thermal decomposition of $\text{Bi}[\text{N}(\text{SiMe}_3)_2]_3$ with $\text{Na}[\text{N}(\text{SiMe}_3)_2]$. The quantity following the \pm symbol is the standard deviation in the diameter distribution, expressed as a percentage of the mean diameter. Mean diameter = (a) 6.4 nm \pm 11.5%, (b) 15.1 nm \pm 5.6%, and (c) 25.2 nm \pm	

5.1%..... 30

Figure.13 Plots of nanowire diameter vs initial catalyst nanoparticle diameter for SLS-grown wires. The lines are least-squares fits to the data, which are identified in the inset legend. The dotted lines correspond to nanowires grown from In-catalyst nanoparticles. Legend format: nanowire composition-surfactant-catalyst nanoparticle. HAD = n-hexadecylamine, TOPO = tri-n-octylphosphine oxide, TOP = tri-n-octylphosphine, OPA = n-octylphosphonic acid, MA = myristate, SA = stearate, and polymer = poly(1-hexadecene-co-vinylpyrrolidinone) for InP and poly(1-diphenylphosphinomethyl-4-vinylbenzene) / poly(1-hexadecene-co-vinylpyrrolidinone) mixtures for GaAs..... 31

Figure.14 TEM images of SLS-grown III-V nanowires and the corresponding diameters. (a) InP, $11.2 \text{ nm} \pm 17.5\%$, (b) GaAs, $7.0 \text{ nm} \pm 12.7\%$, and (c) InAs, $5.3 \text{ nm} \pm 12.4\%$ 32

Figure.15 TEM images of SLS-grown II-VI nanowires and the corresponding diameters. (a) CdSe, $5.3 \text{ nm} \pm 14.4\%$, (b) ZnTe, $7.6 \text{ nm} \pm 13.8\%$, and (c) CdTe, $9.7 \text{ nm} \pm 20.6\%$ 32

Chapter 2. Characterization Techniques

Figure.1 An illustration of a typical TEM system..... 46

Figure.2 Ray paths through a magnetic prism spectrometer showing (A) dispersion and focusing of the electrons in the plane of the spectrometer and (B) the lens-focusing action in the plane normal to the spectrometer; compare the nonfocusing action of a glass prism on visible light (inset)... 46

Figure.3 A conventional spectrofluorometer..... 47

Figure.4 Basic features of typical XRD experiment..... 47

Figure.5 Schematic diagram of the optical pathway and principle components in a basic confocal microscope.....	48
Figure.6 Schematic diagram of the pendant drop apparatus.....	48
Chapter 3. 2D Self-Bundled CdS Nanorods with Micrometer Dimension in the Absence of External Directing Process	
Figure.1 (a) TEM image of TDPA and TOP capped CdS nanorods with self-assembled organization in large scale. The inset shows the diffraction pattern of the bundle. (b) TEM image of bundled-up CdS nanorods in higher magnification. (c) An extended TEM image of self-assembled CdS nanorods.....	73
Figure.2 Contrast-enhanced Fourier filtered micrograph of the same region in Figure 1a. The dots are the bundled CdS nanorods standing on the copper grid, and the stripe patterns are the leaning nanorods.....	74
Figure.3 An extended TEM image of self-assembled CdS nanorods synthesized with TDPA and TOP.....	75
Figure.4 TEM image of TDPA and TOP capped CdS nanorods with concentrations of (a) 2.5 and (b) 0.5 in weight percent.....	76
Figure.5 The surface energy, measured by pendent drop method, with respect to different concentrations of CdS nanorods. (0, 0.4, 0.8, 1.5, 3.125, and 6.25 weight percent).....	77
Figure.6 Powder X-ray diffraction (XRD) of CdS nanorods synthesized by using (a) TDPA and TOP, (b) TDPA, HDA, and TOP, and that of standard CdS (wurtzite) pattern (lower).....	78
Figure.7 TEM image of TDPA, HDA, and TOP capped CdS nanorods with concentration of 2.0% weight percent (see text for detail).....	79

Figure.8 The normalized emission spectra of (a) CdS nanorods (synthesized by using TDPA and TOP) solution. (b) peripheral and (c) central region of a single array in the deposited thin film measured by a confocal microscope. The excitation wavelength is 406 nm (GaN laser) for all measurements..... 80

Figure.9 TEM image of a monolayer of CdS nanorods in the hole of a Quantifoil grid..... 81

Figure.10 Proposed model of self-assembled CdS arrays synthesized by using TDPA and TOP as surfactants..... 82

Figure.11 Drawings that illustrate the corralling behavior of CdS nanorods upon the evaporation of solvent on (a) Formvar grid and (b) Quantifoil grid..... 83

Figure.12 TEM images of CdS nanorods synthesized by using (a) ODPA, TOPO, and TOP and (b) ODPA and TOP..... 84

Figure.13 Proposed model of formation of CdS nanorods synthesized by using (a) ODPA, TOPO, and TOP and (b) ODPA and TOP..... 85

Figure.14 TEM images of CdS nanorods synthesized by using (a) OPA, TOPO, and TOP and (b) OPA and TOP..... 86

Chapter 4. Surfactant/Temperature Controlled CdS Nanowires Formation

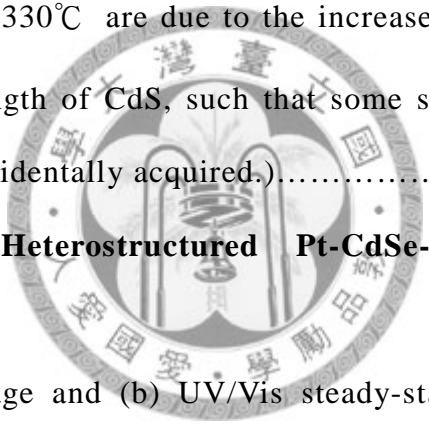
Figure.1 TEM images of CdS nanocrystals synthesized under different temperatures of (a) 280°C, (b) 315°C, (c) 320°C and (d) 330°C 100

Figure.2 Powder X-ray diffraction (XRD) of CdS nanocrystals synthesized under 320°C (upper) and that of standard CdS (wurtzite)

pattern (lower)..... 101

Figure.3 A prototype of CdS nanowires synthesized under 330°C . HRTEM image (inset) clearly shows the junction of bipod that consists with a zinc-blende core with wurtzite arms epitaxially grown from the {111} plane of the core..... 102

Figure.4 (a) absorption and (b) emission spectra of CdS nanocrystals synthesized under different temperatures. Solvent: toluene. The excitation wavelength was fixed at 400 nm for all emission spectra. (note: The multiple peaks at longer wavelength of the defect emission prepared at 320°C and 330°C are due to the increase of scattering light upon increasing the length of CdS, such that some stray light from the excitation lamp was accidentally acquired.)..... 103



Chapter 5. Axial Heterostructured Pt-CdSe-CdS Semiconducting Nanorods

Figure.1 (a) TEM image and (b) UV/Vis steady-state absorption and emission spectra of CdSe nanocrystals..... 126

Figure.2 (a) TEM image and (b) HRTEM image of Pt-CdSe nanocrystals. (inset: selected area EDS spectrum of this image.)..... 127

Figure.3 TEM images of nanocrystals synthesized by using (a) TDPA, and TOP. (b) stearic acid and TOP..... 128

Figure.4 (a) TEM image of Pt-CdSe-CdS nanocrystals synthesized by using oleic acid, ODE, and TOP. (b) UV/Vis steady-state absorption spectra of CdSe, Pt-CdSe, and Pt-CdSe-CdS nanocrystals..... 129

Figure.5 (a) HRTEM image of a Pt-CdSe-CdS heterostructured nanorod

synthesized by using oleic acid, ODE, and TOP as surfactants. The inset shows EDS results of (1) head and (2) tail part of the hybrid nanorod. (b) Se and (c) S mapping done by using EELS measurements..... 130

Figure.6 TEM image of Pt-CdSe-CdS nanocrystals synthesized by using oleic acid, ODE, and TOP for 1 hour..... 131



Chapter 1.

Growth Mechanism of One-Dimensional II-VI Semiconducting Nanomaterials

1. Introduction

Nanomaterials, materials made with dimensions on a scale of 1 - 100 nm, is one of the most interesting subjects in the field of chemical research. Among the inorganic nanomaterials, semiconducting nanocrystals have attracted considerable attention mainly due to the significance of size-tunable optical properties.¹⁻⁵ These size-dependent phenomena make semiconducting nanocrystals good candidates in a wide range of technological applications, such as lasing,⁶ electroluminescence,^{7,8} photovoltaics,^{9,10} and nanoelectronics.^{11,12}

In addition to particle size, shapes of nanocrystals also have influence on the optical and electronic properties. For example, one dimensional nanocrystals, several nanometers in diameter and with different aspect ratios, has shown unique linear polarized emission along the *c*-axis of crystals because of intrinsic dipolar structure.¹³⁻¹⁷ Therefore, understanding of shape-evolution and growth mechanism of semiconducting nanocrystals is necessary while designing and synthesizing the tailored nanostructure.

Considering the crystal growth, the most widely cited classical model for shape control of crystals is based on thermodynamics, namely Wulff facets argument, or Gibbs-Curie-Wulff theorem.¹⁸ Small crystals have substantial numbers of surface atoms compared to atoms in a bulk-like environment, and hence the energy contribution of surfaces to the total energy of a nanocrystal is significant. In this theory, shape of a crystal is thermodynamically determined by the relative chemical potential of all possible crystallographic facets. The final crystal shape is decided in a way such that the total free energy of the system is minimized. However, being based on thermodynamics, shape evolution is not allowed. Furthermore, this theory cannot account for kinetically trapped morphologies, for example, this thermodynamic argument cannot explain the frequently observed shape evolution via high-temperature routes and rapid quenching methods to stabilize a metastable form.

As a result, a new framework is needed for the development of shape-controlled synthesis of colloidal nanocrystals. Several research groups in the world have made a lot of efforts to reasonably explain shape evolution of nanocrystals, especially one-dimensional semiconducting nanomaterials. In the following sections, four different kinds of proposed mechanisms and the corresponding synthetic routes in solution phase will be discussed, namely, effective-monomer model, selective-adsorption model, oriented-attachment model, and solution-liquid-solution model.

2. Effective-Monomer and Selective-Adsorption Model

In 2000, Alivisatos and the coworkers reported the formation of elongated CdSe nanocrystals with their short axes smaller than the quantum-confined dimension of the given material – CdSe quantum rods.¹³ They also observed the unique-axis polarized emission from the CdSe nanorods. From 2000 to 2003, a great deal of tailored experiments has been made to construct a general model for the growth mechanism of quantum rods.¹⁹⁻²³ In their studies, the so-called “high-temperature organometallic routes” were applied to synthesize anisotropic nanocrystals. During the synthesis, selenium powder and organometallic cadmium precursor, namely dimethyl cadmium, were co-dissolved in a tri-alkyl phosphine (-butyl or -octyl). Subsequently, the solution was injected into hot (340 – 360 °C) trioctyl phosphine oxide (TOPO).¹³ Nucleation occurred rapidly, followed by growth of nanorods (280 – 300 °C). Right after these reports,^{13,19,20} Peng *et al.* found that the organometallic cadmium precursor is not necessary. In substitution, cadmium oxide (CdO) and alkylphosphonic acid, such as hexylphosphonic acid (HPA) and tetradecylphosphonic acid (TDPA) were used in the reaction.²¹ Since then, this set of materials, namely, cadmium oxide (CdO), alkylphosphonic acid (tetradecyl (TDPA) and hexyl (HPA)), tri-alkyl phosphine (-butyl (TBP) or -octyl (TOP)), and trioctyl phosphine oxide (TOPO), has been viewed as the most broadly accepted precursor in the synthesis of nanorods.

Formation of crystals is constituted by nucleation and growth. Initially, as reported by Alivisatos and the coworkers,¹³ high monomer concentration is a critical condition in the growth of nanorods, which is known as the “effective-monomer model”. Also, as shown in the experiments done by the same group,¹⁹ addition of second kind of surfactant, namely hexylphosphonic acid (HPA), would help the formation of anisotropic nanocrystals because of different adsorption ability on the desired crystallographic faces of these surfactants. Therefore, variation of growth rate on different facets could be achieved. This is known as the “selective-adsorption model”.

Bearing the above-mentioned concepts in mind, in 2001, Peng *et al.* started digging out the origin of nanorod growth.^{20,22} As shown in Figure 1,²² from the Gibbs-Thompson equation,¹⁸ for dot-shaped crystals, their relative chemical potential is plotted in the upper part, indicating a strong size-dependent response of the chemical potential. The shape effect, such as different aspect ratios, on the relative chemical potential of nanocrystals is plotted in lower part of Figure 1. The chemical potential doubled when CdSe crystal is elongated from a dot to a rod with aspect ratio of 30, which implies the necessity of a high chemical potential environment as well as high monomer concentration during the growth of elongated nanocrystals.

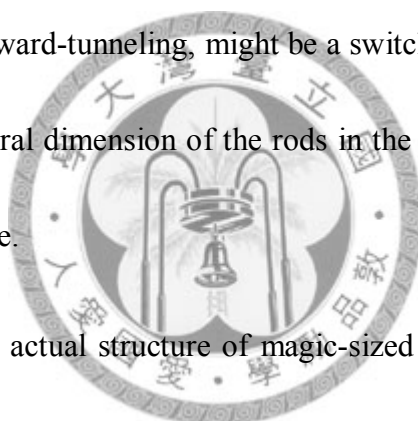
Combining experimental and theoretical approaches, Peng and coworkers found that nucleation process in the growth of nanorods takes place through the presence of

“magic sized nanocluster”,²² those CdSe clusters with defined molecular structures in the size range between 1 and 2 nm. Typically, these clusters contain no more than one unit cell of the bulk crystal and possess close-shell structures.²⁴ Because of the close-shell configuration, these nanoclusters are thermodynamically more stable than those without a close-shell structure. Therefore, magic sized nanoclusters appear always at fixed and discrete sizes.

Experimentally, magic sized nanoclusters of semiconductors can be detected by the appearance of sharp absorption peaks at persistent and isolated positions. By monitoring the UV/Vis absorption spectra of the middle-tip aliquots taken from the reaction flask at given time intervals, as shown in Figure 2, two absorption peaks were recorded at about 285 nm and 349 nm. The peak at 349 nm is also reported by Soloviev *et al.*, which is attributed to CdSe clusters containing 17 Cd atoms.²⁴ Thus the appearance of a magic sized nanoclusters is confirmed. The other absorption feature observed at about 285 nm, which is not very sharp and lasts normally for the entire growth course, should be something significantly smaller than a cluster with eight cadmium atoms.²⁴ Because of the exceptionally high absorption energy, it might be a CdSe molecule, instead of a magic sized nanocluster.

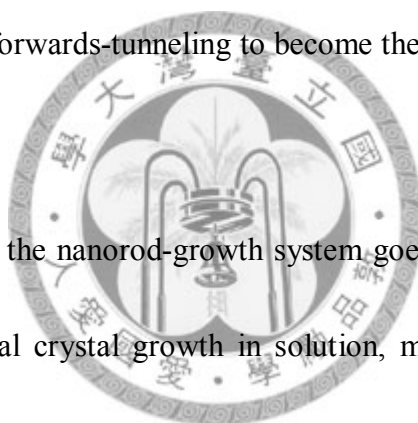
Magic sized nanocluster might have local minimum chemical potential because of their close-shell configurations. Certainly, the Gibbs–Thompson equation is no longer

valid in this size regime. Schematically, Figure 3 illustrates the size- and configuration-dependent chemical potential in this extremely small size regime. The inevitable formation of magic sized nanoclusters in the nucleation stage likely plays a key role in determining the nature of all of the following events, and the size/shape of the resulting nanocrystals. Since the lateral dimension is always uniform regardless of the distribution of the aspect ratio, there should be only one kind of limited-sized magic sized nanoclusters. The “tunneling” through the lower thermodynamic barrier toward larger sizes, denoted as forward-tunneling, might be a switching-on step at the initiation of the rod growth. The lateral dimension of the rods in the 1D-growth mode is thus set as a more or less fixed value.



When it comes to the actual structure of magic-sized nanoclusters, some reports, containing the identified molecular (crystal) structures of magic-sized nanoclusters of cadmium chalcogenides, have also been published.²⁴⁻²⁷ Surprisingly, the core of all nanoclusters has a tetrahedral closed-shell configuration and a zinc blend structure, irrespective of the growth temperature. Peng *et al.* tentatively suggested that the magic-sized nuclei formed in their reactions also have a tetrahedral closed-shell configuration and a zinc blend core.²² This assumption is consistent with the observed formation of branched nanostructures.^{19,28} Experimental results of high-resolution transmission electron microscopy (HRTEM) revealed that the branching point is always

tetrahedral core with zinc blende structure, even though the rest of the nanocrystals is mostly of wurtzite structure. It is likely that the structure and morphology of the magic-sized nanoclusters are arrested at those branching points. Furthermore, the results also showed that the branched structures are more likely to appear at lower growth temperatures,^{22,28} which is consistent with the fact that, for CdSe, the zinc blende structure is more stable at lower temperature. Presumably, a phase transition to wurtzite structure may easily take place at higher temperatures when the magic-sized nanoclusters go through a forwards-tunneling to become the real seeds for the growth of the elongated structures.



After the nucleation, the nanorod-growth system goes into the next step, namely shape evolution. For typical crystal growth in solution, monomers diffuse from bulk solution and approach the area right next to the surface of a crystal, and then they react with the surface of the crystal. The so-called “diffusion-controlled process” is suitable for explaining the anisotropic growth of CdSe nanorods. As concluded by Peng and the coworkers,²⁰ a typical temporal shape evolution of CdSe quantum rods occurs in three distinguishable stages, as shown in Figure 4. Firstly, “1D-growth stage”, when the Cd monomer concentration in the solution is between 1.4 % and 2 % of cadmium by mass, all the nanocrystals grow almost exclusively along their long axis and both aspect ratio and volume of crystals increased rapidly. Secondly, “3D-growth stage”, as the Cd

monomer concentration dropped to between 0.5 % and 1.4 %, crystals grow simultaneously in three dimensions. The aspect ratio remains constant, but the crystal volume increases. Finally, “1D-to-2D-ripening”, when the Cd concentration is constant at 0.5 %, the aspect ratio decreases noticeably, because the dimension of the crystals increases along the short axis and decreases along the long axis. In addition, volume of nanocrystals remains constant, and there is no apparent net growth or dissolution of nanocrystals. This indicates that the monomers very likely move on the surface of a crystal from one dimension (c-axis) to the other two dimensions in an intraparticle manner. In the 1D-to-2D-ripening process, the quantum rods can eventually evolve to dot shape, if given enough time.

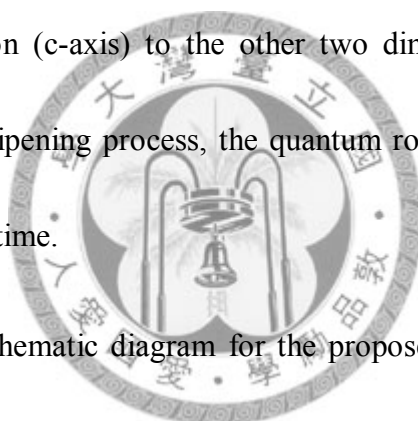


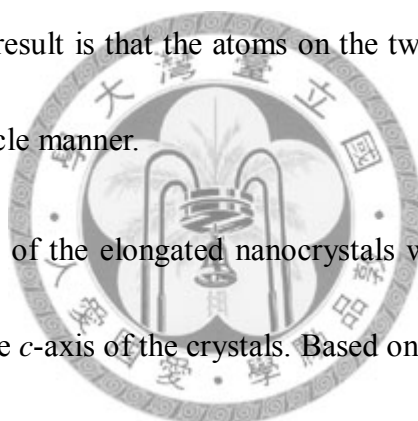
Figure 5 denotes a schematic diagram for the proposed mechanisms of the three stages of the shape evolution. The circle in each stage is the interface between the bulk solution and the diffusion sphere, and arrows indicate the diffusion directions of the monomers. In the 1D-growth stage, when the monomer concentration in the bulk solution is high, the chemical potential of the monomers in the bulk solution is significantly higher than that in the stagnant solution at any facets of the crystals, which means that monomers should diffuse into the diffusion sphere. Therefore, the volume of nanocrystals increases noticeably (see Figure 4). However, the unique structural feature of the (001) facet and the high chemical potential on both unique facets makes the

growth reaction rate along the c-axis much faster than that along any other axis. The limited amount of monomers maintained by diffusion is mainly consumed by the quick growth of the unique facets, especially the (001) facet. As a result, the diffusion flux goes to the c-axis exclusively and forms long axis of quantum rods. In this specific stage, the reactivity of different facets plays an important role. However, this stage is still diffusion controlled because the amount of diffusion flux is sufficient for the quick growth along the unique axis.

At the 3D-growth stage, as the monomer concentration drops to a certain level, the lower chemical potential gradient between the bulk solution and the different facets slows down the growth, with slower crystal volume increases as an indicator, compared to the 1D-growth. Further, this gradient drop impacts the unique facets the most, due to their relatively high chemical potential with respect to the other facets. Smaller gradient between surface of the unique facets and the bulk solution makes the diffusion flux difficult to go into the unique facets. Consequently, the monomers entering the diffusion sphere are shared by all three dimensions.

In the 1D-to-2D-ripening stage, the chemical potential of the monomers in the bulk solution drops to a level lower than that of the two unique facets, but still higher than that of the other surfaces. Overall, the chemical potential in the bulk solution approximately equals the average chemical potential of the entire surface atoms of a

nanocrystal. This leads to an equilibrium at interface between bulk solution and diffusion sphere, which explains that why both the volume of nanocrystals and the monomer concentration in the bulk solution remain constant. Without incoming diffusion flux, the monomers start to diffuse from the surface of the unique facets to the stagnant solution of the other facets because of the internal chemical potential gradient. Consequently, atoms on the unique facets dissolve into their stagnant solution to maintain the solubility equilibrium. The same equilibrium drives the other facets to take monomers from their stagnant solution. The net result is that the atoms on the two unique facets move to the other facets in an intraparticle manner.



Besides, the long axis of the elongated nanocrystals with a wurtzite structure has always been observed as the c -axis of the crystals. Based on the crystal structure and the surface coordination of the ligands, as shown in Figure 6, a qualitative explanation is proposed.²⁰ Firstly, a permanent dipole is along the c -axis of the wurtzite structure, and for any cadmium atoms exposed on the (001) facet, there are always three dangling bonds for each cadmium atoms. Secondly, since all ligands in the system are for cationic species, the (001) facets, if terminated with selenium atoms, should be nearly uncoated. These two facts make the (001) facet to be chemically more active than the other facets. As the monomer concentration is high enough, namely in the 1D-growthstage, the resulting nanocrystals would be rod-shaped.

3. Oriented-Attachment Model

In 2002, the group of Kotov reported formation of CdTe nanowires starting from the nanodots of CdTe in aqueous phase.²⁹ After the study of the growth mechanism, they also published several papers about applications of the as-prepared CdTe nanowires.³⁰⁻³² For the experimental condition, the CdTe nanodots were synthesized by using $\text{Cd}(\text{ClO}_4)_2$, NaHTe, and the stabilizing agent, such as 1-thioglycerol. The solution was refluxed at 96 °C for 48h to promote the growth of CdTe nanocrystals.

After the synthesis of CdTe nanodots, the key step of obtaining nanowires is the removal of excess stabilizer. To accomplish this requirement, CdTe nanoparticles were precipitated by methanol and redissolved in pure water at pH 9.0. The obtained dispersion was allowed to age in darkness at room temperature for several days. The TEM images of final product, CdTe nanowires, are shown in Figure 7.²⁹ During the dot-to-wire transformation, the intermediate state, “pearl necklace” aggregation, are also observed, as shown in Figure 8.²⁹ The presence of short nanorods among the “pearl” beads indicates that the nanowires formed not through point-initiated vectorial growth but rather by the recrystallization of multiple nanoparticles in a linear aggregate that fused gradually into one crystal. The crystal structure of the as-synthesized nanodots is zinc blende. However, the HRTEM results, as shown in Figure 9,²⁹ reveal that the CdTe

nanowires possess a wurtzite structure. The lattice plane spacings calculated from the diffraction patterns, showing a typical type of hexagonal wurtzite CdTe structure, are 3.98 angstrom and 2.29 angstrom for (100) and (110) facets, respectively. Therefore, the nanowire growth is obtained by a phase transition.

Based on experimental observations, Kotov and the coworkers proposed a mechanism, called “oriented attachment”, to rationally explain the growth of CdTe nanowires. During the controlled surfactant-detachment process, the CdTe nanoparticles reorganize their lattice to obtain a match between the symmetry of the crystal and the uniaxial geometry of 1D species. The chain aggregation is initiated by the overall decrease of the stabilizer concentration, which results in the shift of the dynamic equilibrium between nanoparticle-bonded and free stabilizer toward its dissolved state. This kind of attachment can lead to the formation of twin faces or other interfaces with structures distinct from that of bulk. These structurally different regions can serve as nucleation sites for new phases. The diameters of the nanowires and the nanoparticles were similar, further confirming the oriented attachment model. The existence of such a pearl necklace aggregate suggests that an understanding of the growth process will depend on collective behaviors of nanoparticles and the intermolecular forces between them.

The force capable of producing chains of nanocrystals is believed to be the

dipole-dipole attraction. The magnitude of the II-VI quantum dot dipoles was experimentally determined to be very high for both hexagonal and cubic nanocrystals, which is attributed to charging chalcogen surface states.³³ For CdSe (hexagonal) and ZnSe (cubic) nanocrystals the dipole moments are as high as 64 D and 42 D, respectively.³³ Even without additional polarizability terms, the attractive forces can be as high as 10 kJ/mole, which is substantially higher than the energy of regular molecular dipole-dipole attractions (~1.5 kJ/mole).

4. Solution-Liquid-Solid Model



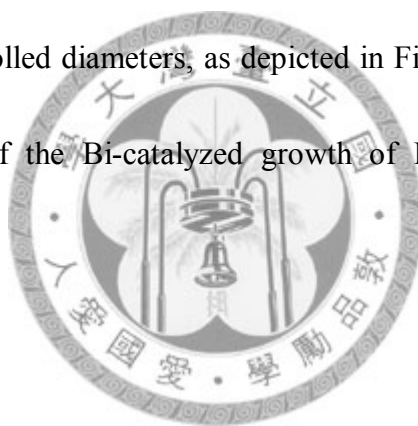
In the early 1990s, during the synthesis of the InP nanodots by using single precursor, $\{t\text{-Bu}_2\text{In}[\text{P}(\text{SiMe}_3)_2]\}_2$ (the structure is shown in Figure 10), Buhro *et al.* accidentally found the presence of metallic In on the end of as-synthesized InP fibers,³⁴⁻³⁶ as shown in Figure 10. Based on the observation, in 1995, they proposed a mechanism that the nanowires are grown according to a catalyzed mechanism, named the “solution-liquid-solid” (SLS) mechanism.³⁷ The SLS mechanism is an analogy to the previously discovered vapor-liquid-solid (VLS) mechanism.³⁸ The schematic illustration of VLS and SLS mechanism are shown in Figure 11(a) and (b), respectively.³⁹

In the VLS mechanism, under chemical vapor deposition (CVD) conditions, Si whiskers could be grown on Au-decorated Si substrates. At the elevated temperature of a CVD reactor, Gold particles deposited on Si melt to Au droplets. The dissolution of elemental Si into the Au droplet takes place while admission of a gaseous mixture of SiCl_4 and H_2 . A crystalline Si whisker is nucleated at the droplet–substrate interface when concentration of Si in a droplet reaches supersaturation, and therefore results in preferential reaction at the Au–droplet interface (Figure 11a). Owing to the the most active crystal-growth environment at the droplet–substrate interface, the growth of whisker naturally acquires a pseudo-one-dimensional (1D) morphology and continues growing until the precursor delivery is discontinued. The Au droplet catalyzes whisker growth in part by functioning as a crystallization solvent. In Figure 11b, for a VLS-like behavior, Buhro *et al.* thus named the SLS mechanism to distinguish between precursor delivery from solution and the vapor phase.³⁷

The choice of catalytic droplets is the key point due to the dual role in the system, namely for precursor adsorption and decomposition. Melting points, solvating abilities, and reactivities are the important criteria for judging suitable metals or metal alloys in SLS reaction.³⁹ First, Catalyst particles must be molten under the reaction conditions (200 – 300 °C). Second, to achieve supersaturation, at least one of the components in the precursor must have finite but limited solubility in the catalyst material. Finally, the

catalyst should not react with the target product (unless the catalyst material is the same as one of the constituent elements of the semiconductor).³⁹

Accordingly, Buhro and the coworkers found the Bi nanoparticle, synthesized by the thermal decomposition of $\text{Bi}[\text{N}(\text{SiMe}_3)_2]_3$ in the presence of $\text{Na}[\text{N}(\text{SiMe}_3)_2]$ (see Figure 12),³⁹ is the most suitable candidate for SLS mechanism. This method affords nanoparticles in the diameter range of 4–40 nm, with homogeneous size distribution at each diameter. The nearly monodispersed Bi nanoparticles can help to produce nanowires with well-controlled diameters, as depicted in Figure 13.³⁹ Figure 14 and 15 show the TEM images of the Bi-catalyzed growth of III-V and II-VI nanowires, respectively.³⁹



5. Motivation

After literature reviewing about different kinds of growth mechanism for 1D nanorods, some equivocal points arise in our mind. Firstly, the function of surfactants in section 2, effective-monomer and selective-adsorption model, is only mentioned to adsorb on the surface of nanorods and maintain the initial monomer concentration. However, after the growth, alkylchains on these adsorbed surfactants might have influence on final appearance of as-synthesized nanorods, such as secondary structure

and self-assembled behavior, in which the building blocks are those nanorods. In addition, mixture of different kinds of surfactants is thought to be necessary for producing uniform-shaped nanorods. This protocol would average the characteristics of each kind of surfactant. Furthermore, besides precursor, temperature dependence in reaction is seldom discussed in previous papers, which might tune the results of nanorods synthesis. Finally, based on the SLS mechanism, continuous growth of different semiconducting nanomaterials could be achieved, such as the quantum wires with axial heterojunctions and hyperbranched structure.^{40,41} We start to think that if the second nanomaterial in axial heterojunctions could be grown in different manners. In other words, it is possible that the nanoparticles on one side of nanorods serve as protecting group, blocking one end of the composite nanorods, and subsequently, second segment of nanorods could be grown on the unprotected side of nanorods. Bearing the above-mentioned statements in mind, experimental results and discussion of designed strategy are provided in the following chapters.

6. References

- (1) Brus, L. E. *J. Chem. Phys.* **1984**, *80*, 4403-4409.

- (2) Murray, C. B.; Norris, D. J.; Bawendi, M. G. *J. Am. Chem. Soc.* **1993**, *115*, 8706-8715.
- (3) Alivisatos, A. P. *J. Phys. Chem.* **1996**, *100*, 13226-13239.
- (4) Alivisatos, A. P. *Science* **1996**, *271*, 933-937.
- (5) Markovich, G.; Collier, C. P.; Henrichs, S. E.; Remacle, F.; Levine, R. D.; Heath, J. R. *Acc. Chem. Res.* **1999**, *32*, 415-423.
- (6) Klimov, V. I.; Mikhailovsky, A. A.; Xu, S.; Malko, A.; Hollingsworth, J. A.; Leatherdale, C. A.; Eisler, H. J.; Bawendi, M. G. *Science* **2000**, *290*, 314-317.
- (7) Tessler, N.; Medvedev, V.; Kazes, M.; Kan, S. H.; Banin, U. *Science* **2002**, *295*, 1506-1508.
- (8) Bakueva, L.; Musikhin, S.; Hines, M. A.; Chang, T. W. F.; Tzolov, M.; Scholes, G. D.; Sargent, E. H. *Appl. Phys. Lett.* **2003**, *82*, 2895-2897.
- (9) Huynh, W. U.; Dittmer, J. J.; Alivisatos, A. P. *Science* **2002**, *295*, 2425-2427.
- (10) McDonald, S. A.; Konstantatos, G.; Zhang, S.; Cyr, P. W.; Klem, E. J. D.; Levina, L.; Sargent, E. H. *Nat. Mater.* **2005**, *4*, 138-142.
- (11) Duan, X. F.; Huang, Y.; Cui, Y.; Wang, J. F.; Lieber, C. M. *Nature* **2001**, *409*, 66-69.
- (12) Gudixsen, M. S.; Lauhon, L. J.; Wang, J. F.; Smith, D.; Lieber, C. M. *Nature* **2002**, *415*, 617-620.



(13) Peng, X. G.; Manna, L.; Yang, W. D.; Wickham, J.; Scher, E.; Kadavanich, A.; Alivisatos, A. P. *Nature* **2000**, *404*, 59-61.

(14) Hu, J. T.; Li, L. S.; Yang, W. D.; Manna, L.; Wang, L. W.; Alivisatos, A. P. *Science* **2001**, *292*, 2060-2063.

(15) Talapin, D. V.; Koeppel, R.; Gotzinger, S.; Kornowski, A.; Lupton, J. M.; Rogach, A. L.; Benson, O.; Feldmann, J.; Weller, H. *Nano Lett.* **2003**, *3*, 1677-1681.

(16) Hikmet, R. A. M.; Chin, P. T. K.; Talapin, D. V.; Weller, H. *Adv. Mater.* **2005**, *17*, 1436-1439.

(17) Acharya, S.; Patla, I.; Kost, J.; Efrima, S.; Golan, V. *J. Am. Chem. Soc.* **2006**, *128*, 9294-9295.

(18) Mullin, J. W. *Crystallization*, 4th Ed., Butterworth Heinemann, Boston, **2001**.

(19) Manna, L.; Scher, E. C.; Alivisatos, A. P. *J. Am. Chem. Soc.* **2000**, *122*, 12700-12706.

(20) Peng, Z. A.; Peng, X. G. *J. Am. Chem. Soc.* **2001**, *123*, 1389-1395.

(21) Peng, Z. A.; Peng, X. G. *J. Am. Chem. Soc.* **2001**, *123*, 183-184.

(22) Peng, Z. A.; Peng, X. G. *J. Am. Chem. Soc.* **2002**, *124*, 3343-3353.

(23) Peng, X. G. *Adv. Mater.* **2003**, *15*, 459-463.

(24) Soloviev, V. N.; Eichhofer, A.; Fenske, D.; Banin, U. *J. Am. Chem. Soc.* **2000**, *122*,

2673-2674.

(25) Vossmeier, T.; Reck, G.; Schulz, B.; Haupt, E. T. K.; Weller, H. *Science* **1995**, *267*, 1477-1479.

(26) Herron, N.; Calabrese, J. C.; Farneth, W. E.; Wang, Y. *Science* **1993**, *259*, 1426-1428.

(27) Dance, I. G.; Choy, A.; Scudder, L. *J. Am. Chem. Soc.* **1984**, *106*, 6285-6295.

(28) Jun, Y. W.; Lee, S. M.; Kang, N. J.; Cheon, J. W. *J. Am. Chem. Soc.* **2001**, *123*, 5150-5151.

(29) Tang, Z.; Kotov, N. A.; Giersig, M. *Science* **2002**, *297*, 237-240.

(30) Wang, Y.; Tang, Z.; Liang, X.; Liz-Marzan, L. M.; Kotov, N. A. *Nano Lett.* **2004**, *4*, 225-231.

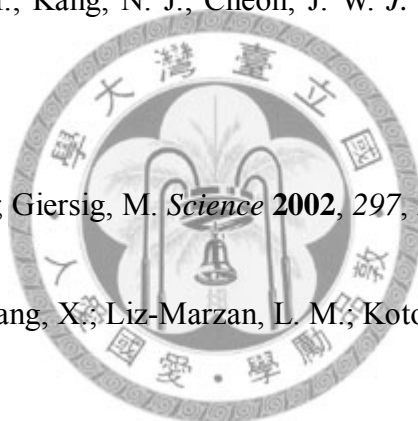
(31) Liang, X.; Tang, S.; Tang, Z.; Kotov, N. A. *Langmuir* **2004**, *20*, 1016-1020.

(32) Wang, Y.; Tang, Z.; Tang, S.; Kotov, N. A. *Nano Lett.* **2005**, *5*, 243-248.

(33) Shim, M.; Guyot-Sionnest, P. *J. Chem. Phys.* **1999**, *111*, 6955-6964.

(34) Goel, S. C.; Chiang, M. Y.; Buhro, W. E. *J. Am. Chem. Soc.* **1990**, *112*, 5636-5637.

(35) Matchett, M. A.; Viano, A. M.; Adolphi, N. L.; Stoddard, R. D.; Buhro, W. E.; Conradi, M. S.; Gibbons, P. C. *Chem. Mater.* **1992**, *4*, 508-511.



- (36) Buhro, W. E. *Polyhedron* **1994**, *13*, 1131–1148.
- (37) Trentler, T. J.; Hichman, K. M.; Goel, S. C.; Viano, A. M.; Gibbons, P. C.; Buhro, W. E. *Science* **1995**, *270*, 1791–1794.
- (38) Wagner, R. S.; Ellis, W. C. *Appl. Phys. Lett.* **1964**, *4*, 89–90.
- (39) Wang, F.; Dong, A.; Sun, J.; Tang, R.; Yu, H.; Buhro, W. E. *Inorg. Chem.* **2006**, *45*, 7511–7521.
- (40) Dong, A.; Wang, F.; Daulton, T. L.; Buhro, W. E. *Nano Lett.* **2007**, *7*, 1308–1313.
- (41) Dong, A.; Tang, R.; Buhro, W. E. *J. Am. Chem. Soc.* **2007**, *129*, 12254–12262.

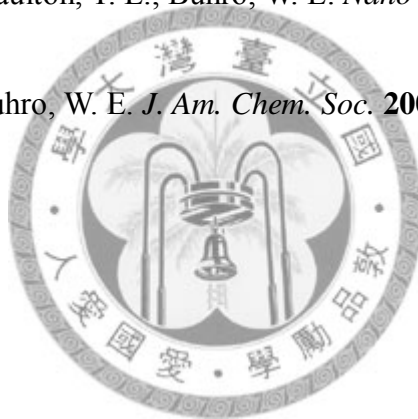


Figure 1

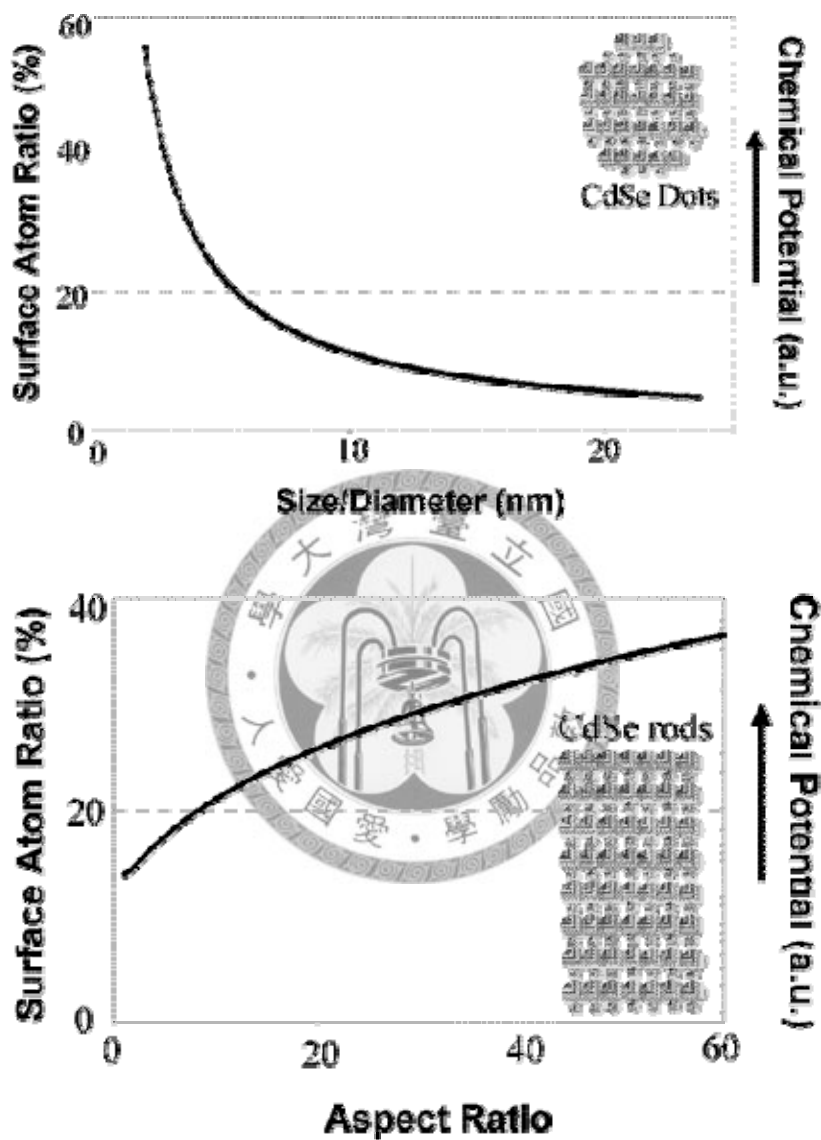


Figure 1. Top: Size-dependence of the surface atom ratio and the relative chemical potential of CdSe nanocrystals, assuming a spherical shape. Bottom: Shape-dependent chemical potential of CdSe quantum rods. The volume of all nanocrystals is set to the same value as of an 8 nm CdSe dot.²²

Figure 2

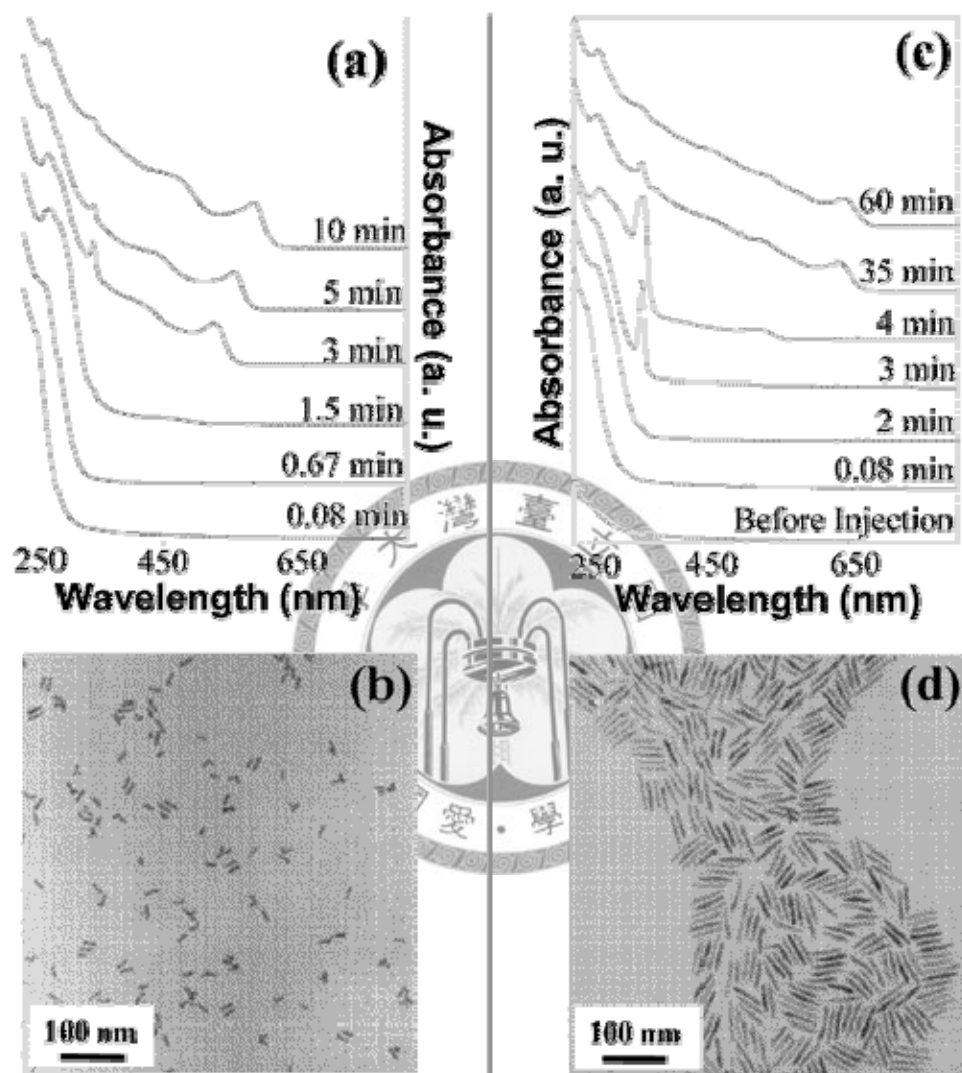


Figure 2. Influence of the history of Cd-TDPA complexes. Left panel: Without aging at room temperature. Right panel: Aged at room temperatures. TEM pictures were taken with the aliquots with the highest average aspect ratio in each reaction.²²

Figure 3

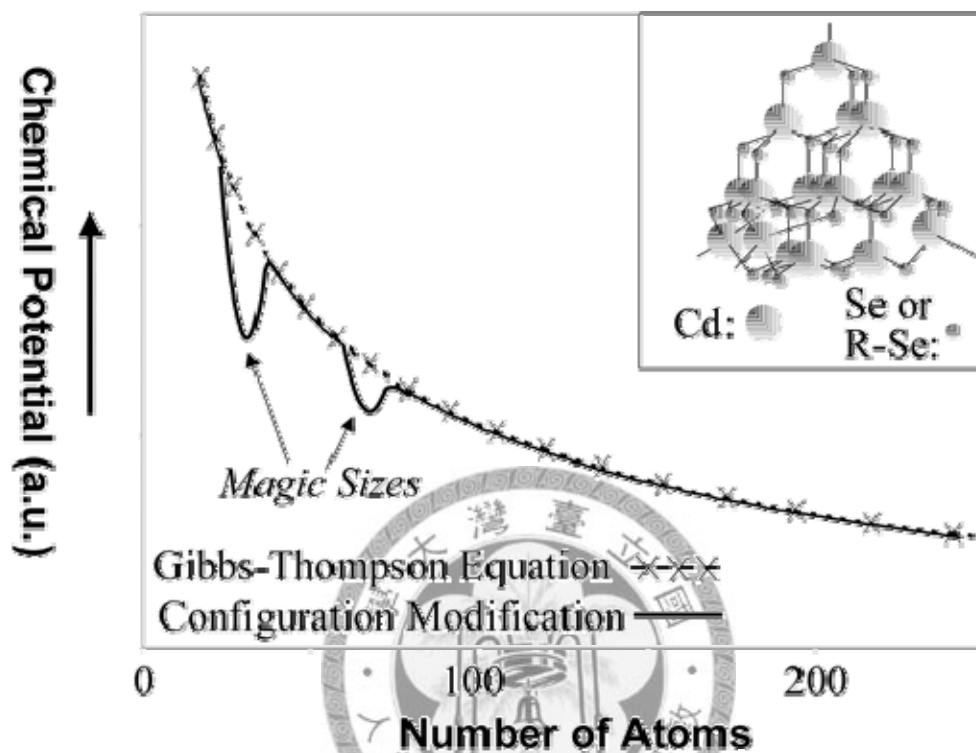


Figure 3. Schematic illustration of the size- and configuration-dependence of the relative chemical potential of crystals/clusters in the extremely small size regime. Inset: Structure of Cd₁₇.²⁵ The magic sized nanocluster observed may likely possess a similar structure.²²

Figure 4

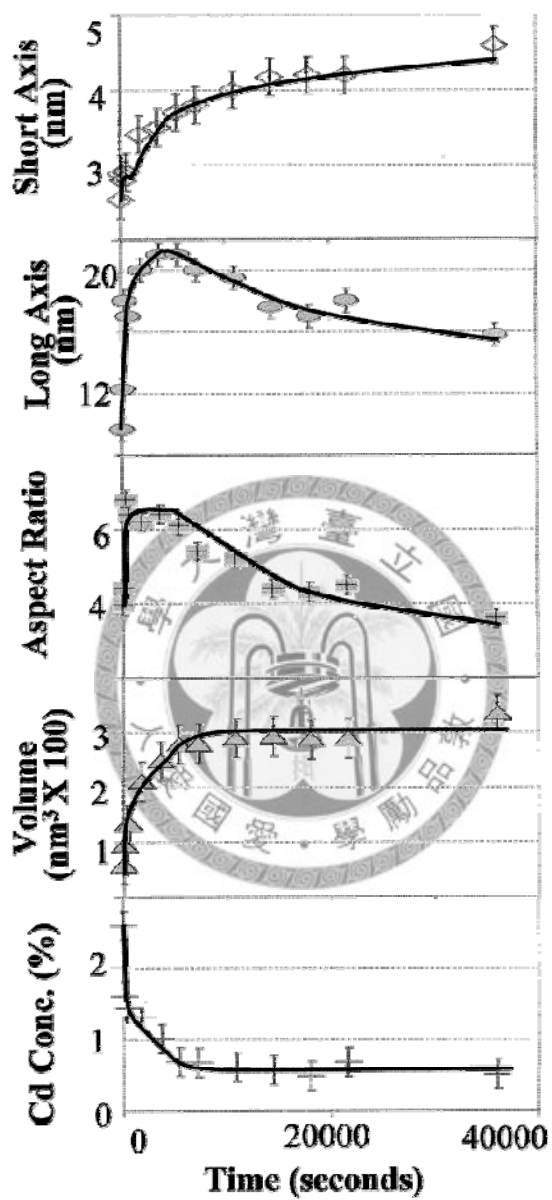


Figure 4. The temporal shape evolution of CdSe nanocrystals determined by TEM and the corresponding temporal variation of Cd monomer concentration in solution determined by ICP.²⁰

Figure 5

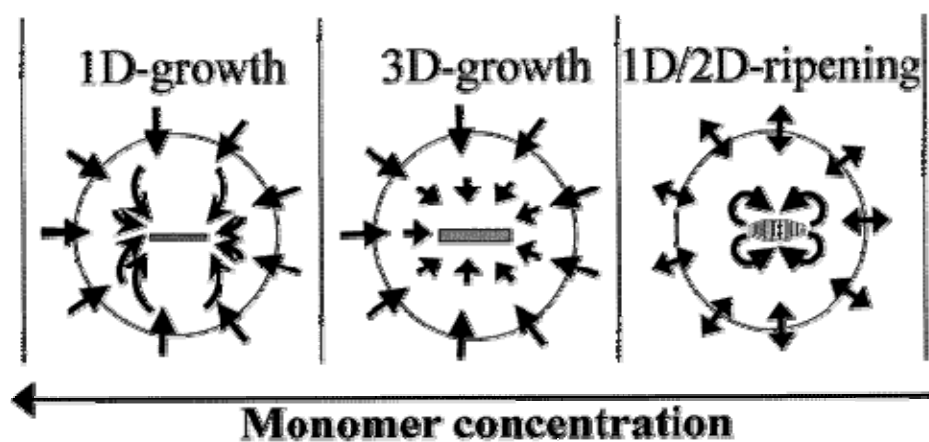


Figure 5. The three growth stages of elongated CdSe nanocrystals at different monomer concentration windows.²⁰

Figure 6

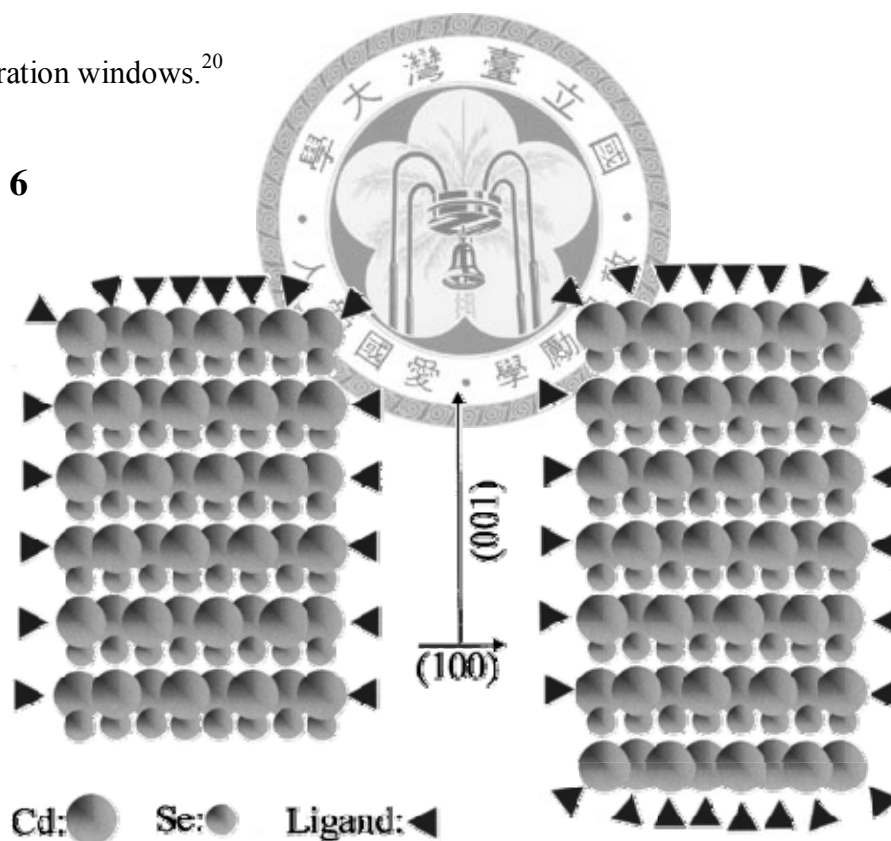


Figure 6. The unique chemical reactivity of the (001) facet of the wurtzite CdSe nanocrystals.²⁰

Figure 7

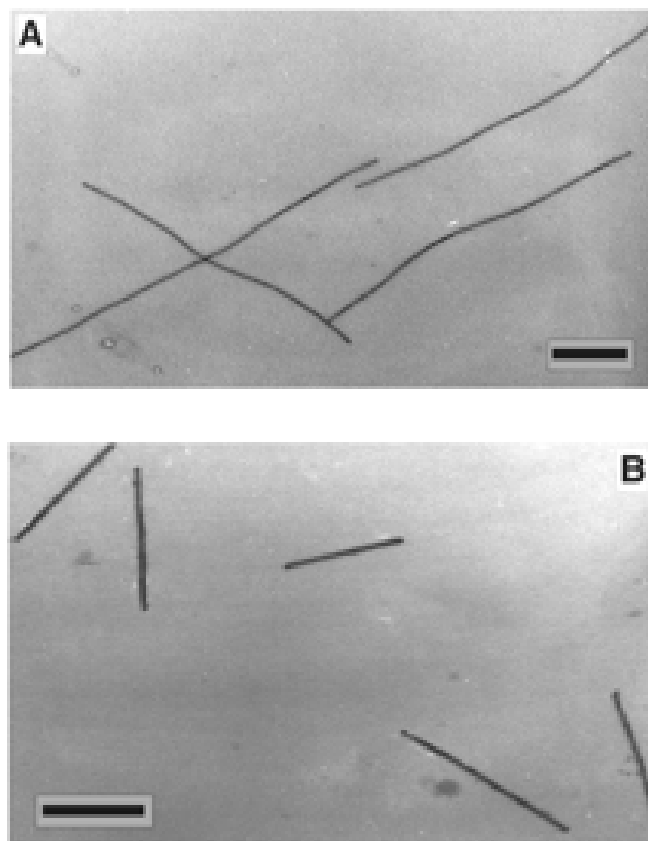


Figure 7. TEM images of CdTe nanowires made from 3.4 (A) and 5.4 nm (B) nanoparticles. Bars, 100 nm.²⁹

Figure 8

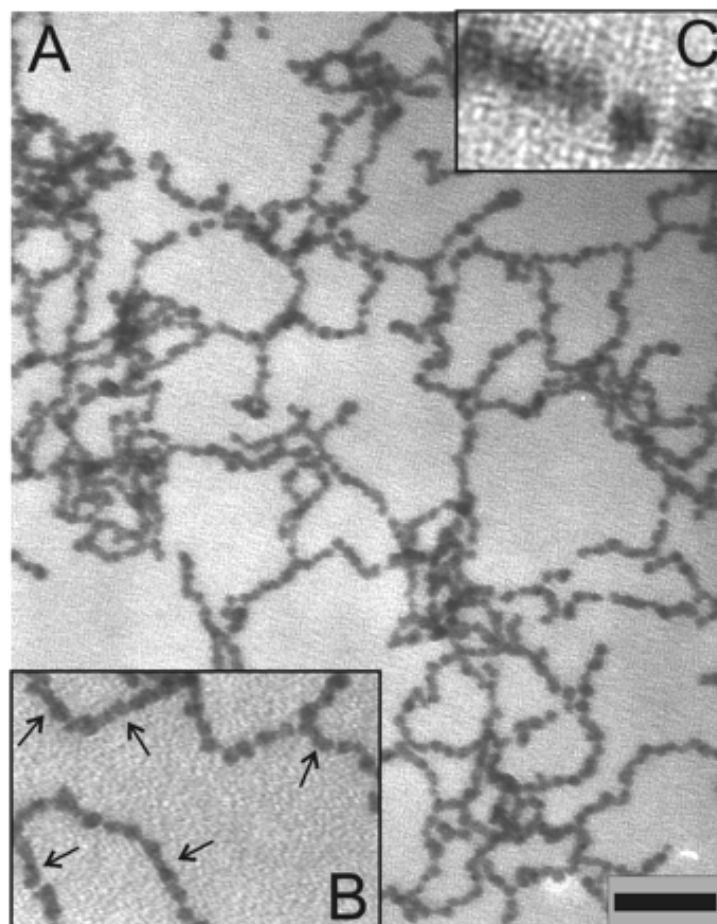


Figure 8. (A) TEM image of intermediate state of nanoparticle-nanowire transition for 5.4-nm nanoparticles. (B) The enlarged portion of the chain, with short rods marked by arrows. (C) The high-resolution TEM image of the adjacent nanoparticles in the chain. The "pearl necklace" aggregates were not observed in the standard dispersions of CdTe.²⁹

Figure 9

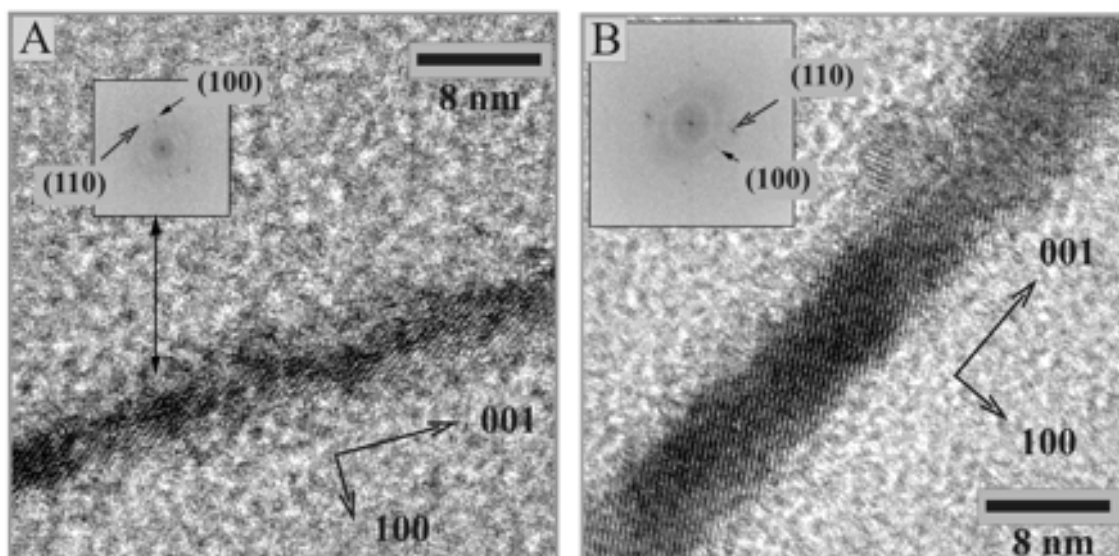


Figure 9. High-resolution TEM of nanowires made from (A) orange- and (B) red-emitting CdTe quantum dots. The insets show the corresponding diffraction patterns for (001) and (100); vectors of the crystal lattice are indicated by thick arrows. Energy dispersive x-ray spectroscopy showed identical chemical composition in respect to Cd and Te for both nanoparticles and nanowires.²⁹

Figure 10

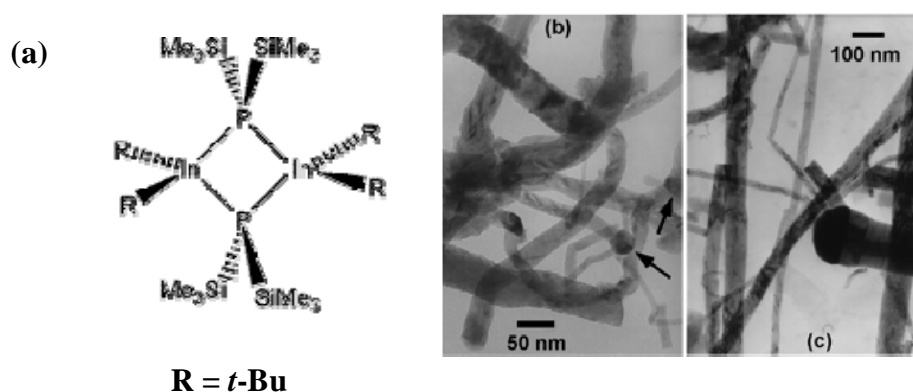


Figure 10. (a) Structure of $\{t\text{-Bu}_2\text{In}[\text{P}(\text{SiMe}_3)_2]\}_2$; (b) under conditions allowing the imaging of the In-catalyst droplets (arrows); (c) from a higher-temperature synthesis employing added In catalyst.³⁶

Figure 11

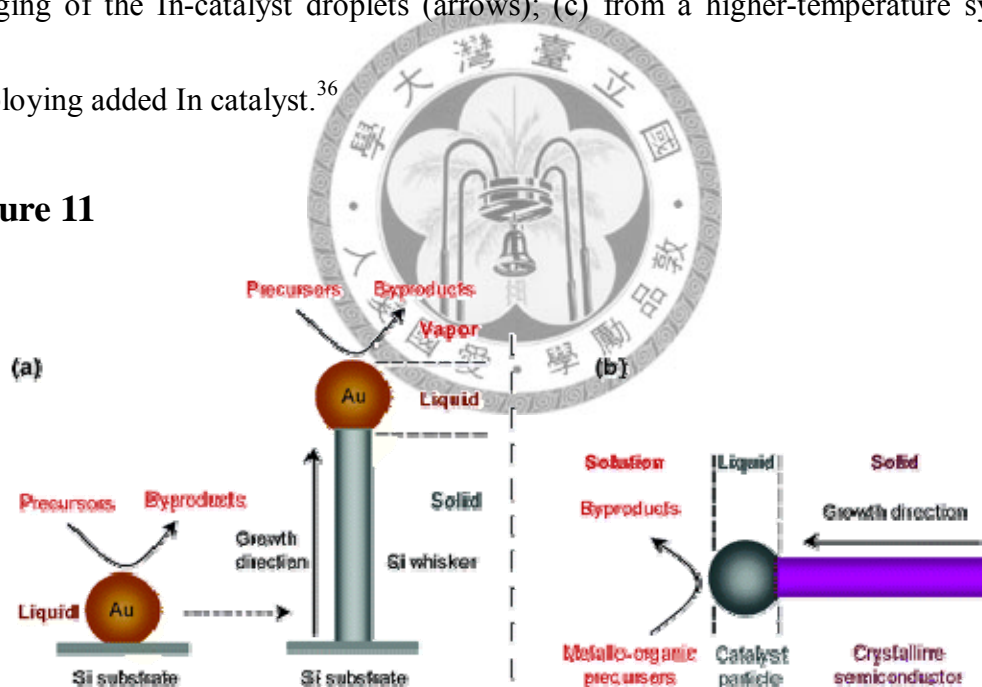


Figure 11. Growth mechanisms for pseudo-1D crystalline morphologies: (a) VLS mechanism proposed by Wagner and Ellis for growth under CVD conditions; (b) SLS mechanism proposed by Buhro and co-workers for analogous growth from solution.³⁹

Figure 12

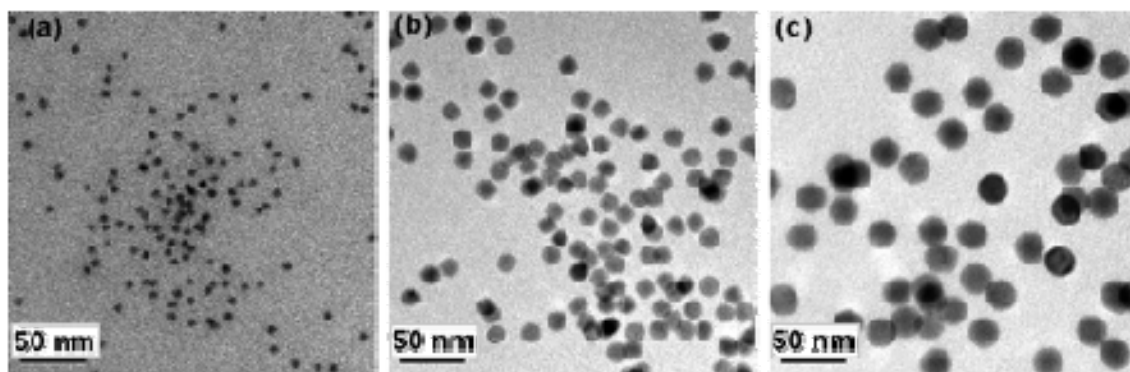


Figure 12. TEM images of near-monodisperse Bi nanoparticles obtained by thermal decomposition of $\text{Bi}[\text{N}(\text{SiMe}_3)_2]_3$ with $\text{Na}[\text{N}(\text{SiMe}_3)_2]$. The quantity following the \pm symbol is the standard deviation in the diameter distribution, expressed as a percentage of the mean diameter. Mean diameter = (a) $6.4 \text{ nm} \pm 11.5\%$, (b) $15.1 \text{ nm} \pm 5.6\%$, and (c) $25.2 \text{ nm} \pm 5.1\%$.³⁹

Figure 13

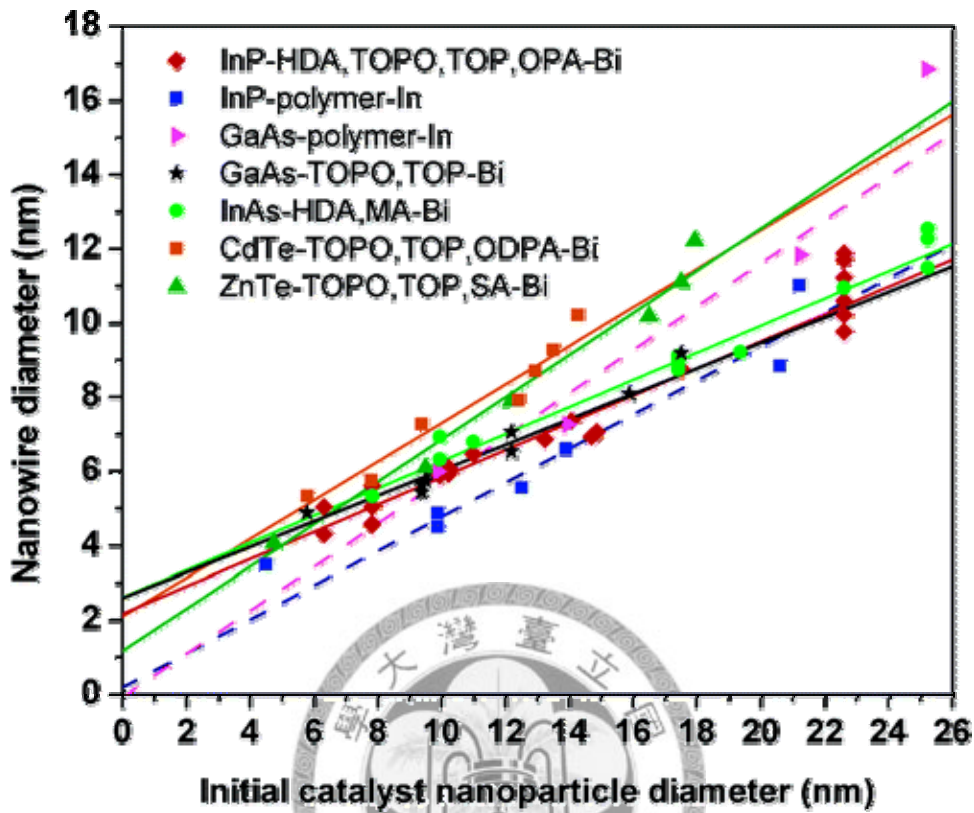


Figure 13. Plots of nanowire diameter vs initial catalyst nanoparticle diameter for SLS-grown wires. The lines are least-squares fits to the data, which are identified in the inset legend. The dotted lines correspond to nanowires grown from In-catalyst nanoparticles. Legend format: nanowire composition-surfactant-catalyst nanoparticle.

HAD = n-hexadecylamine, TOPO = tri-n-octylphosphine oxide, TOP = tri-n-octylphosphine, OPA = n-octylphosphonic acid, MA = myristate, SA = stearate, and polymer = poly(1-hexadecene-co-vinylpyrrolidinone) for InP and poly(1-diphenylphosphinomethyl-4-vinylbenzene)/poly(1-hexadecene-co-vinylpyrrolidinone) mixtures for GaAs.³⁹

Figure 14

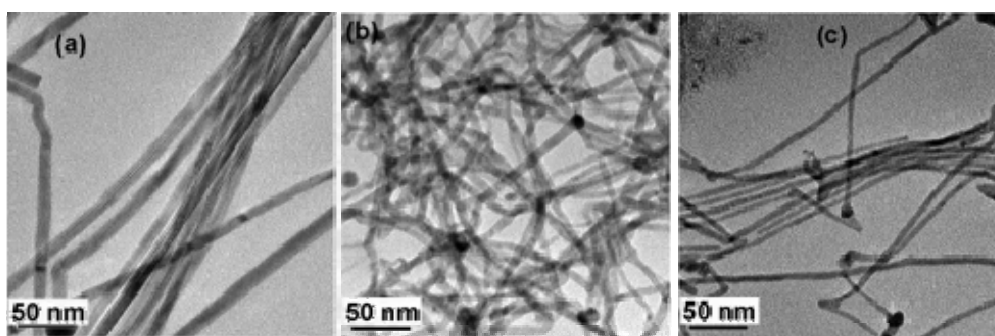


Figure 14. TEM images of SLS-grown III-V nanowires and the corresponding diameters. (a) InP, $11.2 \text{ nm} \pm 17.5\%$, (b) GaAs, $7.0 \text{ nm} \pm 12.7\%$, and (c) InAs, $5.3 \text{ nm} \pm 12.4\%$.³⁹



Figure 15

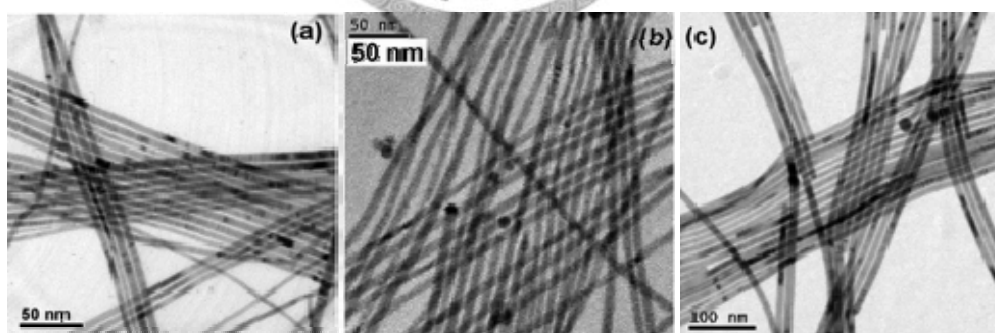


Figure 15. TEM images of SLS-grown II-VI nanowires and the corresponding diameters. (a) CdSe, $5.3 \text{ nm} \pm 14.4\%$, (b) ZnTe, $7.6 \text{ nm} \pm 13.8\%$, and (c) CdTe, $9.7 \text{ nm} \pm 20.6\%$.³⁹

Chapter 2.

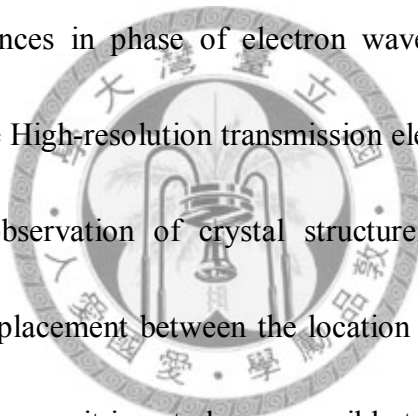
Characterization Techniques

1. Transmission Electron Microscopy (TEM)¹⁻³

Transmission electron microscopy is an imaging technique wherein a beam of electrons is transmitted through a specimen. A magnified image is formed, and the signals are directed to a fluorescent screen, a photographic film, or a charged-coupled device (CCD) camera. Electrons have both wave and particle properties. As for wave-like property, wavelength which could be much smaller than that of light is determined by accelerating fields. Electrons are generated by processes known as thermionic discharge or field emission. Emitted electrons are then accelerated by an electric field and focused by electrical and magnetic fields onto the sample. Areas where electrons are scattered appear dark on the screen, forming a positive image. Comparing with traditional microscope, TEM provides very high resolution and improved depth of vision. The capabilities of the TEM can be further extended by acquiring additional detectors on the same microscope. An analytical TEM is equipped with detectors that can determine the elemental composition of the specimen by analyzing X-ray spectrum or energy-loss spectrum of the transmitted electrons. Modern TEM may include aberration correctors, to reduce the amount of distortion in the image, allowing

information on features on the scale of 0.1 nm to be obtained (resolutions down to 0.05 nm have been achieved) at magnifications of 50 million times. Monochromators may also be used to reduce the energy spread of the incident electron beam to less than 0.15 eV. Figure 1 shows an illustration of a typical TEM system. Major TEM makers include JEOL, Hitachi High-technologies, FEI Company and Carl Zeiss.

Crystal structure can be investigated by High Resolution Transmission Electron Microscopy (HRTEM), also known as phase contrast imaging technique, as the images are formed due to differences in phase of electron waves scattered through a thin specimen. Furthermore, the High-resolution transmission electron microscopy (HRTEM) technique allows direct observation of crystal structure, an advantage over other methods because of no displacement between the location of a defect and the contrast variation in the image. However, it is not always possible to interpret the lattice images directly in terms of sample structure or composition. Because the image is sensitive to a number of factors (specimen thickness and orientation, objective lens defocus, spherical and chromatic aberration), it is inherently complicated, and may require extensive simulation of the images. Computer modeling of these images has added a new layer of understanding to the study of crystalline materials. The resolution of the HRTEM is limited by spherical and chromatic aberration and a set of aberration correctors would be able to overcome spherical aberration. Software correction of spherical aberration



has allowed the production of images with sufficient resolution to show carbon atoms in diamond separated by only 0.089 nm and atoms in silicon at 0.078 nm at magnifications of 50 million times. Improved resolution has also allows monitoring the lighter atoms that scatter electrons less efficiently. The ability of determining positions of atoms within materials has made the HRTEM an indispensable tool for nanotechnology research and development in many fields, including heterogeneous catalysis and semiconductor devices for electronics and photonics. However, there are a number of drawbacks to the TEM technique. Many materials require extensive sample preparation to produce a sample thin enough to be electron transparent, which makes TEM analysis a relatively time consuming process with a low throughput of samples. The structure of the sample may also be changed during the preparation process. The field of view is relatively small, raising the possibility that the region analyzed may not be characteristic of the whole sample. There is potential that the sample may be damaged by the electron beam, particularly in the case of biological materials.

To measure the spectrum of electron energy losses, an EELS spectrometer can be mounted after the projector lenses of the TEM. The heart of most EELS spectrometers is a magnetic sector, which provides the energy dispersion of the electrons. In the homogeneous magnetic field of the sector, Lorentz forces will bend electrons of equal energies into arcs of equal curvature. Some such electron trajectories are shown in

Figure 2. From the figure we can see that electrons are selected by a variable entrance aperture. Electrons travel down a “drift tube” through the spectrometer and are deflected through $\geq 90^\circ$ by the surrounding magnetic field. Electrons with greater energy loss (dashed line) are deflected further than those suffering zero loss (full line). A spectrum is thus formed in the dispersion plane which consists of a distribution of electron counts versus energy loss. This process is exactly analogous to the dispersion of white light by a glass prism.

2. Ultraviolet-visible spectroscopy (UV/Vis)⁴

Experimentally, the efficiency of light absorption at a wavelength λ by an absorbing medium is defined by the Beer-Lambert law, which is most often used in a quantitative way to determine concentrations of an absorbing species in solution.

$$A = -\log(I / I_0) = \varepsilon \cdot c \cdot L$$

where A is the measured absorbance, I_0 is the intensity of the incident light at a given wavelength, I is the transmitted intensity, L is the path length through the sample, and c is the concentration of the absorbing species. For each species and wavelength, ε is a constant known as the molar absorptivity or extinction coefficient. This constant is a fundamental molecular property in a given solvent, at a particular temperature and pressure. The Beer-Lambert Law is useful for characterizing many compounds but does

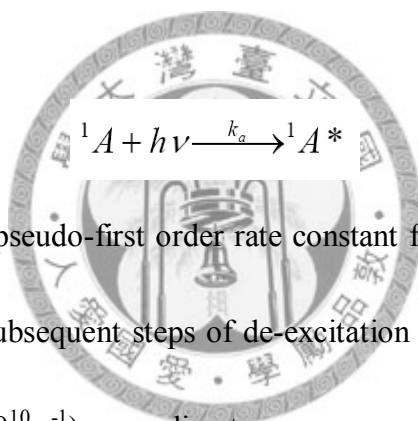
not hold as a universal relationship for the concentration and absorption of all substances. UV/vis spectrophotometer measures the intensity of light passing through a sample (I), and compares it to the intensity of light before it passes through the sample (I_0). The I / I_0 ratio is called the transmittance, and is usually expressed as a percentage ($\%T$). The absorbance, A , is based on the transmittance

$$A = -\log(\%T)$$

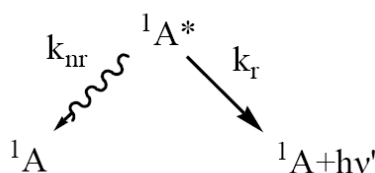
The basic set of a spectrophotometer contains a light source, a holder for the sample, a diffraction grating or monochromator to separate the different wavelengths of light, and a detector. The detector is typically a photodiode or a CCD. Photodiodes are used with monochromator, which filter the light so that only light of a single wavelength reaches the detector. Diffraction gratings are used with CCD, which collects light of different wavelengths on different pixels. An ultraviolet-visible spectrum is essentially a graph of light absorbance versus wavelength in a range of ultraviolet or visible regions. Such a spectrum can often be produced directly by a more sophisticated spectrophotometer, or the data can be collected for one wavelength at a time by simpler instruments. Wavelength is often represented by the symbol λ . For a given substance, a standard graph of the extinction coefficient (ϵ) vs. wavelength (λ) may be made or used if one is already available. Such a standard graph would be effectively "concentration-corrected" and thus is independent of concentration.

3. Steady-State Fluorescence

Emission and excitation spectra are recorded by an Edinburgh (FS920) spectrofluorometer. The light source is Xe lamp emitting a constant photon flow, i.e. a constant amount of photons per unit time, whatever their energy. Let us denote by N_0 the constant amount of incident photons entering, during a given time, a unit volume of the sample where the fluorophore concentration is $[A]$ (N_0 and $[A]$ in unit of mol L^{-1}). αN_0 represents the amount of absorbed photons per unit volume involved in the excitation process.



Let us recall that the pseudo-first order rate constant for this process is very large ($k_a \sim 10^{15} \text{ s}^{-1}$) whereas the subsequent steps of de-excitation occur with much lower rate constants (k_r and $k_{nr} \sim 10^7 - 10^{10} \text{ s}^{-1}$), according to



Under continuous illumination, the concentration $[{}^1A^*]$ remains constant, which means that ${}^1A^*$ is in a steady state. Measurements under these conditions are then called *steady-state measurements*.

The rate of change of $[{}^1A^*]$ is equal to zero:

$$\frac{d[{}^1A^*]}{dt} = 0 = k_a \alpha N_0 - (k_r + k_{nr})[{}^1A^*]$$

$k_a \alpha N_0$ represents the amount of absorbed photons per unit volume per unit time. It can be rewritten as αI_0 where I_0 represents the intensity of the incident light (in moles of photons per liter per second).

The constant concentration $[{}^1A^*]$ is given by

$$[{}^1A^*] = \frac{\alpha I_0}{k_r + k_{nr}}$$

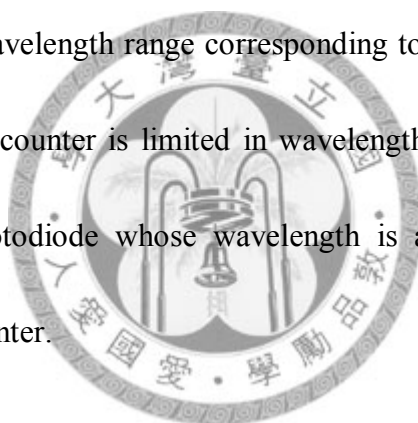
The amount of fluorescence photons emitted per unit time and per unit volume, i.e. the *steady-state fluorescence intensity*, is then given by

$$i_F = k_r [{}^1A^*] = \alpha I_0 \frac{k_r}{k_r + k_{nr}} = \alpha I_0 \Phi_F$$

This expression shows that the steady-state fluorescence intensity per absorbed photon $i_F / \alpha I_0$ is the fluorescence quantum yield Φ_F .

Figure 3 shows the components of a conventional spectrofluorometer. The light source is generally a high-pressure xenon arc lamp, which offers the advantages of continuous emission from 190 nm to the 2600 nm with intense lines between 800 and 1000 nm. A monochromator is used to select the excitation wavelength. Fluorescence is collected at right angles with respect to the incident beam and detected through a monochromator by a photomultiplier. Automatic scanning of wavelength is achieved by the electronic devices and the computer where the data are stored.

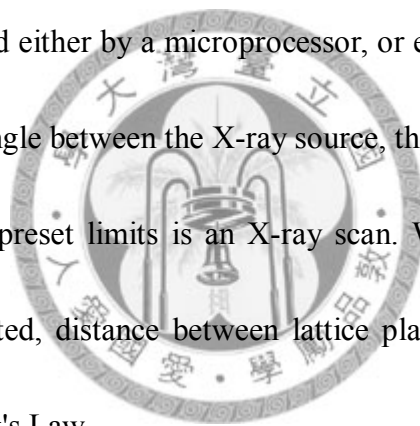
The optical module contains various parts: a sample holder, shutter, polarizers if necessary, and a beam splitter consisting of a quartz plate reflecting a few percent of the exciting light towards a quantum counter or a photodiode. A quantum counter usually consists of a triangular cuvette containing a concentrated solution of a dye whose fluorescence quantum yield is independent of the excitation wavelength. At such high concentration, the solution absorbs all incident photons and the light collected at right angles by a reference photomultiplier is proportional to the photon flux of the incident light over the excitation wavelength range corresponding to the absorption range of the dye. However, a quantum counter is limited in wavelength to the absorption range of the dye. Therefore, a photodiode whose wavelength is as flat as possible may be preferred to a quantum counter.



4. X-Ray Diffraction (XRD)⁵

The three-dimensional structure of nonamorphous materials, such as minerals, is defined by regular, repeating planes, namely a crystal lattice. When a focused X-ray beam interacts with these lattice planes, a portion of the beam is diffracted. Diffraction of X-ray occurs according to the type of atoms and how these atoms are arranged in the crystal. In X-ray powder diffractometry, X-rays are generated within a sealed tube that is under vacuum. A current is applied for heating a filament within the tube. The number

of electrons emitted from filament is proportional to the applied current. Generation of electrons is analogous to the production of electrons in a television picture tube. A high voltage, typically 15-60 kilovolts, is applied within the tube. This high voltage accelerates the electrons, which then hit a target, commonly made of copper. When these electrons hit the target, X-rays are produced. The wavelength of these X-rays is characteristic of that target. These X-rays are collimated and directed onto the sample, typically a powder form in which particle size is less than 10 micrometers. Signals are then detected and processed either by a microprocessor, or electronically, converted to a count rate. Changing the angle between the X-ray source, the sample, and the detector at a controlled rate between preset limits is an X-ray scan. When an X-ray beam hits a sample and thus is diffracted, distance between lattice planes of the sample could be deduced by applying Bragg's Law,



$$n\lambda = 2d \sin \theta$$

where the integer n is the order of the diffracted beam, λ is the wavelength of the incident X-ray beam, d is the distance between adjacent planes of atoms (the d-spacing), and θ is the angle of incidence of the X-ray beam. Since the λ is known and θ is measured, the d-spacing could be calculated. The geometry of an XRD unit is designed to accommodate this measurement (Figure 4). The characteristic set of d-spacings generated in a typical X-ray scan provides a unique fingerprint of the samples. When

properly interpreted, by comparison with standard reference patterns and measurements, this fingerprint allows for identification of the desired material.

5. Confocal Microscopy^{6,7}

Confocal microscopy offers several advantages over conventional optical microscopy, including shallow depth of field, elimination of out-of-focus glare, and the ability to collect serial optical sections from thick specimens. Figure 5 illustrates the principal light pathways in a basic confocal microscope configuration. Coherent light emitted by the laser system (excitation source) passes through a pinhole aperture that is situated in a conjugate plane (confocal) with a scanning point on the specimen and a second pinhole aperture positioned in front of the detector (a photomultiplier tube). As the laser is reflected by a dichromatic mirror and scanned across the specimen in a defined focal plane, secondary fluorescence emitted from points on the specimen (in the same focal plane) pass back through the dichromatic mirror and are focused as a confocal point at the detector pinhole aperture.

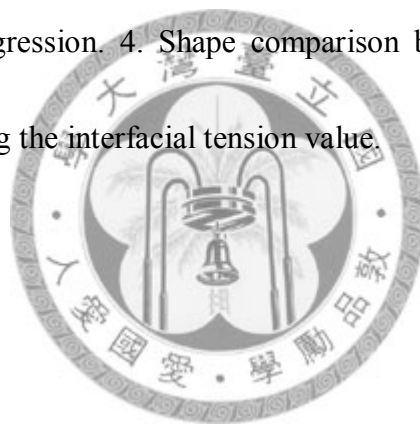
When fluorescent specimens are imaged using a conventional widefield optical microscope, secondary fluorescence emitted by the specimen that appears away from the region of interest often interferes with the resolution of those features that are in focus. This situation is especially problematic for specimens having a thickness greater

than about 2 micrometers. The confocal imaging approach provides a marginal improvement in both axial and lateral resolution, but it is the ability of the instrument to exclude from the image the “out-of focus” flare that occurs in thick fluorescently labeled specimens, which has caused the recent explosion in popularity of the technique. Because the resolution possible in the laser scanning confocal microscope is somewhat better than in the conventional widefield optical microscope, but still considerably less than that of the transmission electron microscope, it has in some ways bridged the gap between the two more commonly used techniques.

6. Pendant Drop Method^{8,9}

The pendant drop method is probably the most convenient, versatile and popular method to measure interfacial tension between molten polymers, which involves the determination of the profile of a drop of one liquid suspended in another liquid at mechanical equilibrium. The profile of a drop is determined by the balance between gravity and surface forces. As shown in Figure 5, a typical pendant drop apparatus consists of three parts: an experimental cell, an illuminating and viewing system to visualize the drop, and a data acquisition system to infer the interfacial tension from the pendant drop profile. Using a pendant drop system it is possible to register the evolution of a drop. Images of the drop are taken automatically at a certain frequency which

depends on the time duration of the test. The images are digitized by a frame grabber resident in the computer and are analyzed immediately during measurement. The contours of the drops are analyzed to infer interfacial tension from the profile of the drop using different programs. The whole process of digitalization and analysis includes four steps: 1. Capture and digitalization of the image of the pendant drop. 2. Extraction of the drop contour and determination of the radius of curvature at the apex necessary for the calculation of interfacial tension. 3. Smoothing of the extracted contour of the drop using polynomial regression. 4. Shape comparison between the theoretical and experimental drop, inferring the interfacial tension value.



7. References

- (1) Wang, Z. L. *Characterization of Nanophase Materials*, Wiley & Sons: New York, **2000**.
- (2) Williams, D. B.; Carter, C. B. *Transmission Electron Microscopy*, Plenum: New York, **1996**.
- (3) Ahn, C. V. *Transmission Electron Energy Loss Spectrometry in Materials Science and the EELS Atlas*, Wiley & Sons: New York, **2004**.
- (4) Cao, G. *Nanostructures & Nanomaterials*, Imperial College: London, **2004**.

(5) Callister, Jr. W. D. *Materials Science and Engineering an Introduction*, Wiley & Sons: New York, **2003**.

(6) <http://www.olympusfluoview.com/>

(7) <http://www.microscopyu.com/>

(8) Arashiro, E. Y.; Demarquette, N. R. *Mater. Res.* **1999**, 2, 23-32.

(9) Cabezas, M. G.; Bateni, A.; Montanero, J. M.; Neumann, A. W. *Langmuir* **2006**, 22, 10053-10060.



Figure 1

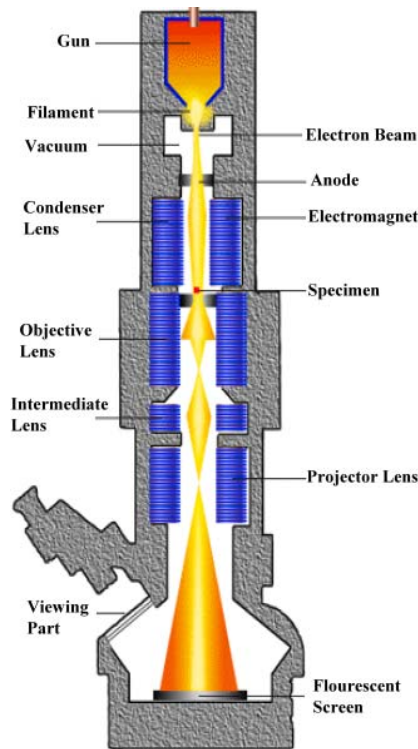


Figure 1. An illustration of a typical TEM system.

Figure 2

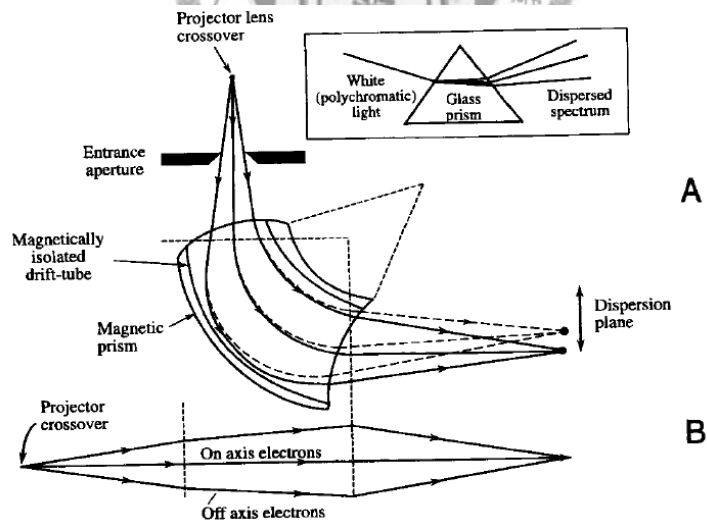


Figure 2. Ray paths through a magnetic prism spectrometer showing (A) dispersion and focusing of the electrons in the plane of the spectrometer and (B) the lens-focusing action in the plane normal to the spectrometer; compare the nonfocusing action of a glass prism on visible light (inset).

Figure 3

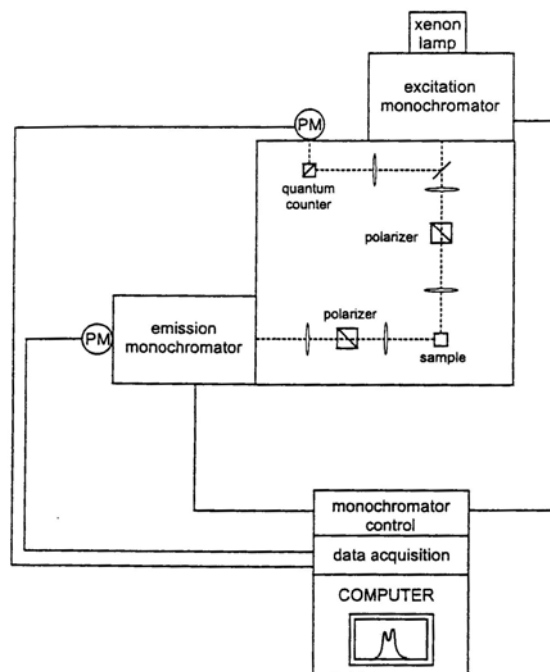


Figure 3. A conventional spectrofluorometer.

Figure 4

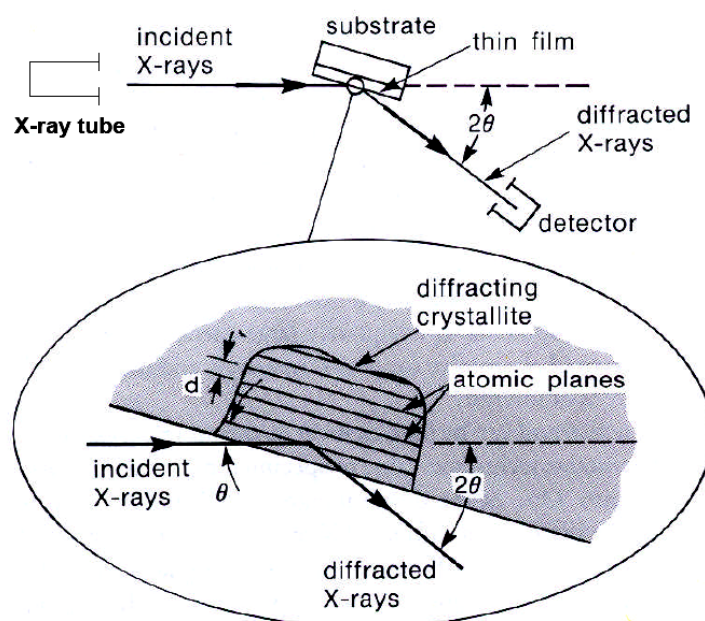


Figure 4. Basic features of typical XRD experiment.

Figure 5

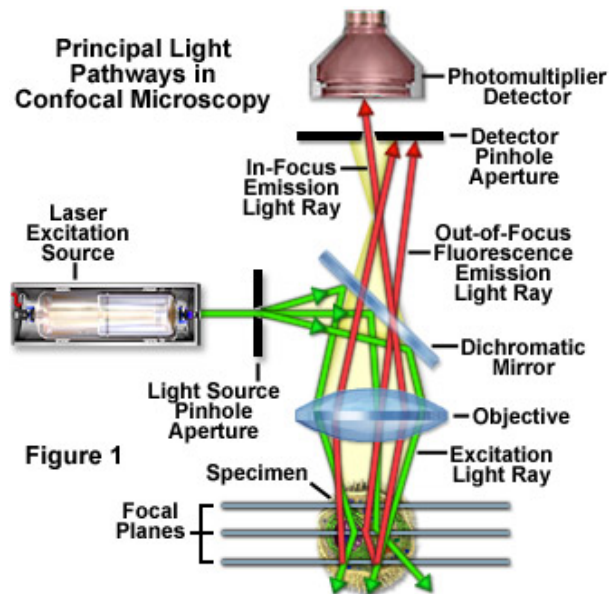


Figure 1

Figure 5. Schematic diagram of the optical pathway and principle components in a basic confocal microscope.



Figure 6

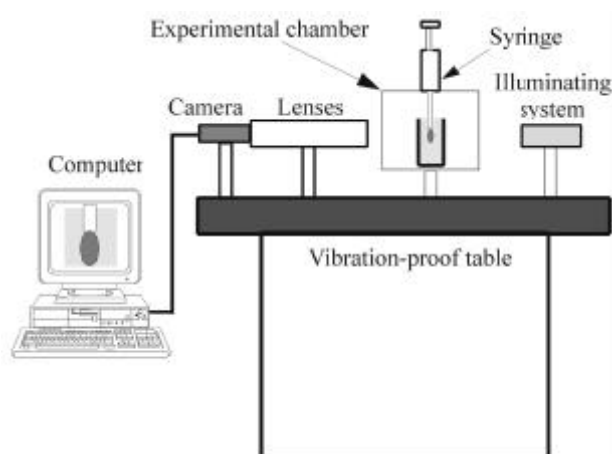
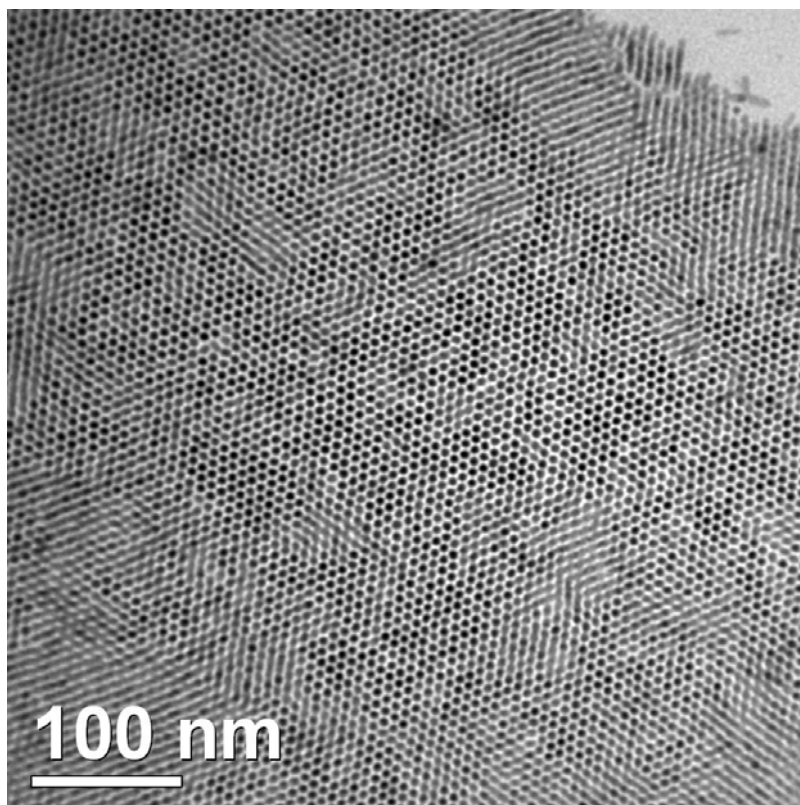


Figure 6. Schematic diagram of the pendant drop apparatus.

Chapter 3.

2D Self-Bundled CdS Nanorods with Micrometer Dimension in the Absence of External Directing Process



Abstract

In the absence of an external direction-controlling process, exclusive self-bundled arrays of CdS nanorods are formed using a facile solution-based method involving trioctylphosphine (TOP) and tetradecylphosphonic acids (TDPA) as co-surfactants. CdS self-bundled arrays with an area of as large as $2.0 \mu\text{m}^2$ could be obtained. Detailed

mechanistic investigation leads us to conclude that the matching in nanorod concentration, intrinsic properties of CdS, and the hydrocarbon chains of the surfactants between adjacent CdS rods play key roles in the self-assembly. In sharp contrast to the defect dominant emission in solutions, the self-bundled CdS nanorods exhibit optical emission nearly free from the defect-states, demonstrating their potential for applications in luminescence and photovoltaic devices.

1. Introduction

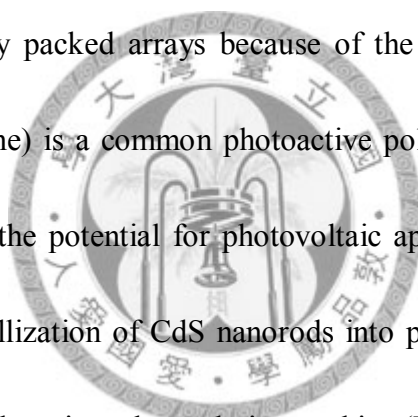


In addition to zero dimensional semiconductor nanoparticles (also referred to as “quantum dots”), one dimensional semiconductor nanocrystals that are several nanometers in diameter and have different aspect ratios have also drawn much attention due to their fascinating size-dependent optical and electronic properties. Pioneering works have unravelled unique linear polarized emission along the *c*-axis of crystals in CdSe and CdSe/CdS (core/shell) nanorods owing to their intrinsic dipolar structure.¹⁻⁵ Concurrently, tremendous efforts have been devoted to the alternative synthesizing routes and the growth mechanism of semiconductor nanocrystals.⁶⁻²² Regarding the updated progress, the Gibbs-Curie-Wulff theorem, which concludes that minimization of total free energy in the reaction system is essential to determine the crystalline shapes,

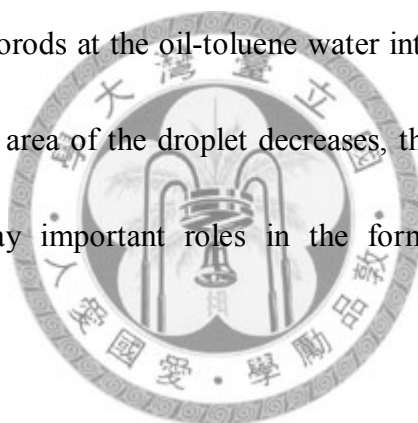
may not be valid in explaining the anisotropic shape-controlling models of nanocrystals.^{1,6-8,13,16} Alternatively, the models of effective-monomer,^{1,7-8,16} selective-adsorption,⁶ and the presence of “magic-sized” nuclei^{7,13} turn out to be more appropriate in rationalizing the kinetic growth mechanism of the semiconducting nanorods.

Elongated semiconducting nanocrystals, such as CdSe or CdTe nanorods, are highly attractive for photovoltaic applications due to their ability to transport charges along the long axis.^{23,24} Nowadays, state-of-the-art synthetic techniques can provide nanorods with uniform size and shape distribution.^{6-8,11-13,19} These nanorods can also offer a route to systematically study the effect of shape on the phase behavior, namely the liquid crystalline phase and self-assembled superstructures. Moreover, macroscopic assembly of nanorods might have advantages for applications in photovoltaic, field emission, and data storage devices. Onsager first claimed that anisotropic particles may form a liquid crystalline phase, which shows long range ordering in orientation but disordering in position.²⁵ Further research supports this notable theory, and large-scale spatial organization has been obtained by depositing concentrated solutions of CdSe and CdSe/CdS heterostructure aggregates onto substrates.²⁶⁻²⁸ Recently, Alivisatos and coworkers reported the assembly of CdS nanorod superlattices by the combination of a DC electric field and controlled solvent evaporation.²⁹ During gentle evaporation of

toluene, the CdS nanorods were confined into an array by the DC electric field, making the long axis of the rods in the same direction. The net effect was a 2D superlattice “standing” on the substrate. Concurrently, Gupta *et al.* discovered similar results with CdSe nanorods.³⁰ The surface of CdSe nanorods was modified by polyethylene oxide (PEO) or polystyrene (PS). Poly(methyl methacrylate) (PMMA) or poly(3-hexylthiophene) (P3HT) were added to the CdSe solution to serve as the polymer matrix. In the presence of an electric field, alkane-covered CdSe nanorods were corralled into densely packed arrays because of the polymer-ligand interaction. Since poly(3-hexylthiophene) is a common photoactive polymer, the polymer-nanorod assembly appears to have the potential for photovoltaic applications. In 2007, Ryan’s group reported supercrystallization of CdS nanorods into perpendicular superlattices.³¹ Via the assistance of highly oriented pyrolytic graphite (HOPG), hexagonal oriented domains of CdS nanorods bundles can be obtained on a variety of substrates without an external electric field. More recently, Manna’s group synthesized CdS nanorods through a seeded-growth approach in which CdSe nanoparticles were used as seeds to produce asymmetric core-shell CdSe/CdS nanorods. By evaporating the solvent at the toluene/water interface or under the applied electric field, large areas of vertically aligned nanorods arrays were obtained.³²



To investigate the internal force that laterally bunches nanorods together, Korgel and the coworkers calculated the dipole-dipole attractive force and van der Waals attraction of self-alignment CdS nanorods.³³ The result of calculations suggested that side-by-side alignment was more favourable than the end-to-end case. Conversely, experimental results from the same report showed networks of end-to-end stripes instead of side-by-side assembly, and it was thus proposed that the formation of stripes was kinetically limited, or mediated, by solvent evaporation. Also, He *et al.* studied the self-assembly of CdSe nanorods at the oil-toluene water interface.³⁴ During the solvent evaporation, as the surface area of the droplet decreases, the in-plane compression and the interfacial tension play important roles in the formation of two dimensional assembled structures.



Although the bundling of 1D semiconductor nanostructures has been theoretically predicted and experimentally observed, exclusively well-aligned arrays of nanorods without an external direction-controlling force, e.g. applying an external electric field or evaporation in the presence of ordered substrate, have not been reported yet. In this work, upon capping CdS with tri-*n*-octylphosphine (TOP) and tetradecylphosphonic acid (TDPA) with the optimum ratio, exclusive formation of arrays of self-bundled CdS nanorods (~5 nm in diameter and ~15 nm in length) without the presence of an external electric field or the direction-controlling substrates was observed. It is found that as the

solvent evaporates and the concentration of the solid increases, the decreasing of the interfacial energy of the nanorods caused by interlacing the alkyl chains of surfactants plays a key factor to account for the driving force. Details of the results and discussion regarding the assembled CdS nanorods are elaborated as follows.

2. Experimental Section

Tetradecylphosphonic acid (TDPA, 98 %) was purchased from Alfa Aesar. Tri-*n*-octylphosphine (TOP, > 85 %) and *n*-hexadecylamine (HDA, 90 %) were purchased from TCI. Cadmium oxide (CdO, 99.99%) and sulfur (S, 99.5%) powder were obtained from Strem Chemicals and ACROS, respectively. Chemicals were used as received.

CdS nanorod was synthesized according to the literature methods⁸ with modification by varying surfactants. Briefly, a sulfur injection solution containing 0.072 g of sulfur (2.25 mmol) was prepared by dissolving sulfur powder in 2 mL of tri-*n*-octylphosphine. 0.1 g of CdO (0.78 mmol) and 0.4565 g of TDPA (1.64 mmol) were loaded into a 50 mL three-neck flask and heated to 200 °C under Ar flow. After

the CdO was completely dissolved, judging by the disappearance of the brown color of CdO, the Cd-TDPA complex was allowed to cool to room temperature.

As for the addition of TOP (or HDA), the weight percentage has been optimized such that the formation of the CdS self-bundle array was maximized. In detail, 5 mL of TOP or 1.35 g of HDA was added to the flask, and the temperature was raised to 330 °C to produce an optically clear solution. At this temperature, the sulfur injection solution was swiftly injected into the hot solution. The reaction mixture was maintained at 330°C for growth of CdS crystals. After 5 minutes, the temperature was quenched to 40°C to terminate the reaction. 5 mL of toluene was then introduced to dissolve the reaction mixture, and yellow precipitate was obtained by adding 5 mL of isopropanol and centrifuged at 3,000 rpm for 5 minutes. The precipitate was washed with toluene and isopropanol three times and re-dispersed in toluene for the TEM characterization. The dried powder of the precipitate was obtained for the XRD measurement. The shapes and size distributions of the nanocrystals were measured with a JEOL JEM 1230 transmission electron microscope (TEM). The surface energies of suspensions with different CdS concentrations were determined using the pendant drop method,³⁵ and the data was analyzed with DataPhysics SCA20 software. The crystal structure and phases of the synthesized samples were analyzed by X-ray powder diffraction (XRD) on a PANalytical X'Pert PRO with Cu K α X-ray. Emission spectra were recorded with an

Edinburgh (FS920) fluorometer. In order to investigate the possible differences in photoluminescence between nanorods in solution and those in self-assembled bundles, the latter were measured with a confocal microscope (WITec AlphaSNOM) coupled with a red-sensitive charge coupled detector (CCD, Princeton Instruments, PI-MAX). Note that in the confocal microscopy, the probing laser (406 nm, 0.3 μm in diameter) was located on the region of self-assembled bundles determined by TEM. Ti:sapphire laser (Tsunami, Spectra-Physics) with an 80MHz repetition rate was used as the excitation source for the lifetime measurement. This laser beam (820 nm) was directed into a doubling crystal (BBO) to yield an UV beam (406 nm) as a pulsed excitation source for the solution study. As for the self-bundled CdS nanorods, the 406 nm beam was then guided to a telescope for focusing. The confocal microscope was applied to monitor the self-bundled CdS nanorods in an area of 0.5 μm in diameter. The fluorescence signal was analyzed by the time-correlated single photon counting system (SPC-300, Becker & Hickl) and high speed photodetector module (OT900, Edinburgh).

3. Results and Discussions

Figures 1a and 1b show TEM images of TDPA and TOP capped, self-assembled CdS nanorods in different scales. Evidently, as depicted in Figures 1a and 1b, exclusive

honeycomb structures were formed. Note that the results are independent of the TEM probing area, as supported by the observation of whole self-bundled CdS nanorods in a largely extended area of micrometer dimensions depicted in Figure 1c. Because the crystal structure of CdS is wurtzite and the growing direction is along the *c*-axis, nanorods with a hexagonal cross-section are anticipated. The single-crystal-like selective-area diffraction pattern (inset in Figure 1a, note that the effective aperture size is ~100 nm and multiple nanorods in the same domain contribute to the pattern) indicates that in addition to the alignment along the *c*-axis, the basalplane (*a*- and *b*-axis) is also self-aligned. The slightly diffused diffraction spots suggest that the basalplane of the rods are rotated within 10 degrees, similar to the results reported by Ryan's group.³¹ Note Figure 1b shows nearly perfect 2D assembly, in which only one vacancy in the lower right part (marked by a red circle) is seen from the uniform hexagonal packing of the CdS nanorods perpendicular to the substrate. The intriguing issue therefore lies in the reason for the predominant corralling of the nanorods. According to previous reports about the self-assembled CdS superstructure,^{29-31,34} evaporation of the solvent causes the corralling-together of the nanorods. However, without direction-controlling external interference,³⁴ the nanorods should form three phases of packing, namely smectic, columnar, and crystal, due to the reduction of interfacial energy. Capillary attraction might help the formation of an ordered structure but could not force the nanorods to

rearrange normal to the interface. Note that the outer edge of the bundled structure in Figure 1a shows a slight tilt of the nanorods, being depicted as a columnar structure,³⁴ (also see Figure 2; the Fourier filtered micrograph with enhanced contrast is presented to view the leaning behavior of edges) the result of which implies that in our experiments, evaporation-induced corralling of the nanorods might be the origin of the self-assembled CdS superstructure. On the other hand, direction-controlling processes such as external DC electric field,²⁹ polymer matrix,³⁰ and highly oriented pyrolytic carbon³¹ all have the purpose of orientating the nanorods perpendicular to the substrate during gentle evaporation of solvent. However, these external direction-controlling methods are not used in this study to control the assembly behavior. As a result, besides the evaporation-induced aggregation of the nanorods, we may narrow down the discussion to the following aspects.

We first consider the concentration effect of the nanorods in the solvent. The sample shown in Figure 1 was prepared with a (toluene) solution that contains 2.5 % CdS in weight. With increasing the weight percentage from 2.5 % to 5 %, the same 2D assembly with an area as large as micrometer dimension was obtained (see Figure 3). However, as shown in Figures 4a and 4b, with a decrease of the concentration of the CdS nanorods from 2.5 to 0.5 weight percent, the 2D framework gradually collapsed. At concentration of ~0.5 weight percent, as shown in Figure 4b, a lying-down monolayer

of CdS nanorods with their *c*-axis parallel to the plane of the grid was clearly observed. Therefore, it is reasonable to predict that the critical concentration of the CdS nanorods in toluene for obtaining the assembled structure might be between 0.5 % and 2.5 % in weight.

Nevertheless, despite the lack of a 2D framework of the CdS nanorods, judging from the TEM image shown in Figure 4b, most of the nanorods are still aligned side by side. The results imply the possible existence of the influence of the surfactants between nanorods, and surfactants that surround the CdS nanorods might play an important role in the self-bundled superstructure. Initially, the reaction system contains Cd-TDPA complex, sulfur and TOP, among which the surfactants that affect shape and aspect ratios are ascribed to TDPA and TOP. Therefore, interaction between the alkyl groups of surfactants might serve as the direction-controlling agent. The tendency of self-association of the hydrocarbon part on the surfactant is known to be the driving force for the micelle formation. Wishnia³⁶ has measured the solubility of hydrocarbons such as ethane, propane, butane, and pentane in sodium dodecyl sulfate (SDS) solution and concluded that the hydrocarbon contribution to the standard free energy is in the range of $-12.0 RT$ to $-18.2 RT$. To a certain degree, the intercrossed hydrocarbon groups of TOP and TDPA that occupy the space between two neighboring CdS nanorods would reduce the free energy and help the self-assembly of CdS nanorods as well. To further

manifest this viewpoint, we thus measured the surface energy of solutions containing different concentrations of CdS nanorods. As shown in Figure 5, at the interval of CdS nanorod concentration from 0.4 to 1.5 weight percent, the surface energy of the solution gradually decreases as the surface concentration of the nanorod increases with the total concentration. Above 1.5 wt.-%, the surface energy of the solution is independent of the total concentration, indicating a constant surface concentration of the nanorod. In other words, the nanorod is saturated in the solution, and aggregates will form to minimize the energy. According to the plot depicted in Figure 5, the critical concentration of the CdS nanorods in toluene should be between 1.0 % and 2.0 % in weight, in good agreement with the concentration used for the TEM observation of 2D self-bundled CdS nanorods (vide supra). This variation of surface energy supports the fact that upon increasing the concentration of nanorods in the solution, CdS nanorods saturate and self-assemble into bundles.

Considering a self-assembled monolayer composed of the organic molecules with a head group and a long-chain alkane tail on the surface of semiconductor, Bent³⁷ recently concluded that the net result of competition between intermolecular and interfacial forces tends to alter the behavior of the monolayers. Good alignment of the alkane tails could be achieved in the case if intermolecular forces overcome the molecule-substrate and lattice forces. On the contrary, if the interfacial forces appear to

dominate over the inter-chain forces, the head groups form commensurate bonding with the underlying surface. Hence, extensively ordered coverage of the head groups on the surface causes mismatch between the semiconductor lattice and molecule-molecule spacing among the head groups. This strain could be released by disordering of the alkane tails, such that the ordered packing of the alkane chains may not be available eventually. These viewpoints further support our observations in the concentration-dependent experiments of the surface energy. In other words, after the concentration of CdS nanorods reaches the critical value (0.4 wt.-%), the intermolecular forces among the alkane-chains of surfactants on adjacent CdS nanorods surpass the interfacial forces between the adsorbed head groups and the surface of the nanorods. Consequently, the construction of self-assembled arrays of CdS nanorods comes with a lowering of surface energy.

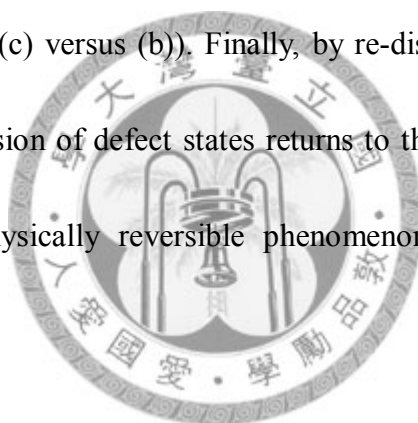
In addition to the solvent-evaporation induced self-assembly, the other key topic would be the direction-controlling effect of the surfactants. We further propose that the three octyl chains from one single TOP molecule might establish a stronger unidirectional superstructure than those surfactants with single hydrocarbon chains. To verify this hypothesis, we thus tentatively used hexadecylamine (HDA) to substitute part of TOP. Figure 6 shows the X-ray powder diffraction (XRD) patterns of the CdS nanorods prepared by using two sets of surfactants: (a) TDPA and TOP (molar ratio of

1:15) and (b) TDPA, HDA and TOP (molar ratio of 1:3.5:6, see experimental section for details). Both patterns show the diffraction peaks matching exactly that of the wurtzite CdS standard pattern (see bottom part of Figure 6). The significantly sharp and narrowed (002) peak at 26.7 degrees (2θ) clearly supports the extended *c*-axis stacking domain of the wurtzite lattice. Note that the broadening of other peaks is due to the corresponding quantized dimensions. Figure 7 shows the TEM image of the CdS nanorods synthesized by using TDPA, HDA, and TOP as surfactants. With control of the concentration of the nanorods (2.0 wt.-%), self-assembly of the nanorods could also be seen on the carbon coated copper grid. However, more than half of the nanorods in the bundle leaned on the substrate, even though the crystalline structure (XRD) is identical for both cases. Further increase of the concentration of HDA capped CdS nanorods did not seem helpful for the assembly. Furthermore, upon an increase of the HDA concentration from 1.35 g (used for obtaining Figure 5) to 4.0 g, the percentage of self-bundled CdS nanorods decreased, accompanied by the elongation of CdS nanorods. As a result, types of surfactants should influence the self-assembly. Since a large amount of the TOP was replaced by HDA, the observation of randomly packed bundles suggests that the three octyl groups on the TOP molecule regulate the bundling direction more readily than the single hexadecyl group on the HDA molecule. Moreover, tetradecyl groups on the TDPA might serve as bridges to enhance the corralling

structure. Certainly, other minor intrinsic properties of the CdS nanorods, such as the dipole-dipole interaction and van der Waals attraction, might also influence the observed self-assembly. As previously concluded by Korgel and coworkers,³³ side-by-side assembly of CdS nanorods was favored in both dipole-dipole interaction (~ 470 meV or ~ 18 kT at room temperature) and van der Waals attraction (~ 140 meV or ~ 5.4 kT) for CdS with an aspect ratio of 9.9.

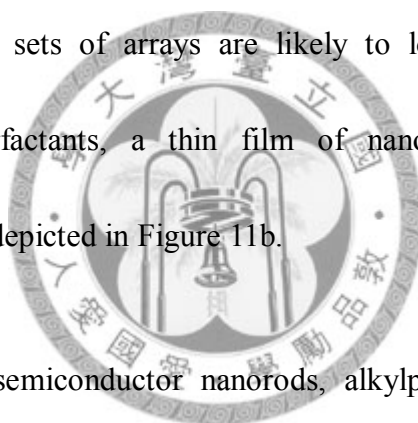
As the emission of quantum confined semiconductors is greatly affected by the dimensions of the nanocrystals, luminescent properties of the bundled nanorods might differ from those of nanorods in solution. Curve (a) of Figure 8 shows emission spectra of CdS nanorods synthesized with TDPA and TOP and dispersed in a toluene solution (0.1 wt.-%). In comparison, curve (b) is that of a single bundled array deposited thin film and measured by a confocal microscope focused on an array area of $0.5 \mu\text{m}$ in diameter using a GaN laser (406 nm). Clearly, the intensity of the broad emission band from 525 nm to 700 nm, which arose from defect states of CdS nanorods in solution, decreased significantly when the nanorods were corralled together. This result was also supported by the corresponding relaxation dynamics, in which the lifetime of the band-edge emission (monitored at 465 nm) of CdS in toluene solution was measured to be 550 ps. On the other hand, probing the area of the CdS self-bundle array with confocal microscope revealed that the lifetime was as long as 4.5 ns, implying the

significant suppression of the radiationless quenching processes. Variation of the emission spectra might be due to the great reduction of the lateral surface area in self-bundled arrays. In the CdS bundles, electrons may hop to the neighboring rods, causing the process of recombination at the defect states to be quenched. Supplementary support of this viewpoint is rendered by tuning the GaN laser to the peripheral region (observed with a microscope) of the self-bundle arrays where the assembly is in a relatively loose structure, resulting in an increase in the intensity ratio for CdS versus defect emission (cf. curve (c) versus (b)). Finally, by re-dispersing the assembled CdS bundles into toluene, emission of defect states returns to the same magnitude as curve (a), demonstrating the physically reversible phenomenon in the self-bundled CdS nanorods.



To gain further insights into the bundling-up phenomenon, Quantifoil holey grids were used for TEM measurements. Figure 9 shows the TEM image of CdS nanorods obtained using the Quantifoil grid. Similar to what was observed using Formvar grids, outside the hole, self-organizing CdS nanorods with honeycomb packing were observed (not shown here). However, inside the hole, a lying-down monolayer of CdS nanorods with their c-axis parallel to the plane of the grid was seen. Judging from the TEM image, most of the nanorods are still aligned side by side, implying the existence of the influence of the surfactants between nanorods even when there is no carbon film

beneath. Combining the results gathered from the Formvar and Quantifoil grids, we tentatively propose that during solvent evaporation, highly solvent swollen surfactants may pull neighboring nanorods together. In addition to the octyl groups on the TOP, as shown in Figure 10, tetradecyl groups on the TDPA might serve as bridges to enhance the corralling structure. With a Formvar grid, the self-assembled arrays of nanorods tend to stand on the carbon film due to the relatively large bottom area as compared with the height of the array, as shown in Figure 11a. Conversely, with a Quantifoil holey grid, as solvent molecules vanish, sets of arrays are likely to loosen, and because of the stretching-out of the surfactants, a thin film of nanorods with a side-by-side arrangement is formed, as depicted in Figure 11b.



In the synthesis of semiconductor nanorods, alkylphosphonic acid is thought mainly to maintain the efficiently high concentration of the cadmium precursor. However, variation of alkyl chains of alkylphosphonic acids may have different effects on the structure-directing templates. Bearing this concept in mind, octadecylphosphonic acid (ODPA) or octylphosphonic acid (OPA) was used to replace TDPA. Figure 12a shows a TEM image of nanorods synthesized by using ODPA, TOPO, and TOP, the same chemicals that were used in Alivisato's report²⁹ but slightly different in experimental protocol. The result is similar to that report, in which both perpendicularly aligned and progressively tilted nanorods were observed in self-assembled CdS arrays.

In addition, the result of nanorods capped by ODPA and TOP is shown in Figure 12b. Judging from the TEM image, dispersed nanorods with side-by-side alignment are obtained, while the self-bundled CdS are obscure. Apparently, by changing the alkylphosphonic acids in the reaction, remarkably different results are observed.

Considering the length of the TDPA molecule is about twice that of TOP, TDPA may act as a bridging agent to stabilize the templates. When TDPA is replaced by ODPA, since the octadecyl groups are longer, the ends of alkyl chains will exceed the bi-layer of self-aligned TOP. Therefore, the templates in the experiment using ODPA, TOPO, and TOP will be strongly disturbed, thus forming nanorods instead of nanowires, as shown in Figure 13a. In other words, in the case of ODPA and TOP, nanorods are separated due to the long hydrocarbon chains of ODPA. Meanwhile, the octadecyl groups that stretch into the octyl layer of TOP on the surface of the nanorods contribute to the release of total free energy. Therefore, the net effect produces side-by-side aligned nanorods, as shown in Figure 13b.

Furthermore, OPA, which has much shorter chains than TDPA and ODPA, but which is comparable to the TOP, is also used in synthesizing nanorods. Figure 14a shows TEM images of bundled long nanorods synthesized by using OPA, TOPO, and TOP, and Figure 14b shows those synthesized by using OPA and TOP. At this stage, all

hydrocarbon chains of the surfactants are octyl group. As a result, self-corralling behavior due to interaction between octyl groups is anticipated. Moreover, templates might be present in the reaction system, but the lack of bridging agents (TDPA) may cause the long range templates to be relatively unstable. Thus, long nanorods instead of nanowires are obtained.

Combining the results by using different alkylphosphonic acids, we therefore tentatively conclude that during the formation of CdS nanocrystals, kinetically balanced templates may be formed by surfactants. The dimensions of the templates can be changed by the hydrocarbon chains of the alkylphosphonic acids. Only with suitable lengths (e.g. TDPA) would the alkyl chains stabilize the templates by bridging the neighboring layers of templates. Surfactants like ODPA, which has longer chains than optimal, would disturb the alignment of surfactants and prevent the formation of long-range stable templates. On the other hand, surfactants like ODA, which has a similar length to TOP, cannot act as a bridge to generate the long-range stability of the template, although these short surfactants will not disturb the template.

4. Conclusion

In summary, exclusive self-assemblies of TDPA and TOP capped CdS nanorods in the absence of external direction-controlling processes (e.g., external electric field, polymer matrix, or highly oriented pyrolytic carbon) are reported. Combining the results and discussion elaborated above, we thus conclude that by using TDPA and TOP as surfactants, the as-prepared CdS nanorods start to corral together with concentration higher than 2.0 % weight percent in toluene. It is believed that the first portion of nanorods, standing normal to the substrate, serves as a nucleation site. Subsequently, the neighboring nanorods tend to assemble in the same direction with the assistance of the hydrocarbon chains on surfactants or the interactions among nanorods. The net result is self-assemblies with outer edges of leaning bundles and an inner part of hexagonal packing perpendicular to the substrate. In comparison to the dominant defect emission of CdS nanorods in toluene solution, the single bundled arrays in a deposited thin film show dramatic decrease of the defect emission, implying the possibilities of enhancing electron transport between nanorods. Also, three other kinds of alkylphosphonic acids are involved in the investigation of the properties of the templates. A growth mechanism based on multiple functions of surfactants is thus proposed to render the rationalization. Accordingly, based on a simple, straightforward bottom-up solution method, it is feasible to construct a monolayer of nanorod bundled polarizer with thickness in the

dimension of nanometers and area in the dimension of micrometers in an aim to greatly facilitate the future preparation of light emitting devices.

5. Acknowledgment

We thank the National Science Council, Taiwan (No. NSC 96-2120-M-002-007) for financially supporting this research.



6. References

- (1) Peng, X. G.; Manna, L.; Yang, W. D.; Wickham, J.; Scher, E.; Kadavanich, A.; Alivisatos, A. P. *Nature* **2000**, *404*, 59-61.
- (2) Hu, J. T.; Li, L. S.; Yang, W. D.; Manna, L.; Wang, L. W.; Alivisatos, A. P. *Science* **2001**, *292*, 2060-2063.
- (3) Talapin, D. V.; Koeppel, R.; Gotzinger, S.; Kornowski, A.; Lupton, J. M.; Rogach, A. L.; Benson, O.; Feldmann, J.; Weller, H. *Nano Lett.* **2003**, *3*, 1677-1681.
- (4) Hikmet, R. A. M.; Chin, P. T. K.; Talapin, D. V.; Weller, H. *Adv. Mater.* **2005**, *17*, 1436-1439.

- (5) Acharya, S.; Patla, I.; Kost, J.; Efrima, S.; Golan, V. *J. Am. Chem. Soc.* **2006**, *128*, 9294-9295.
- (6) Manna, L.; Scher, E. C.; Alivisatos, A. P. *J. Am. Chem. Soc.* **2000**, *122*, 12700-12706.
- (7) Peng, Z. A.; Peng, X. G. *J. Am. Chem. Soc.* **2001**, *123*, 1389-1395.
- (8) Peng, Z. A.; Peng, X. G. *J. Am. Chem. Soc.* **2001**, *123*, 183-184.
- (9) Jun, Y. W.; Lee, S. M.; Kang, N. J.; Cheon, J. W. *J. Am. Chem. Soc.* **2001**, *123*, 5150-5151.
- (10) Li, L. S.; Hu, J. T.; Yang, W. D.; Alivisatos, A. P. *Nano Lett.* **2001**, *1*, 349-351.
- (11) Qu, L. H.; Peng, Z. A.; Peng, X. G. *Nano Lett.* **2001**, *1*, 333-337.
- (12) Qu, L. H.; Peng, X. G. *J. Am. Chem. Soc.* **2002**, *124*, 2049-2055.
- (13) Peng, Z. A.; Peng, X. G. *J. Am. Chem. Soc.* **2002**, *124*, 3343-3353.
- (14) Manna, L.; Scher, E. C.; Li, L. S.; Alivisatos, A. P. *J. Am. Chem. Soc.* **2002**, *124*, 7136-7145.
- (15) Yu, W. W.; Peng, X. G. *Angew. Chem. Int. Ed.* **2002**, *41*, 2368-2371.
- (16) Peng, X. G. *Adv. Mater.* **2003**, *15*, 459-463.
- (17) Mokari, T.; Banin, U. *Chem. Mater.* **2003**, *15*, 3955-3960.

- (18) Yu, W. W.; Wang, Y. A.; Peng, X. G. *Chem. Mater.* **2003**, *15*, 4300-4308.
- (19) Milliron, D. J.; Hughes, S. M.; Cui, Y.; Manna, L.; Li, J.; Wang, L. W.; Alivisatos, A. P. *Nature* **2004**, *430*, 190-195.
- (20) Qu, L. H.; Yu, W. W.; Peng, X. G. *Nano Lett.* **2004**, *4*, 465-469.
- (21) Shieh, F.; Saunders, A. E.; Korgel, B. A. *J. Phys. Chem. B* **2005**, *109*, 8538-8542.
- (22) Kumar, S.; Nann, T. *Small* **2006**, *2*, 316-329.
- (23) Gur, I.; Fromer, N. A.; Geier, M. L.; Alivisatos, A. P. *Science* **2005**, *310*, 462-464.
- (24) Huynh, W. U.; Dittmer, J. J.; Alivisatos, A. P. *Science* **2002**, *295*, 2425-2427.
- (25) Qnsager, L. *Ann. N. Y. Sci.* **1949**, *51*, 627-659.
- (26) Li, L. S.; Walda, J.; Manna, L.; Alivisatos, A. P. *Nano Lett.* **2002**, *2*, 557-560.
- (27) Li, L. S.; Alivisatos, A. P. *Adv. Mater.* **2003**, *15*, 408-411.
- (28) Talapin, D. V.; Shevchenko, E. V.; Mirry, C. B.; Kornowski, A; Forster, S.; Weller, H. *J. Am. Chem. Soc.* **2004**, *126*, 12984-12988.
- (29) Ryan, K. M.; Mastroianni, A.; Stancil, K. A.; Liu, H. T.; Alivisatos, A. P. *Nano Lett.* **2006**, *6*, 1479-1482.
- (30) Gupta, S.; Zhang, Q. L.; Emrick, T.; Russell, T. P. *Nano Lett.* **2006**, *6*, 2066-2069.
- (31) Ahmed, S.; Ryan, K. M. *Nano Lett.* **2007**, *7*, 2480-2485.

(32) Carbone, L.; Nobile, C.; Giorgi, M. D.; Sala, F. D.; Morello, G. Pompa, P. Hytch, M.; Snoeck, E.; Fiore, A.; Franchini, I. R.; Nadasan, M.; Silvestre, A. F.; Chiodo, L.; Kudera, S.; Cingolani, R.; Krahne, R.; Manna, L. *Nano Lett.* **2007**, *7*, 2942-2950.

(33) Ghezelbash, A.; Koo, B.; Korgel, B. A. *Nano Lett.* **2006**, *6*, 1832-1836.

(34) He, J.; Zhang, Q. L.; Gupta, S; Emrick, T.; Russell, T. P.; Thiyagarajan, P. *Small* **2007**, *3*, 1214-1217.

(35) Winkel, D. *J. Phys. Chem.* **1965**, *69*, 348-350.

(36) Wishnia, A. *J. Phys. Chem.* **1963**, *67*, 2079-2082.

(37) Bent, S. F. *ACS Nano* **2007**, *1*, 10-12.



Figure 1

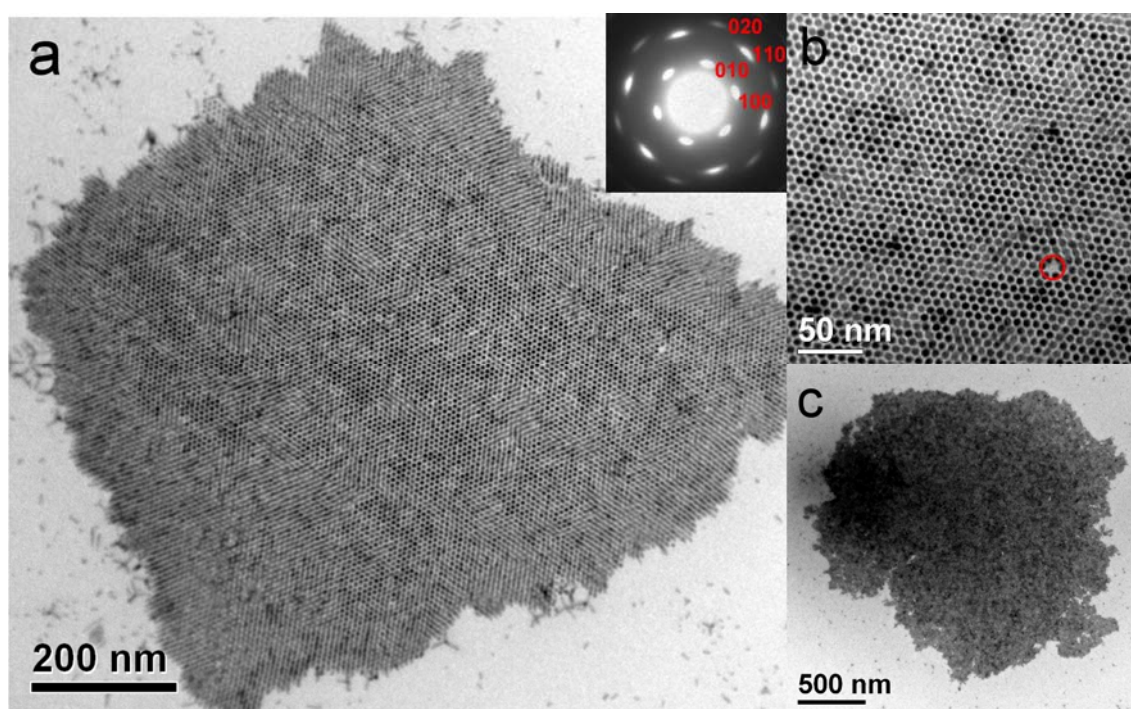


Figure 1. (a) TEM image of TDPA and TOP capped CdS nanorods with self-assembled organization in large scale. The inset shows the diffraction pattern of the bundle. (b) TEM image of bundled-up CdS nanorods in higher magnification. (c) An extended TEM image of self-assembled CdS nanorods.

Figure 2

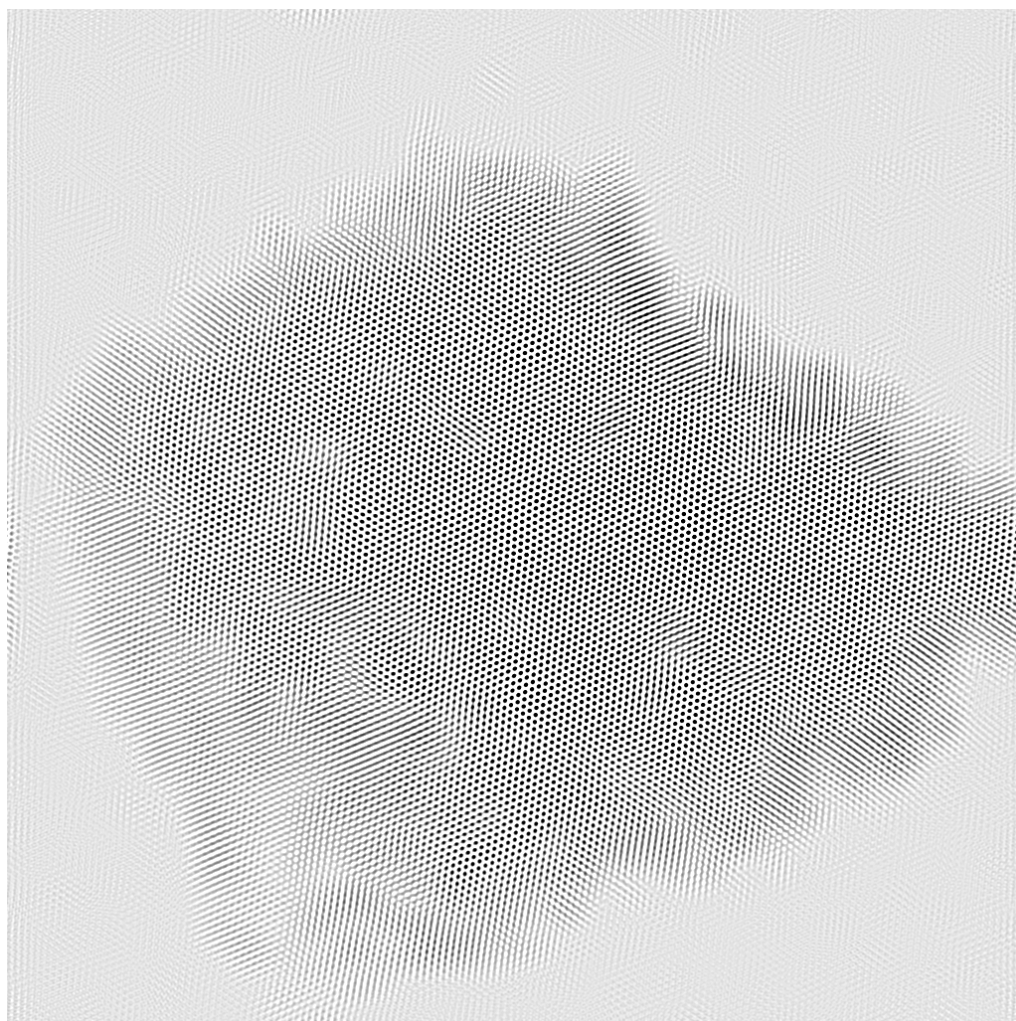


Figure 2. Contrast-enhanced Fourier filtered micrograph of the same region in Figure 1a. The dots are the bundled CdS nanorods standing on the copper grid, and the stripe patterns are the leaning nanorods.

Figure 3

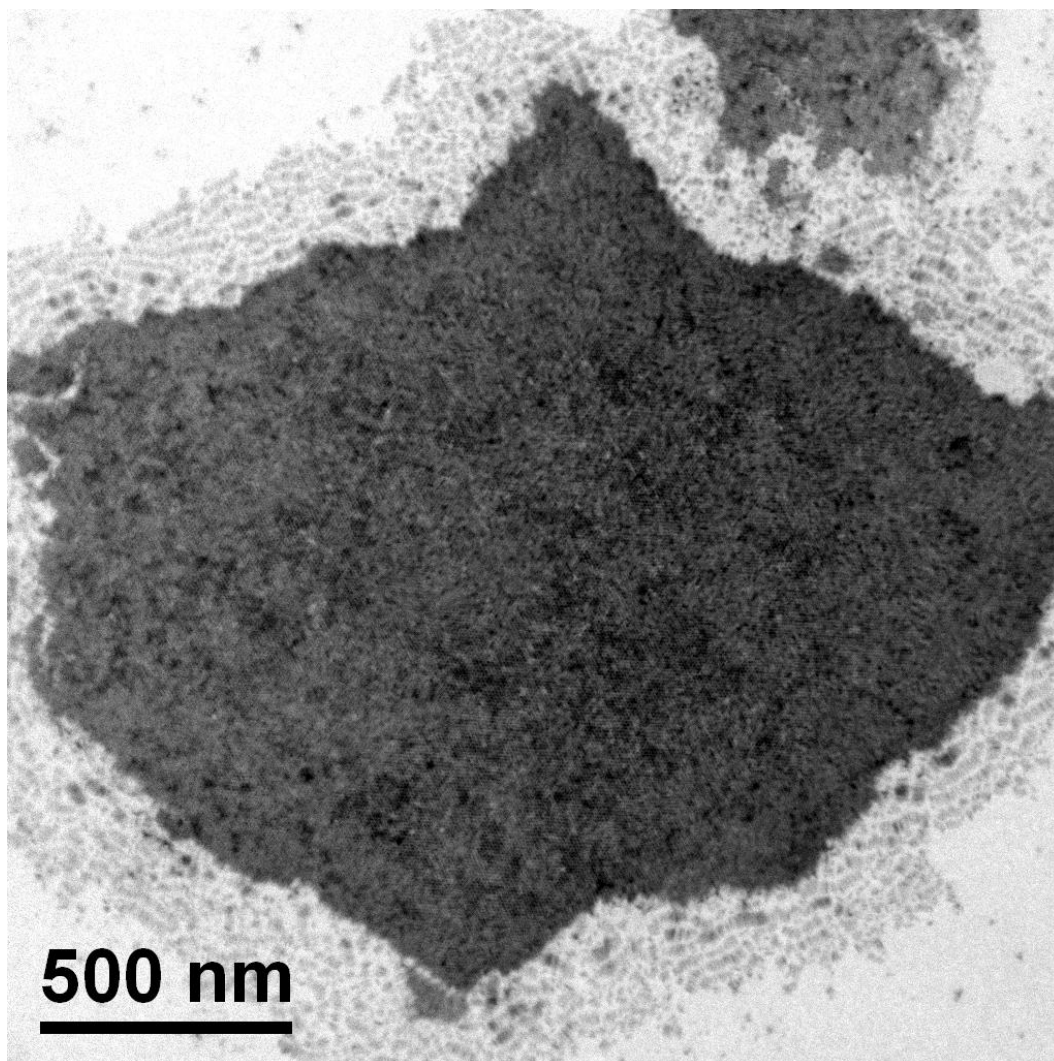


Figure 3. An extended TEM image of self-assembled CdS nanorods synthesized with TDPA and TOP.

Figure 4

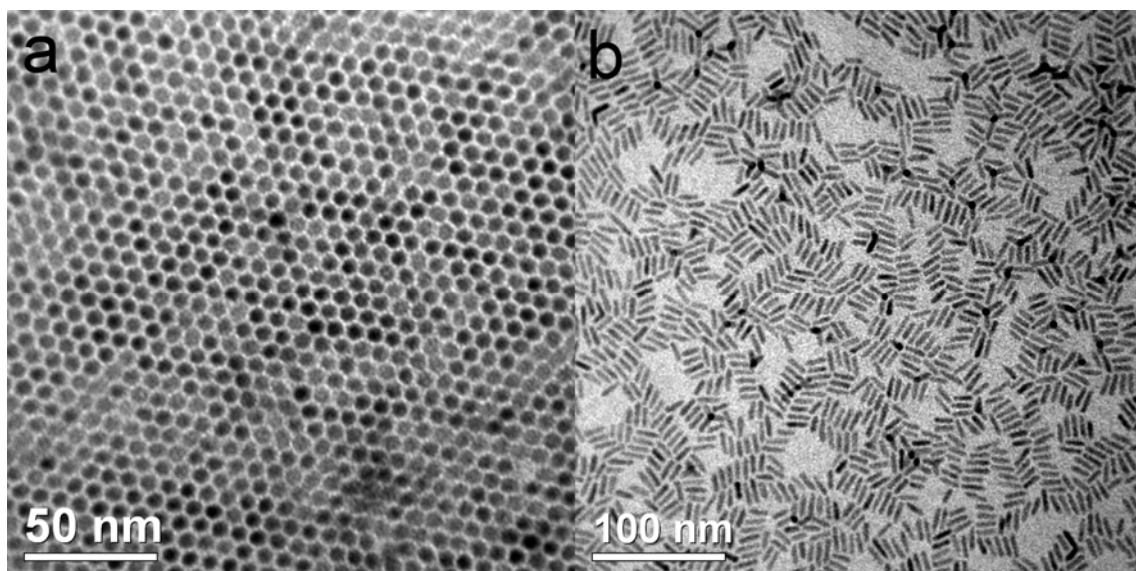


Figure 4. TEM image of TDPA and TOP capped CdS nanorods with concentrations of (a) 2.5 and (b) 0.5 in weight percent.

Figure 5

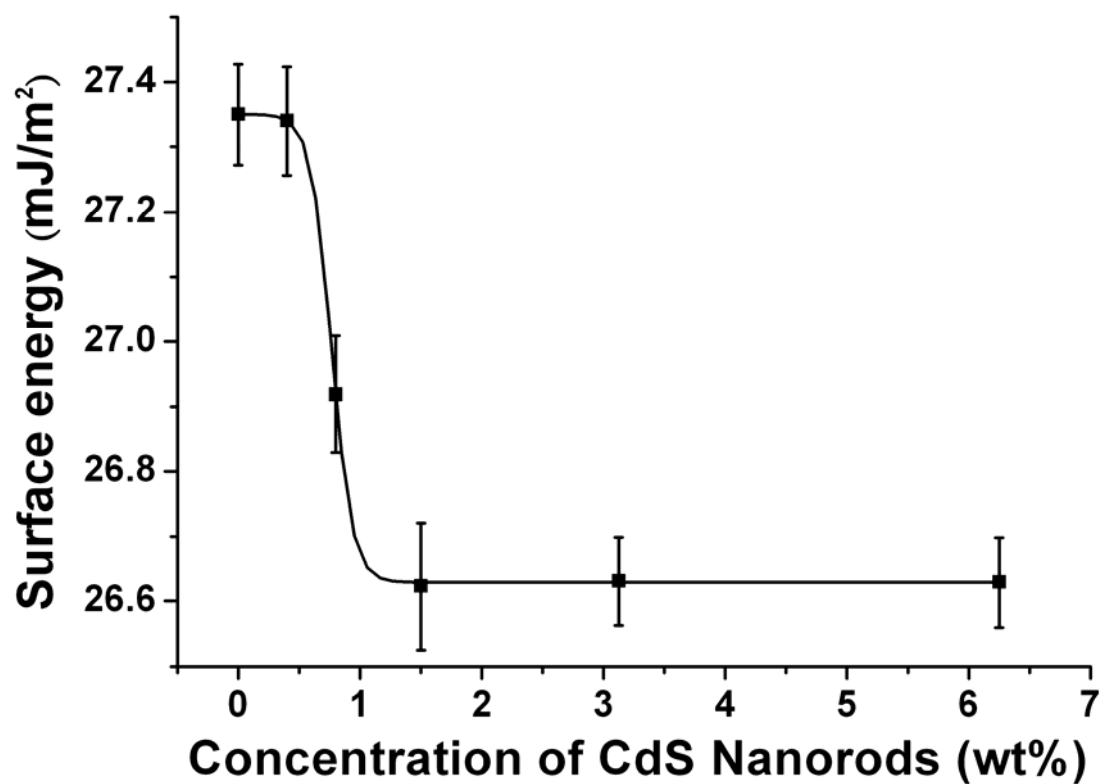


Figure 5. The surface energy, measured by pendent drop method, with respect to different concentrations of CdS nanorods. (0, 0.4, 0.8, 1.5, 3.125, and 6.25 weight percent)

Figure 6

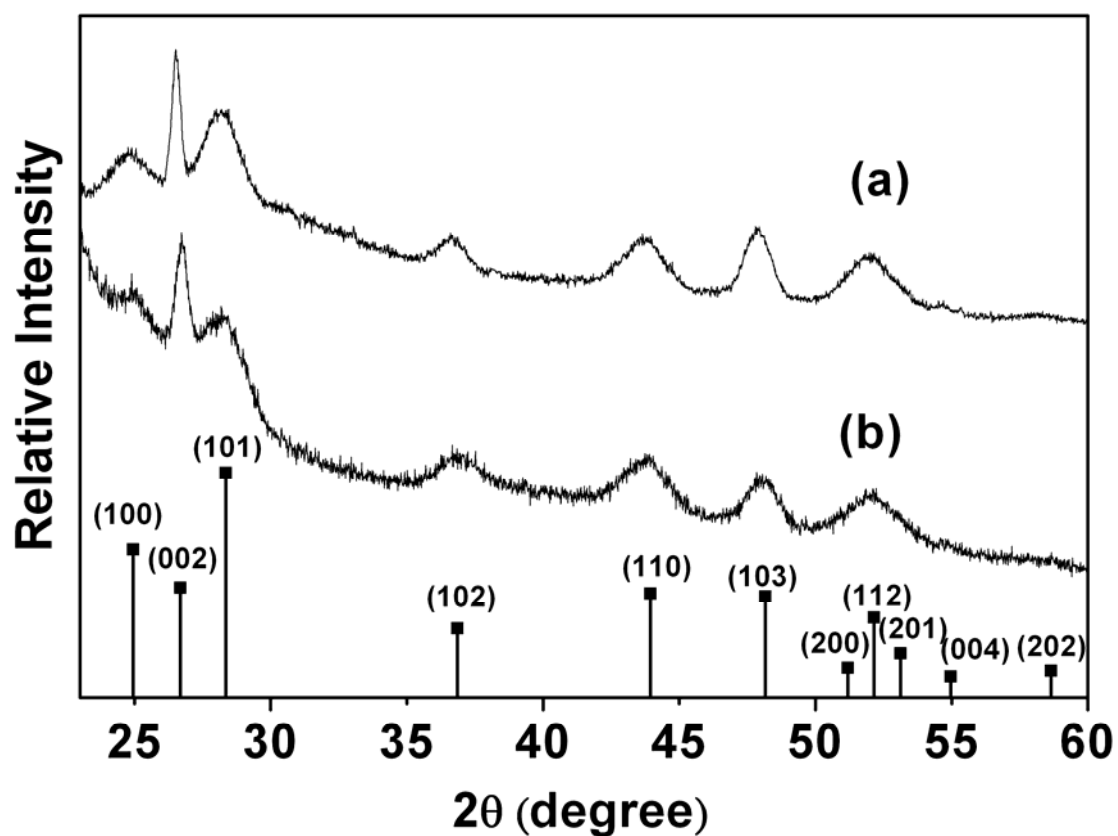


Figure 6. Powder X-ray diffraction (XRD) of CdS nanorods synthesized by using (a) TDPA and TOP, (b) TDPA, HDA, and TOP, and that of standard CdS (wurtzite) pattern (lower).

Figure 7

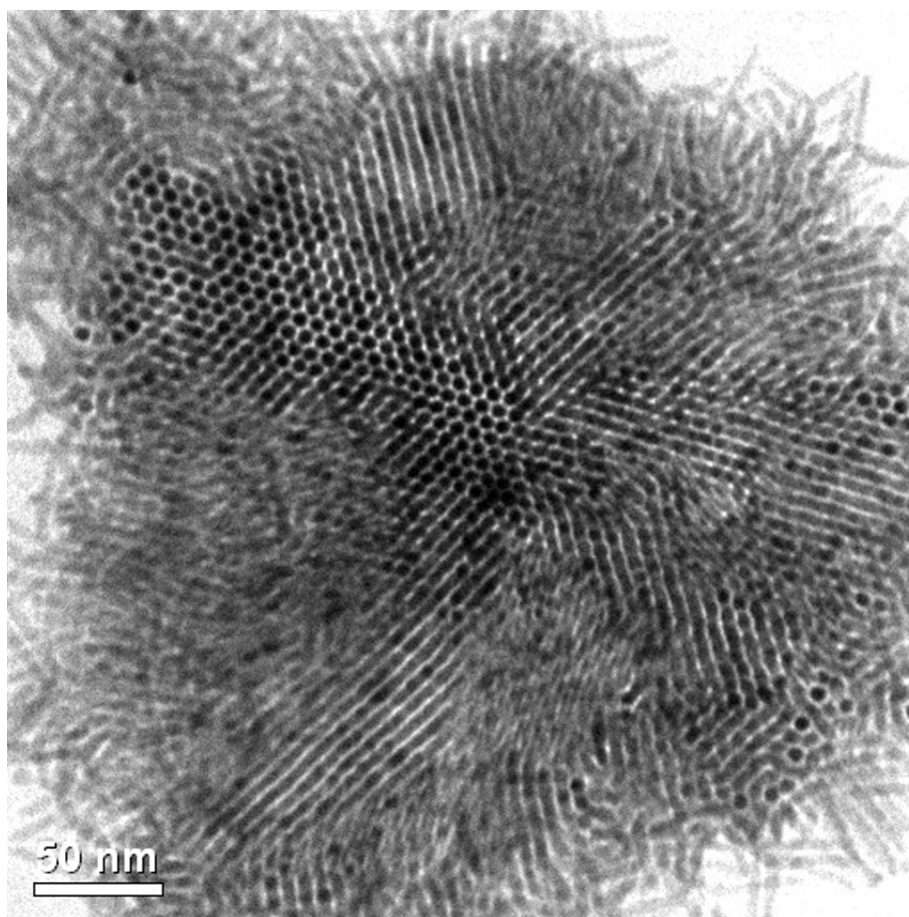


Figure 7. TEM image of TDPA, HDA, and TOP capped CdS nanorods with concentration of 2.0% weight percent (see text for detail).

Figure 8

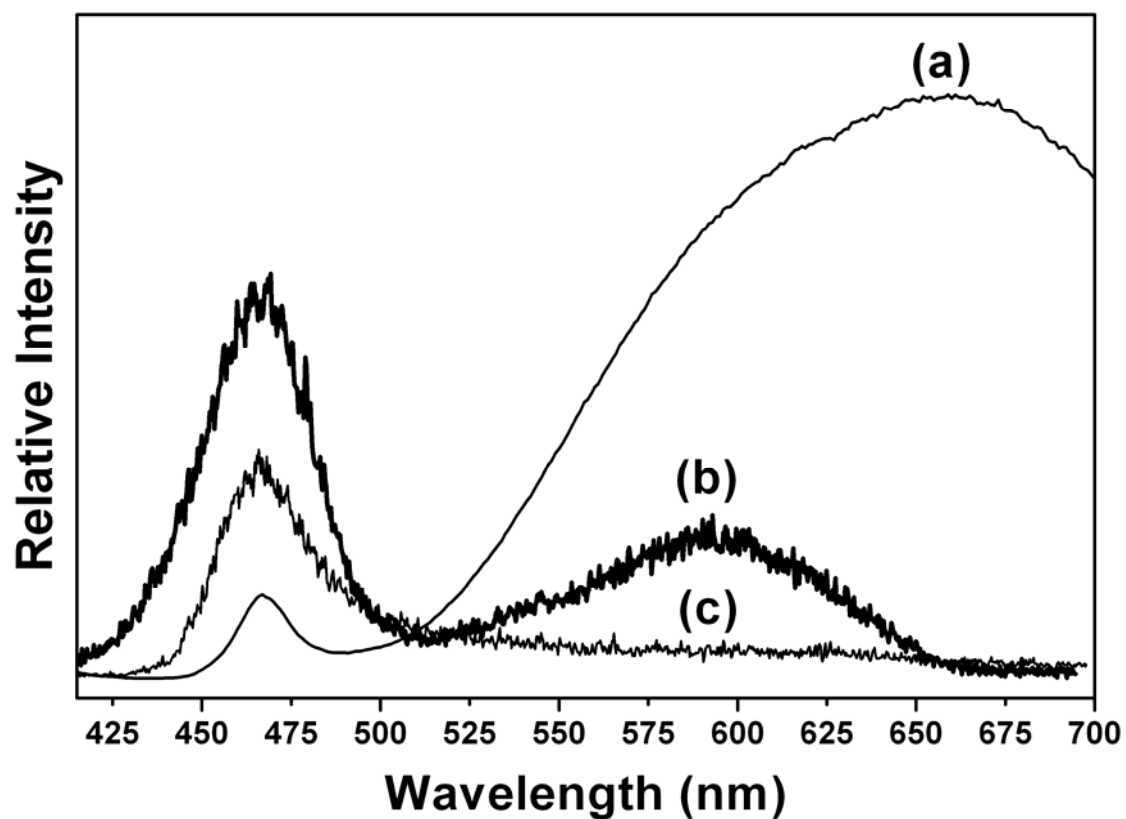


Figure 8. The normalized emission spectra of (a) CdS nanorods (synthesized by using TDPA and TOP) solution. (b) peripheral and (c) central region of a single array in the deposited thin film measured by a confocal microscope. The excitation wavelength is 406 nm (GaN laser) for all measurements.

Figure 9

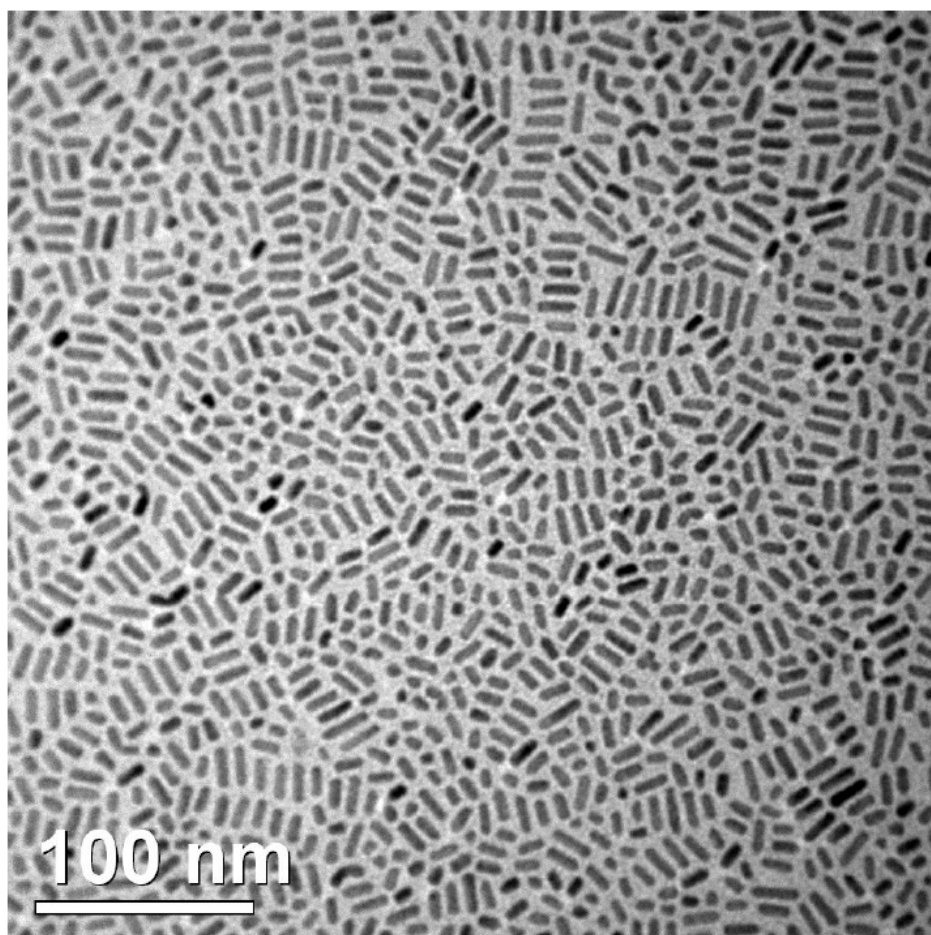


Figure 9. TEM image of a monolayer of CdS nanorods in the hole of a Quantifoil grid.

Figure 10

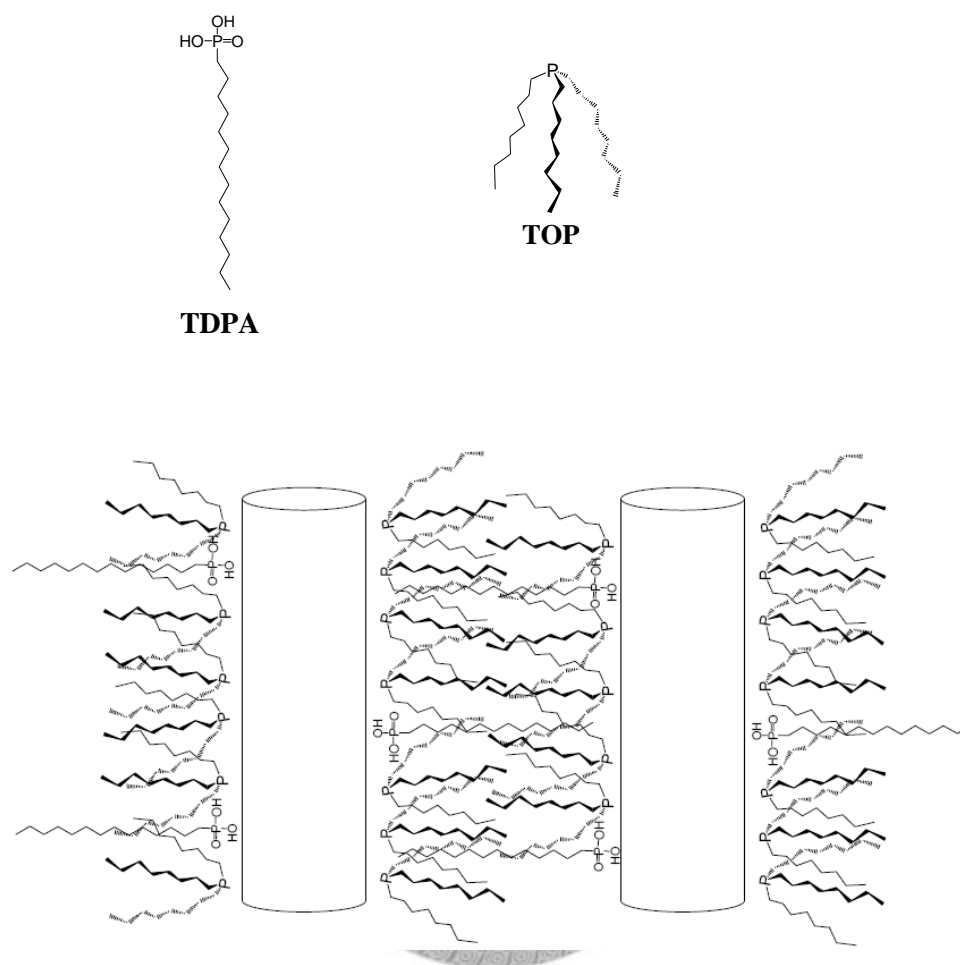


Figure 10. Proposed model of self-assembled CdS arrays synthesized by using TDPA and TOP as surfactants.

Figure 11

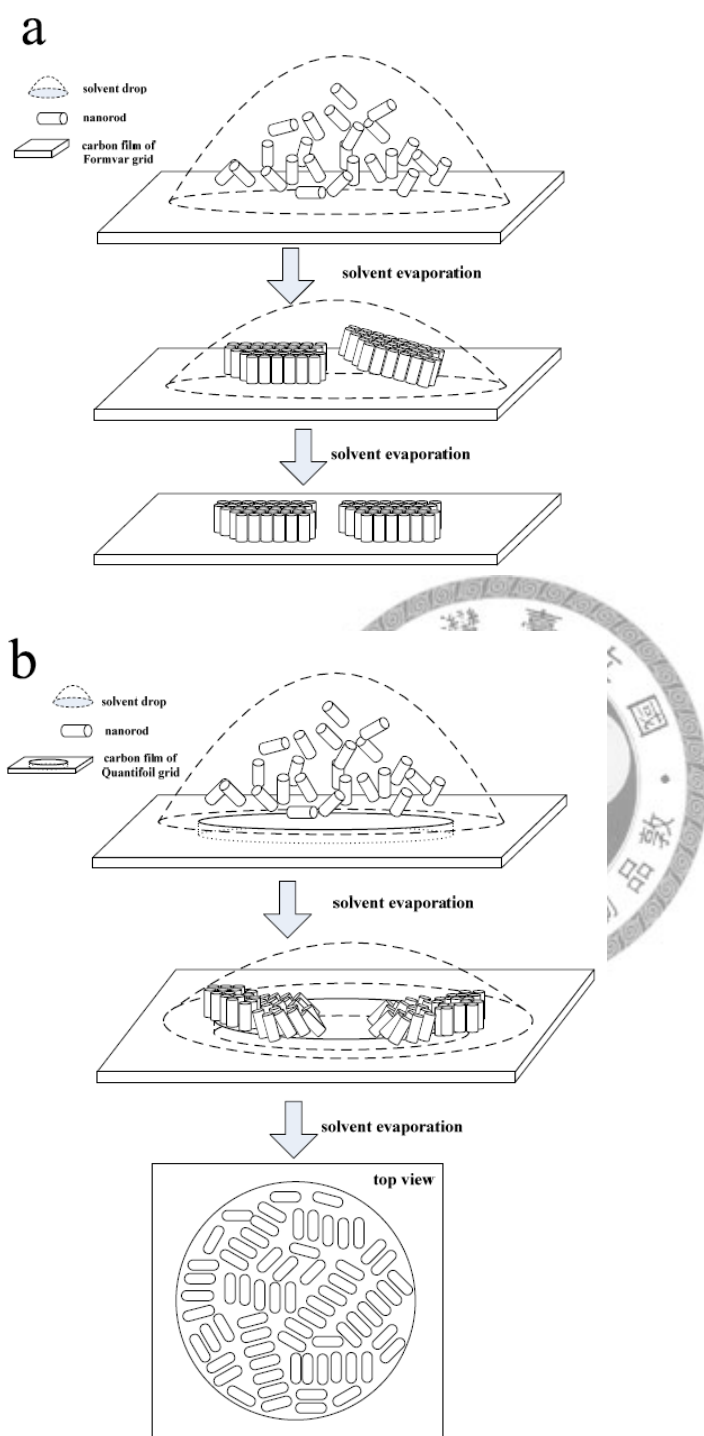


Figure 11. Drawings that illustrate the corraling behavior of CdS nanorods upon the evaporation of solvent on (a) Formvar grid and (b) Quantifoil grid.

Figure 12

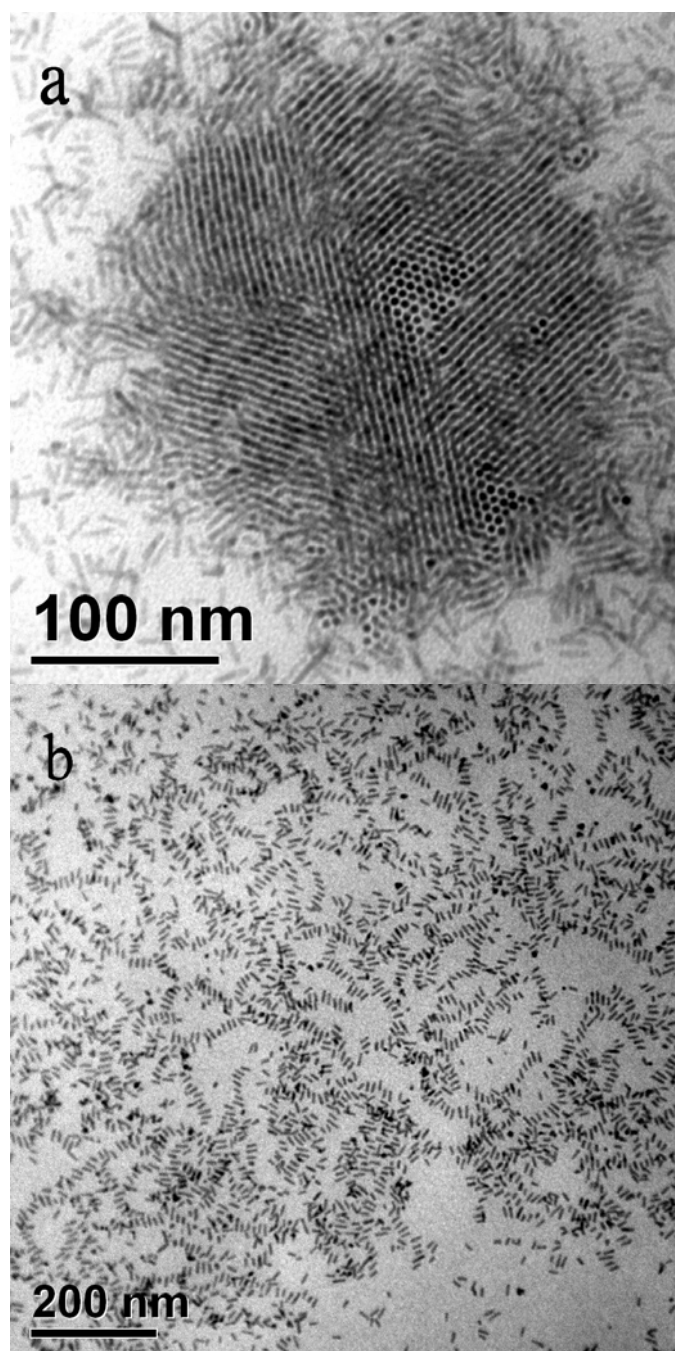


Figure 12. TEM images of CdS nanorods synthesized by using (a) ODPA, TOPO, and TOP and (b) ODPA and TOP.

Figure 13

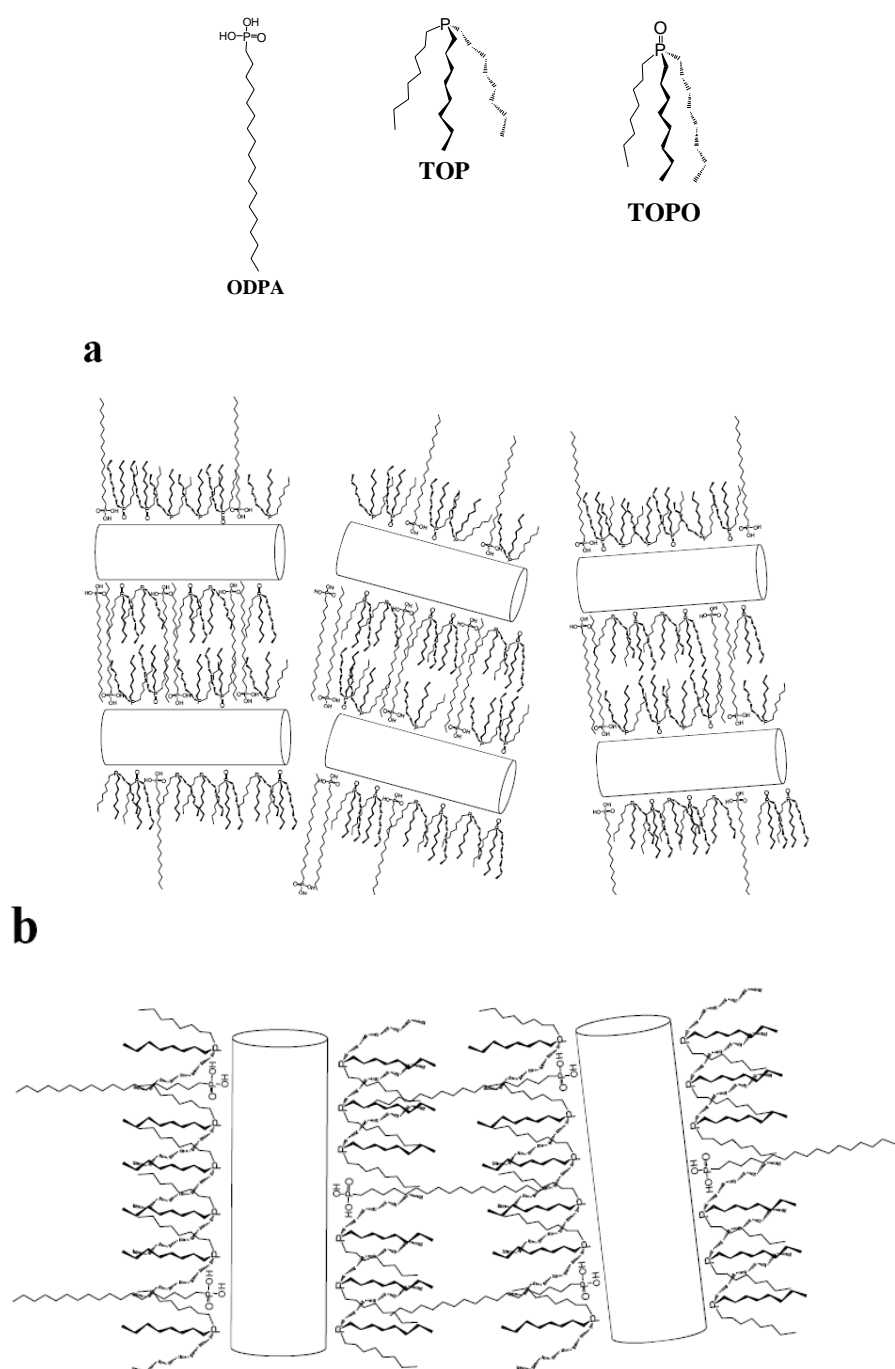


Figure 13. Proposed model of formation of CdS nanorods synthesized by using (a)

ODPA, TOPO, and TOP and (b) ODPA and TOP.

Figure 14

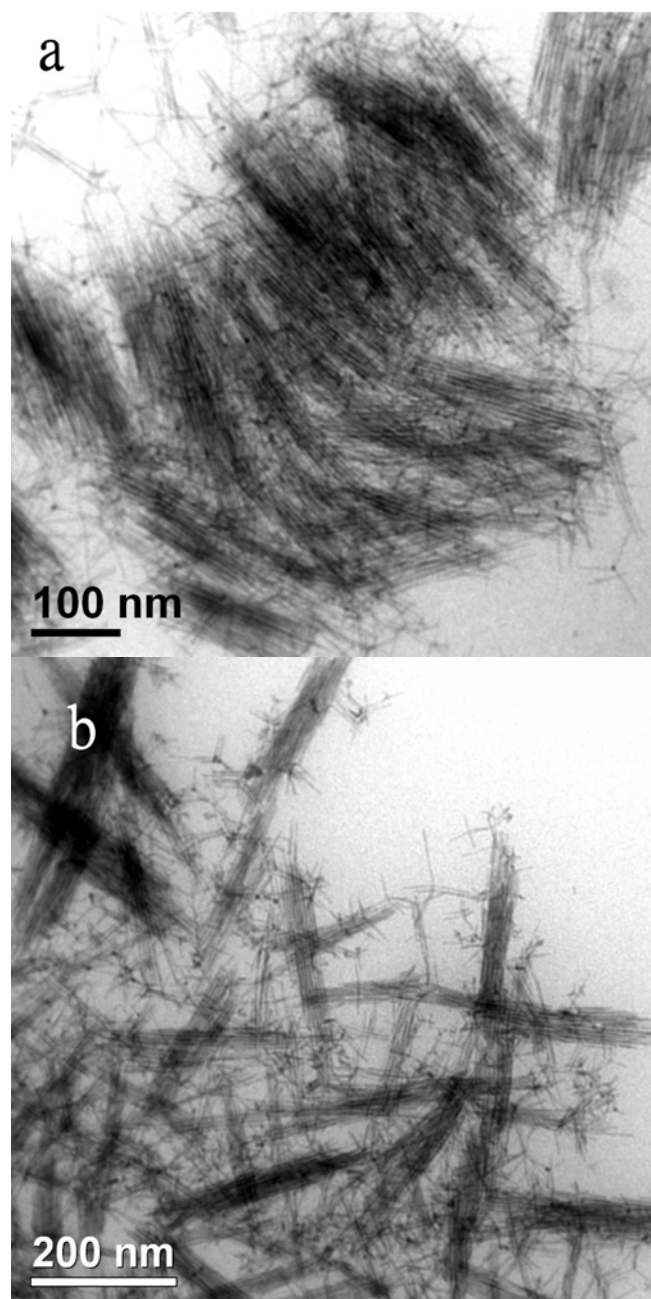
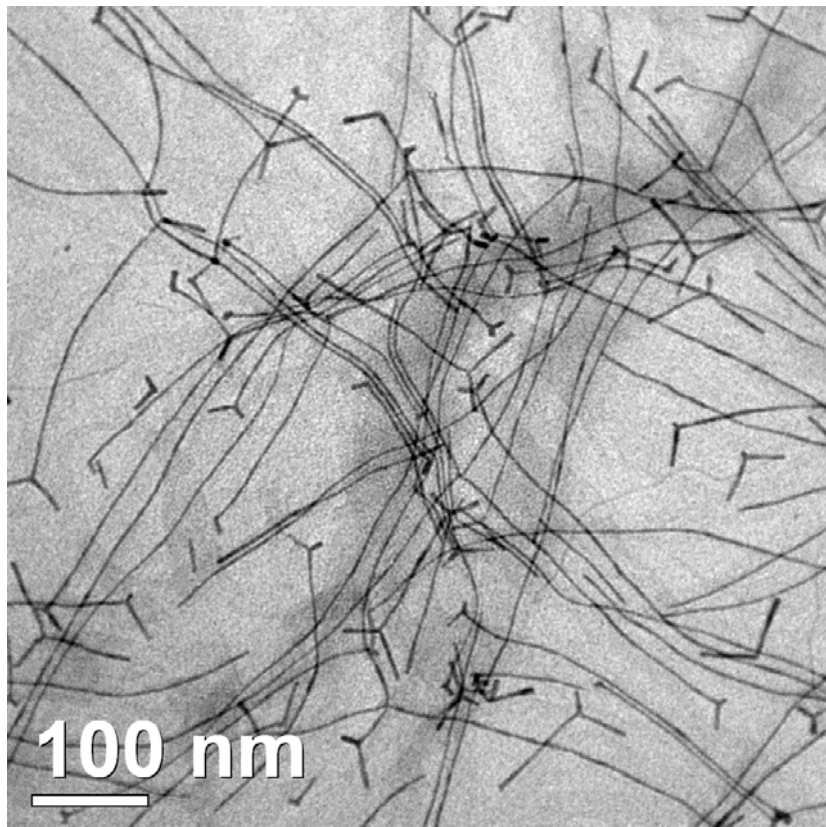


Figure 14. TEM images of CdS nanorods synthesized by using (a) OPA, TOPO, and TOP and (b) OPA and TOP.

Chapter 4.

Surfactant/Temperature Controlled CdS Nanowires Formation



Abstract

By optimizing the use of surfactants, we report the solution-based growth of CdS nanowires from either zinc blende or wurtzite structure. The aspect ratio can be tuned by varying temperatures. This simple and straightforward synthetic route may open a new door to the bottom-up synthesis of semiconductor nanowires.

1. Introduction

Besides nanorods, the 2D-confined nanowires show promising applications in the field of nanoelectronics,¹⁻³ photoconductivity,⁴⁻⁶ lasing,⁷⁻⁹ and sensing.¹⁰⁻¹³ There have been studies that nanowires, with width similar to that of nanorods, could be obtained either according to solution-liquid-solution (SLS) mechanism¹⁴⁻²⁰ or by spontaneous organization of single nanoparticles, known as oriented attachment.²¹⁻²³ In SLS mechanism, metal nanoparticles are involved in the reaction by providing catalytic sites for both precursor adsorption and decomposition. With the assistance of these supersaturated liquid droplets, nucleation takes place with subsequent growth of the nanowires. On the other hand, in the oriented attachment method, CdTe²¹ and PbSe²² nanocrystals unidirectionally self-assemble to nanowires due to the dipole-dipole attraction and dipolar interactions, respectively. The intermediate state of the pearl necklace aggregation was also observed. In 2006, by using alkylamines as the surfactant, Peng and the co-workers²³ also reported the syntheses of CdSe nanowires, in which the oriented attachment was achieved by the relatively weak interaction between the magic-sized cluster precursors. Herein, we report a facile solution-based synthesis of CdS nanowires free from metal catalysts. Although synthesis of short nanorods by using mixture of surfactants has been studied widely, to our knowledge, until the present day, the synthesis of catalyst free CdS nanowires by using mixture of surfactants has not

been achieved yet.

By simply varying temperatures, the aspect ratio of nanowires with diameter of 3.5 nm can be tuned up to 300. More importantly, on the basis of high resolution transmission electron microscope (HRTEM) analysis, the seeding site can be either zinc blende or wurtzite structure, while the wire is in a wurtzite structure. These findings imply that the above mentioned selective-adsorption mechanism could be extended and suited for interpreting the kinetics driven growth of CdS nanowires.

2. Experimental Section



In brief, a sulfur injection solution containing 0.072 g of sulfur (2.25 mmol) was prepared by dissolving sulfur powder in 2 mL of tri-n-octylphosphine. 0.1 g of CdO (0.78 mmol) and 0.4565 g of TDPA (1.64 mmol) were loaded into a 50 mL three-neck flask and heated to 200°C under Ar flow. After the CdO was completely dissolved, judging by the vanishment of the brown color of CdO, the Cd-TDPA complex was allowed to cool down to room temperature. Subsequently, 1.35 g of TOPO was added to the flask, and the temperature was raised to 320°C to produce an optically clear solution.

As for the subsequent addition of the sulfur precursor, through optimization, four prototypical experiments for growing distinct CdS nanowires are presented here. (A) after the sulfur injection to a 320°C mixture containing Cd-TDPA complex and TOPO, the temperature of the reaction system was dropped to and maintained at 280°C throughout the end of reaction (B) The temperature of the reaction system was allowed to cool down to 280°C (due to the sulfur injection) and subsequently raise to 315°C for the crystal growth. (C) Prior to injection, the sulfur solution was initially heated to 320°C so that the temperature of the system remained unchanged amid injection. Note this pre-heating step is to avoid the prompt temperature fluctuation when the sulfur precursor is introduced into the reaction system. (D) Similar to process (C) except that the pre-heated sulfur solution was pre-heated to 330°C prior to the injection into a 330°C reaction mixture. Note that despite the temperature equivalence, the injection still caused a 5°C decrease of the temperature, which was then re-heated and maintained at 330°C. For (A)-(D) the reaction was lasted for 5 minutes to allow the growth of CdS crystals with different lengths and then was terminated by quenching the reaction to 40°C. Subsequently, 5 mL of toluene was introduced to dissolve the reaction mixture, and yellow precipitate was obtained by adding 5 mL of isopropanol followed by centrifugation at 3000 rpm. The precipitate was dispersed in toluene for the TEM characterization, and dried powder of the precipitate was used for the XRD

measurement.

The shapes and size distributions of the nanocrystals were measured with a JEOL JEM 1230 transmission electron microscope (TEM), and high resolution (HRTEM) images were taken with a JEOL JEM 2100F. The conventional Formvar coated 200 mesh Cu grids were used. The crystal structure and phases of the synthesized samples were analyzed by X-ray powder diffraction (XRD) on a PANalytical X'Pert PRO with Cu K α X-ray. UV/Vis steady-state absorption and emission spectra were recorded with a Hitachi (U-3310) spectrophotometer and an Edinburgh (FS920) fluorimeter, respectively.



3. Results and Discussions

We have made attempts to prepare CdS nanowires by virtually using the method to prepare CdX (X= Te, Se and S) nanorods with CdO as a precursor.²⁴ Adopting the same surfactant mixtures reported, i.e. a combination of hexylphosphonic acid (HPA), tetradecylphosphonic acid (TDPA), trioctylphosphine oxide (TOPO) and trioctylphosphine (TOP), we could reproduce the CdS nanorods with a length in the range of 10-20 nm (aspect ratio: 3-5). However, intriguingly, upon optimizing the types of surfactants to only TDPA, TOPO and TOP as well as their respective molar ratio, we

then successfully obtained CdS nanowires with aspect ratio varied from 20 to 300, depending on the controlled temperature elaborated in the experimental section (vide infra).

Figures 1a-d show the transmission electron microscope (TEM) images of CdS nanocrystals synthesized under different temperatures. Figure 1a depicts the TEM results of CdS nanorods prepared at 280°C (process (A), see experimental section). Clearly, nanorods with 3 nm in width and 30-50 nm in length are observed, in part, accompanied by the formation of tetrapod. The results are in consistent with that reported previously.²⁴ As reported by Alivisatos²⁵ and Peng,²⁶⁻²⁸ during the nucleation stage of the CdS and CdSe systems, magic-sized zinc blende structured seeds tend to be more stable at lower temperature, which promotes the formation of elongated structure with nearly monodisperse lateral dimension. However, since the energy difference between zinc-blende and wurtzite phases is merely a few meV for CdSe, CdS, and ZnS,²⁵ at 280°C, formation of CdS nanocrystal exclusively in one phase seems to be impractical, rationalizing the existence of tetrapods and nanorods for the as-prepared samples. Upon elevating the reaction temperature from 280°C to 315°C, i.e. the process (B, see experimental section), as shown in Figure 1b, the width of the nanocrystals increases only slightly from 3 nm to 3.5 nm, while the length drastically increases to as long as 300 nm.

Since the only difference between processes (A) and (B) is temperature, it seems that the length of CdS nanocrystals is determined by the growth rate along the c-axis of a wurtzite structure. Accordingly, we anticipate to produce longer nanowires upon increasing and maintaining of the reaction system at higher temperature than 315°C. To support this viewpoint, methods (C) and (D) were conducted, in which the temperature for growing nanocrystals was set to be at 320°C and 330°C, respectively. It is noteworthy that the added sulfur solution in (C) and (D) processes was kept at the designated temperature in order to avoid sudden temperature drop upon swift sulfur injection. The results, shown in Figure 1c and 1d for (C) and (D), respectively, clearly demonstrate a nearly unchanged width of the CdS nanowires, whereas the aspect ratio is increased, i.e. the elongation of the c-axis, as temperature is increased from 315, 320 to 330°C. At 330°C, CdS nanowires with an aspect ratio of as large as 300 were obtained.

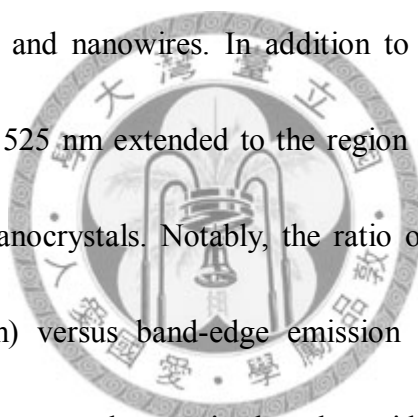
As depicted in Figure 2, X-ray powder diffraction (XRD) pattern of the elongated nanowires prepared at 320°C (upper part of Figure 2) shows the diffraction peaks matching exactly that of the wurtzite CdS standard pattern (lower part of Figure 2). The significantly sharp and narrowed (002) peak at the 26.7 degrees (2θ) clearly supports the extended c-axis stacking domain of the wurtzite lattice. Note the broadening of other peaks is due to the corresponding quantized dimensions. Though not shown here, a similar structure was obtained for CdS nanowires prepared at 315 and 330°C.

The anisotropic growth of the nanocrystals is viewed to be due to the high monomer concentration after nucleation stage,^{26,28,29} which is achieved by applying strong ligands, namely, TDPA, to form a stable complex with cadmium (Cd-TDPA). During the growth stage of nanorods, phosphonic acid molecules tend to selectively bind the lateral facets of the rods. Accordingly, the growth rate of the (00 ℓ) facet of CdS is increased, resulting in the anisotropic growth along c-axis of the wurtzite structure.²⁵

Intriguingly, in addition to the nanowires with solely wurtzite structure, imagery of TEM (Figure 3) and high resolution transmission electron microscopy (HRTEM, see insert of Figure 3) reveals certain CdS nanowires originating from a zinc-blende structure, while the arms possess a wurtzite structure. As shown in insert of Figure 3, the lattice spacing of the arm possesses a wurtzite structure, which is elongated along the c-axis. The 109.5° separation angle between the {111} faces refers to that the core of the bipods is zinc-blende structure with a <-110> zone axis. The wurtzite-structured arms are clearly epitaxially grown from the {111} plane of the zinc-blende core. Note the HRTEM of bipods shown in insert of Figure 3 is reminiscent of that reported by Alivisatos et al. and Cheon et al.^{29,30} That is, wurtzite-structured arms epitaxially grow along the c-axis from {111} planes of a zinc blende core, with an angle of 109.5 degrees between the arms.

The fast growth of the anisotropic nanocrystals might accompany with an increase

of the defect sites and the existence of which could perhaps be examined by the photoluminescence of the as-prepared nanorods and nanowires. Accordingly, UV/Vis steady-state absorption and emission spectra of CdS nanocrystals were performed and the results are shown in Figure 4. As depicted in Figure 4, independent of the temperature, the appearance of the first exciton peak at 450 nm indicates that there is a control of the size distribution ($\sim 3.5 \pm 0.2$ nm) at the transverse direction. Thus the corresponding luminescence peak around 455 nm originates from the band edge of the as-prepared CdS nanorods and nanowires. In addition to the excitonic emission, the broad band emission from 525 nm extended to the region of near infrared arises from the defect states of CdS nanocrystals. Notably, the ratio of emission intensity for the defect emission (~ 525 nm) versus band-edge emission (455 nm) increases as the anisotropic nanocrystals become longer in length, evidently representing a faster growing rate induced by the increase of temperature. Another indirect support of this viewpoint may be given in an attempt to grow other II-VI semiconductor nanowires. Based on a similar method, we have also made a great deal of efforts in attaining CdSe and CdTe nanowires. Unfortunately, similar approaches failed, plausibly due to a lower temperature required to form CdSe (CdTe) nanocrystals. Finally, attempts have also been made to further increase the temperature above 340°C to grow CdS nanowires. However, the results of TEM (not shown here) show CdS nanowires with a decrease of



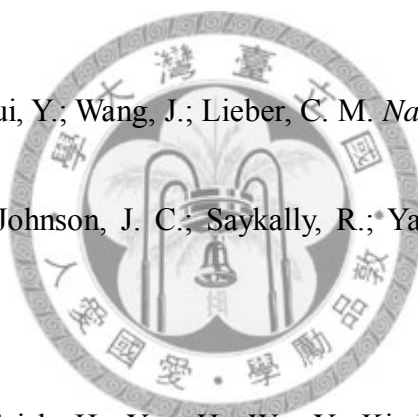
aspect ratio. We tentatively attribute the results to the possible reaching to the azeotrope of the mixture at $> 340^{\circ}\text{C}$, as evidenced by the boiling of the solution, the turbulence from which may perturb the CdS crystal growth. Nevertheless, more robust explanation is pending resolution.

4. Conclusion

To sum up, CdS nanowires with aspect ratio as large as 300 are reported by using a solution-based synthesis. The optimization of surfactants to enhance anisotropic elongation plays an important role in this approach. This, in combination with the temperature-dependent growth rate on the (001) direction of the wurtzite structure, makes feasible the tuning of CdS nanowires in length. Previous studies have shown that nanowires of II-VI semiconductors could be formed by SLS methods and oriented attachment of nanoparticles. Experimental results demonstrated here imply that the selective-adsorption mechanism could be extended to explain the formation of semiconductor nanowires. Owing to the promising applications of 2D-confined nanowires in nanoelectronics and photovoltaic devices, etc, we thus believe that the simple, straightforward and reproducible solution-based synthesis of CdS nanowires reported here may spark a broad spectrum of interest in the in the fields of nanoscience and nanotechnology.

6. References

- (1) Cui, Y.; Duan, X.; Hu, J.; Lieber C. M. *J. Phys. Chem. B* **2000**, *104*, 5213-5216.
- (2) Cui, Y. ; Lieber, C. M. *Science* **2001**, *291*, 851-853.
- (3) Huang, Y.; Duan, X.; Cui, Y.; Lauhon, L. J.; Kim, K. H. ; Lieber, C. M. *Science* **2001**, *294*, 1313-1317.
- (4) Wang, J. ; Gudiksen, M. S. ; Duan, X. ; Cui, Y. ; Lieber, C. M. *Science* **2001**, *293*, 1455-1457.
- (5) Duan, X.; Huang, Y.; Cui, Y.; Wang, J.; Lieber, C. M. *Nature* **2001**, *409*, 66-69.
- (6) Law, M.; Greene, L.; Johnson, J. C.; Saykally, R.; Yang, P. *Nat. Mater.* **2005**, *4*, 455-459.
- (7) Huang, M.; Mao, S.; Feick, H.; Yan, H.; Wu, Y.; Kind, H.; Weber, E.; Russo, R.; Yang, P. *Science* **2001**, *292*, 1897-1899.
- (8) Duan, X.; Huang, Y.; Agarwal, R.; Lieber, C. M. *Nature* **2003**, *421*, 241-245.
- (9) Jing, Y.; Zhang, W. J.; Jie, J. S.; Meng, X. M.; Zapien, J. A.; Lee, S. T. *Adv. Mater.* **2006**, *18*, 1527-1532.
- (10) Cui, Y.; Wei, Q. Q.; Park, H. K.; Lieber, C. M. *Science* **2001**, *293*, 1289-1292.
- (11) Favier, F.; Walter, E. C.; Zach, M. P.; Benter, T.; Penner, R. M. *Science* **2001**, *293*, 2227-2231.



- (12) Law, M.; Kind, H.; Messer, B.; Kim, F.; Yang, P. *Angew. Chem. Int. Ed.* **2002**, *41*, 2405-2408.
- (13) Li, J.; Ng, H. T.; Cassel, A.; Fan, W.; Chen, H.; Ye, Q.; Koehne, J.; Han, J.; Meyyappan, M. *Nano Lett.* **2003**, *3*, 597-602.
- (14) Trentler, T. J.; Hickman, K. M.; Goel, S. C.; Viano, A. M.; Gibbons, P. C.; Buhro, W. E. *Science* **1995**, *270*, 1791-1794.
- (15) Yu, H.; Gibbons, P. C.; Kelton, K. F.; Buhro, W. E. *J. Am. Chem. Soc.* **2001**, *123*, 9198-9199.
- (16) Yu, H.; Li, J.; Loomis, R. A.; Wang, L. W.; Buhro, W. E. *Nat. Mater.* **2003**, *2*, 517-520.
- (17) Buhro, W. E.; Colvin, V. L. *Nat. Mater.* **2003**, *2*, 138-139.
- (18) Yu, H.; Buhro, W. E. *Adv. Mater.* **2003**, *15*, 416-419.
- (19) Yu, H.; Li, J.; Loomis, R. A.; Patrick, C. G.; Wang, L. W.; Buhro, W. E. *J. Am. Chem. Soc.* **2003**, *125*, 16168-16169.
- (20) Wang, F.; Dong, A.; Sun, J.; Tang, R.; Yu, H.; Buhro, W. E. *Inorg. Chem.* **2006**, *45*, 7511-7521.
- (21) Tang, Z.; Kotov, N. A.; Giersig, M. *Science* **2002**, *297*, 237-240.
- (22) Cho, K. S.; Talapin, D. V.; Gaschler, W.; Murray, C. B. *J. Am. Chem. Soc.* **2005**,



127, 7140-7147.

(23) Prashan, N.; Xu, H.; Peng, X. *Nano Lett.* **2006**, *6*, 720-724.

(24) Peng, Z. A.; Peng, X. G. *J. Am. Chem. Soc.* **2001**, *123*, 183-184.

(25) Manna, L.; Milliron, D. J.; Meisel, A.; Scher, E. C.; Alivisatos, A. P. *Nat. Mater.* **2003**, *2*, 382-385.

(26) Peng, Z. A.; Peng, X. G. *J. Am. Chem. Soc.* **2001**, *123*, 1389-1395.

(27) Peng, Z. A.; Peng, X. G. *J. Am. Chem. Soc.* **2002**, *124*, 3343-3353.

(28) Peng, X. G. *Adv. Mater.* **2003**, *15*, 459-463.

(29) Manna, L.; Scher, E. C.; Alivisatos, A. P. *J. Am. Chem. Soc.* **2000**, *122*, 12700-12706.

(30) Jun, Y. W.; Lee, S. M.; Kang, N. J.; Cheon, J. W. *J. Am. Chem. Soc.* **2001**, *123*, 5150-5151.

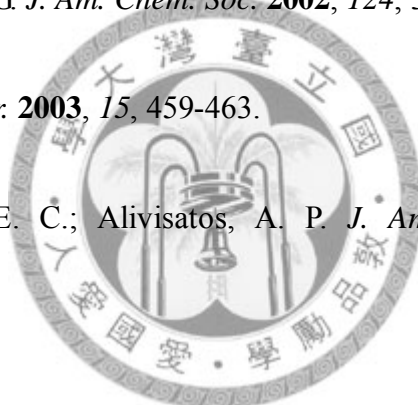


Figure 1

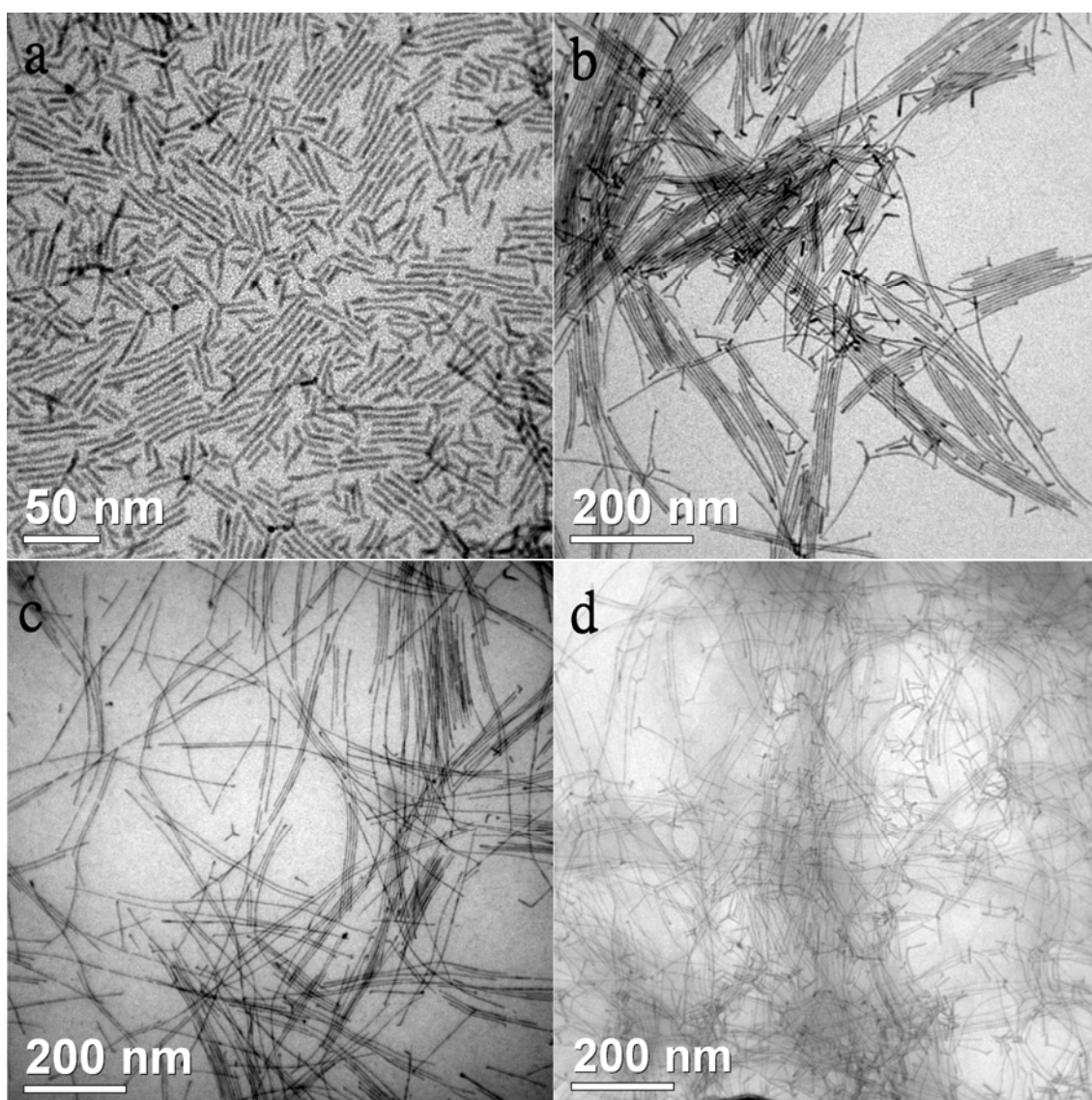


Figure 1. TEM images of CdS nanocrystals synthesized under different temperatures of (a) 280°C, (b) 315°C, (c) 320°C and (d) 330°C.

Figure 2

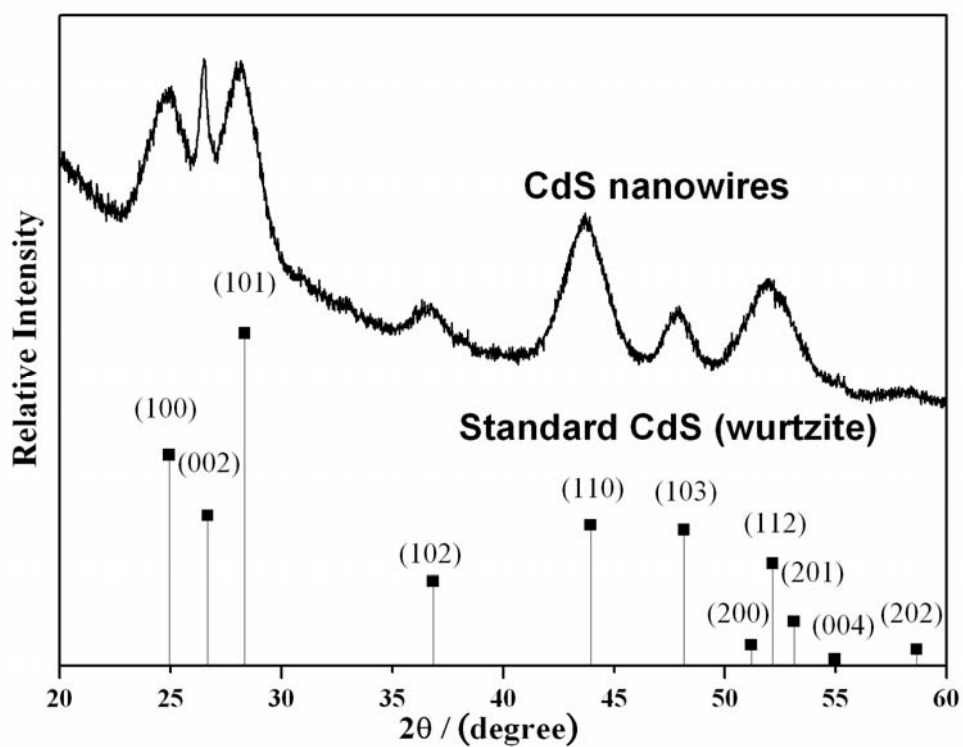


Figure 2. Powder X-ray diffraction (XRD) of CdS nanocrystals synthesized under 320 °C (upper) and that of standard CdS (wurtzite) pattern (lower).

Figure 3

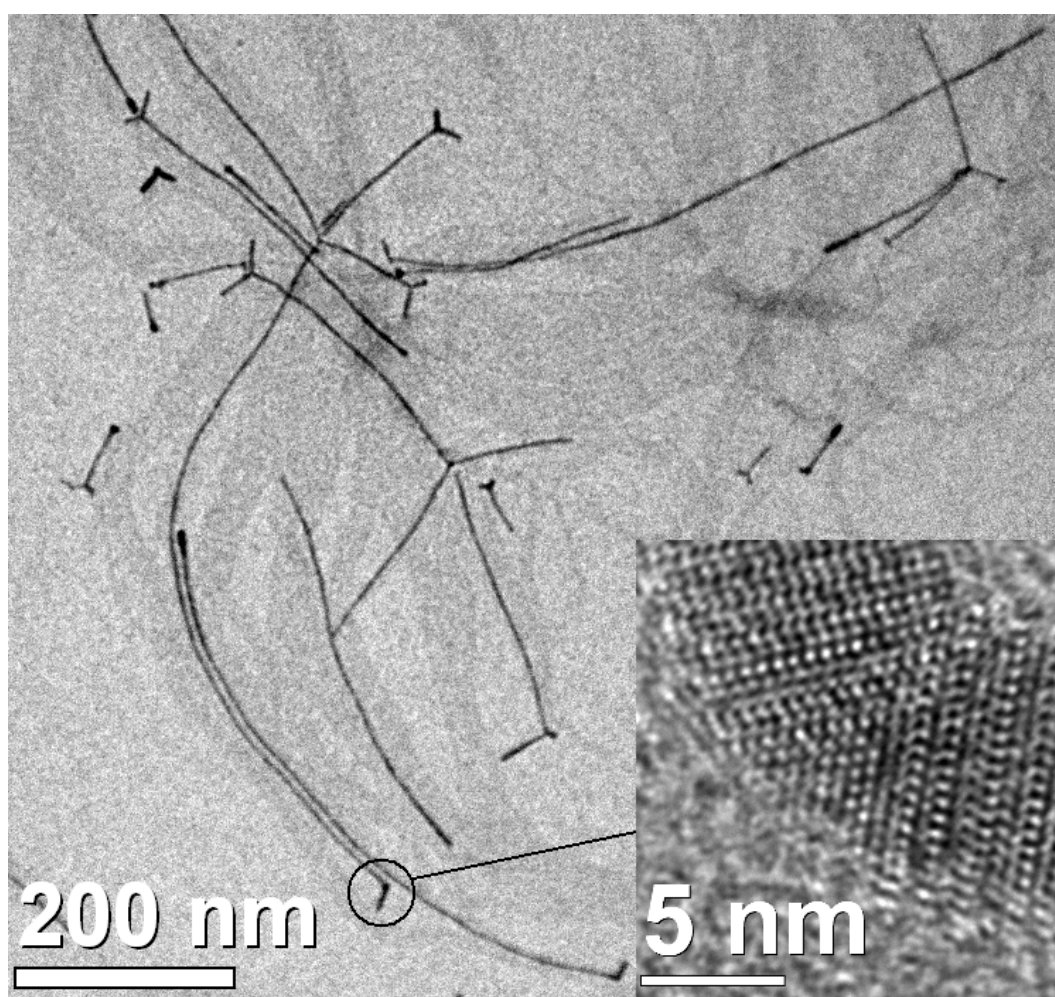


Figure 3. A prototype of CdS nanowires synthesized under 330°C. HRTEM image (inset) clearly shows the junction of bipod that consists with a zinc-blende core with wurtzite arms epitaxially grown from the {111} plane of the core.

Figure 4

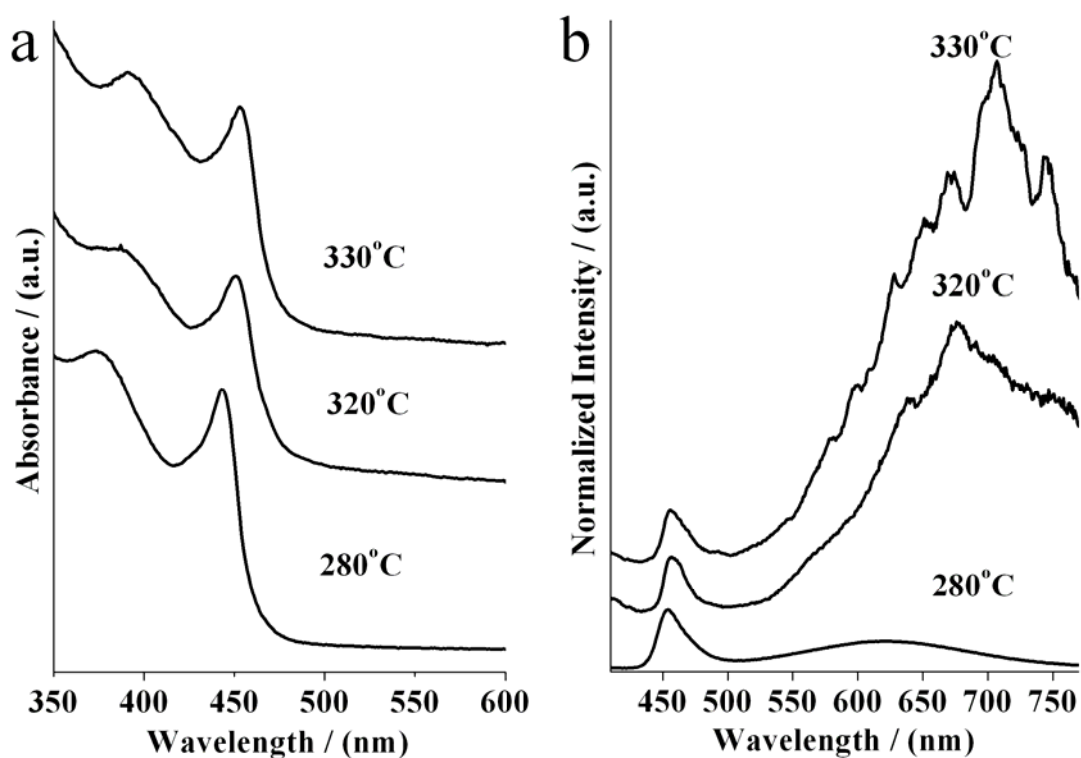
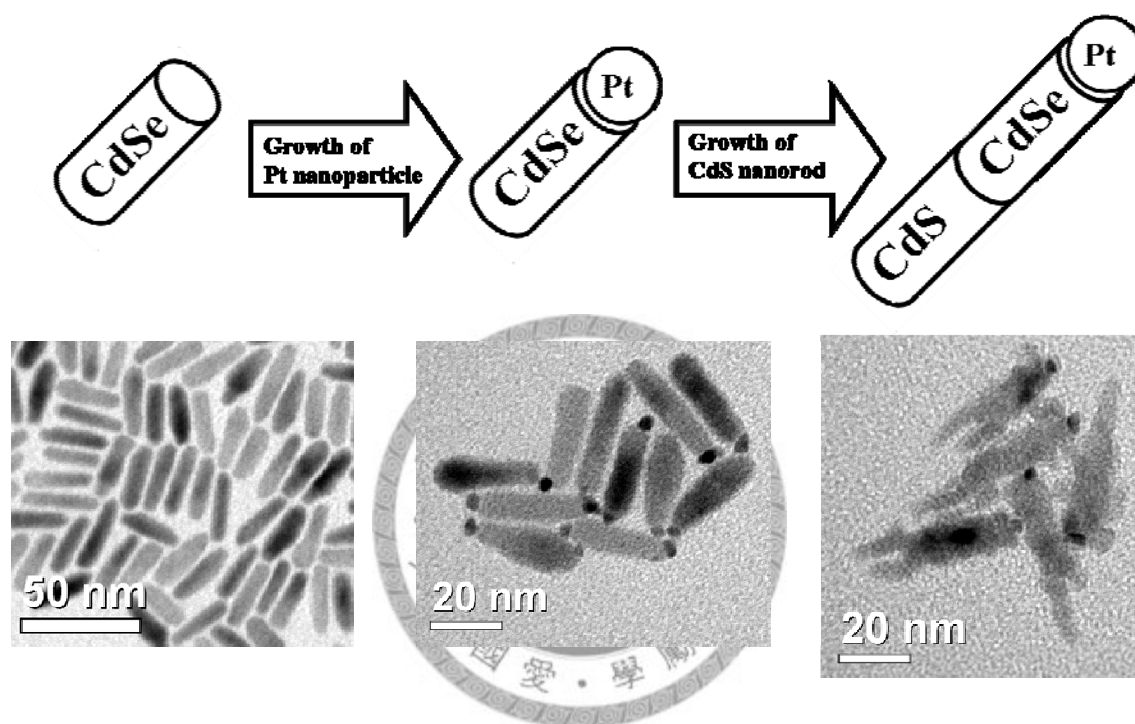


Figure 4. (a) absorption and (b) emission spectra of CdS nanocrystals synthesized under different temperatures. Solvent: toluene. The excitation wavelength was fixed at 400 nm for all emission spectra. (note: The multiple peaks at longer wavelength of the defect emission prepared at 320°C and 330°C are due to the increase of scattering light upon increasing the length of CdS, such that some stray light from the excitation lamp was accidentally acquired.)

Chapter 5.

Axial heterostructured Pt-CdSe-CdS semiconducting nanorods



Abstract

Recently, heterojunction structure of one-dimensional (1D) semiconducting nanorods, with distinct intersection between each segment, could be fabricated without the need of organic linkers. This emerging field in nanoscience represents an effective approach in fine tuning chemical and physical properties of nanocrystals. By incorporation of different nanostructured components, multifunctional capabilities with tunable or enhanced characteristics could be achieved in the hybrid nanostructures. In

this study, Pt-CdSe-CdS heterojunctioned nanorods are produced via a different methodology from the solution-liquid-solid (SLS) method. By controlling the ratio of nanorods and Pt-precursor, matchstick structured nanorods, with single tip of Pt nanoparticles on one end of CdSe nanorods, are synthesized in advance. The function of Pt nanoparticles is therefore viewed as a protecting group, namely blocking one terminal of CdSe nanorods. Second segment of CdS nanorods is sequentially grown on the unprotecting side of CdSe nanorods. The result shown in this report could help tailoring the complex heterojunction nanocrystals in the field of nanomaterial-architecture.



1. Introduction

Over the past decade, fabrication of one-dimensional (1D) semiconducting nanocrystals has drawn much attention because of the fascinating size and shape dependent optical and electronic properties.¹⁻⁵ These phenomena make 1D semiconducting nanocrystals good candidates for fundamental studies and possible technological applications in various fields, such as lasing,⁶ electroluminescence,^{7,8} photovoltaics,^{9,10} and nanoelectronics.^{11,12} Also, numerous reports have been published about synthetic routes and growth mechanism of nanorods with well-controlled size and

aspect ratios.¹³⁻²⁹

Recently, heterojunction structure of 1D semiconducting nanorods, with distinct intersection between each segment, could be fabricated without the need of organic linkers.³⁰⁻⁴⁷ This emerging field in nanoscience represents an effective approach in fine tuning chemical and physical properties of nanocrystals. By incorporation of different nanostructured components, multifunctional capabilities with tunable or enhanced characteristics could be achieved in the hybrid nanostructures. Among them, metallic tips grown on nanorods by using reduction^{30-32,44} or other routes³⁴ could serve as preferential anchoring points for connecting nanorods in different surroundings or have potential in catalytic reaction. Besides, By sequential chalcogenide precursor injection, maintaining the monomer concentration in the stage of 1D growth, CdS/CdTe/CdS³⁷ and CdTe/CdSe/CdTe^{37,38,48,49} heterostructured nanorods could be obtained, and different optical properties were also reported. In addition, by incorporating nanoparticles (CdSe, CdTe, ZnTe, or ZnSe) as seeds, highly luminescent, self-assembled, or type-II heterostructured nanorods were synthesized via seed-mediated growth approach.^{42,43} Also, heterostructures such as tetrapods with cores and arms composed of different compositions, could be synthesized.^{43,50} Furthermore, upon injection of different kinds of chalcogenide precursor in solution-liquid-solution (SLS) growth with Bi nanoparticles as catalytic agents, axial heterostructured CdS/CdSe,

ZnSe/ZnTe, and heterobranch CdSe/ZnSe nanowires were produced.^{34-41,53} These studies set good examples in architecture of one-dimensional nanomaterials. Since the multifunctionally heterostructured nanocrystals are of great interest, a general approach to selectively fabricate 1D heterostructured nanorods would be essential in designing the synthetic route of nanomaterials.

Bearing the idea in mind, we thus tentatively search a possibility of adjusting the role of metallic nanoparticles during the synthesis of 1D heterojunction nanorods. Concerning general chemical synthesis, protecting group often refers to the site with lower activity. In the structure of a nanorod, two ends on the long axis are thought to be more reactive than other facets due to the effective-monomer model.^{14,15,51,52} In this study, by controlling the ratio of nanorods and Pt-precursor, a matchstick structured, with single tip of Pt nanoparticles on one end of CdSe nanorods, were synthesized. The function of Pt nanoparticles is therefore viewed as a protecting group, namely blocking one terminal of CdSe nanorods. Second segment of CdS nanorod is sequentially grown on the unprotected side of CdSe nanorods. The concept and experimental results shown in this report, in combination with traditional methodology of chemical synthesis, might help in tailoring the flexibility of complex heterostructured nanocrystals, and hence further support the development of multifunctional nanomaterials and devices in nanoscale.

2. Experimental Section

Hexylphosphonic acid (HPA, 98%) and Tetradecylphosphonic acid (TDPA, 98%) were purchased from Alfa Aesar. Tri-*n*-octylphosphine (TOP, > 85 %) and *n*-hexadecylamine (HDA, 90%) were purchased from TCI. Tri-*n*-octylphosphine oxide (TOPO, 90%) was purchased from Fluka. Cadmium oxide (CdO, 99.99%) powder was obtained from Strem Chemicals. Selenium (Se, 99.5%) powder, oleic acid (90%), oleylamine (90 %), and diphenylether (95 %) were obtained from ACROS. 1,2-hexadecanediol (90%), platinum acetylacetonate (97%), and 1-octadecene (90%) were obtained from Aldrich. Chemicals were used as received.

Synthesis of CdSe nanorods

CdSe nanorods were synthesized according to the literature methods with modification of varying surfactants.¹⁵ Briefly, a selenium injection solution containing 0.073 g of selenium was prepared by dissolving selenium powder in 1 mL of tri-*n*-octylphosphine. 0.2 g of CdO, 0.71 g of TDPA, 0.16 g of HPA, and 3 g of TOPO were loaded into a 50 mL three-neck flask and heated to 320 °C under Ar flow. After the CdO was completely dissolved, judging by the disappearance of the brown color of CdO, the temperature of reaction system was kept for 30 minutes. Subsequently, the selenium injection solution was swiftly injected into the hot solution. The reaction

mixture was maintained at 320 °C for growth of CdSe crystals. After 5 minutes, the temperature was quenched to 40 °C to terminate the reaction. 5 mL of toluene was then introduced to dissolve the reaction mixture, and dark-red precipitate was obtained by adding 5 mL of isopropanol and centrifuged at 3,000 rpm for 5 minutes. The precipitate was washed with toluene and isopropanol three times and re-dispersed in toluene for further measurements.

Synthesis of matchstick structured Pt-CdSe nanorods

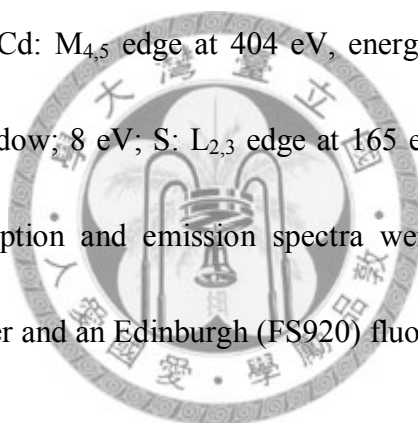
For the synthesis of Pt nanoparticles on one end of CdSe nanorods, Pt-CdSe nanocrystals were synthesized according to the Mokari's report,³⁴ with modification of precursor. Briefly, 0.1 mL of oleic acid, 0.1 mL of oleylamine, and 3.225 mg of 1,2-hexadecanediol were dissolved in 10 mL of diphenylether, and the temperature was raised to 80 °C under vacuum for 1 hour. Separately, 4.91 mg of Pt acetylacetonate and 10 mg of CdSe nanorods were added into 2 mL of dichlorobenzene and heated at 70 °C for 20 minutes. The mixture of surfactants and diphenylether was purged with argon and heated to 210 °C. Subsequently, the Pt injection solution was swiftly injected into the hot solution. After 5 minutes, the temperature was quenched to 40 °C to terminate the reaction. 40 mL of ethanol was then introduced to the reaction mixture, and solution was centrifuged at 3,000 rpm for 5 minutes. The precipitate was washed three times with ethanol and re-dispersed in toluene for characterizations and further experiments.

Synthesis of axial-heterostructured Pt-CdSe-CdS nanorods

The attempt of growing the second segment of nanorods, CdS, onto the preformed Pt-CdSe nanorods was done by using three different sets of surfactants. (A) TDPA, and TOP. (B) stearic acid and TOP. (C) oleic acid, 1-octadecene, and TOP. The Cd and S precursor were CdO and sulfur powder, respectively.

The stock solution was prepared by mixing CdO (5 mg) and surfactants in a 50 mL three necked flask. ((A) TDPA (0.1142 g) and TOP (4 mL). (B) stearic acid (0.1167 g) and TOP (4 mL). (C) oleic acid (1 mL) and 1-octadecene (4mL).) After the flask was pumped under vacuum for ~30 minutes, the mixture was heated to 320 °C under argon to yield a clear and colorless solution containing Cd complex. The temperature of reaction system was kept for 30 minutes. Subsequently, injection solution, containing 7.2 mg of sulfur, 1 mL of TOP, and 0.5 mL of Pt-CdSe solution, was swiftly injected into the flask. After reacting at 320 °C for 5 minutes, the temperature was quenched to 40 °C to terminate the reaction. In order to remove the remaining unreacted precursors and surfactants, 5 mL of toluene was introduced to dissolve the reaction mixture, and dark-brown precipitate was obtained by adding 5 mL of isopropanol followed by centrifugation at 2600 rpm. The precipitate was washed with toluene and isopropanol three times and re-dispersed in toluene for characterizations.

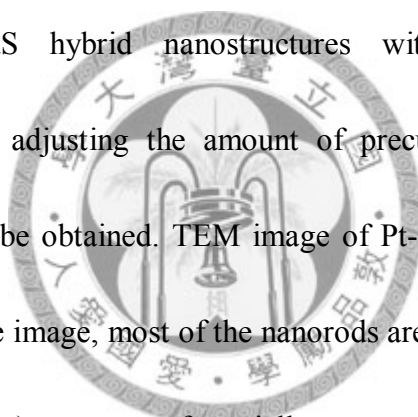
The shapes and size distributions of the nanocrystals were measured with a JEOL JEM 1230 transmission electron microscope (TEM). High resolution (HRTEM) images were taken with a JEOL JEM 2100F microscope operated at 200 kV. Experiments of X-ray energy dispersive spectroscopy (EDS) were performed by using a GENESIS 2000 EDS detector connected to the HRTEM instrument. The conventional Formvar coated 200 mesh Cu grids were used. Electron energy-loss spectroscopy (EELS) was acquired with a postcolumn filter (Tridium, Gatan, USA) using three energy windows near the absorption edge (Cd: $M_{4,5}$ edge at 404 eV, energy window; 60 eV; Se: $M_{4,5}$ edge at 57 eV, energy window; 8 eV; S: $L_{2,3}$ edge at 165 eV, energy window; 20eV). UV/Vis steady-state absorption and emission spectra were recorded with a Hitachi (U-3310) spectrophotometer and an Edinburgh (FS920) fluorimeter, respectively.



3. Results and Discussions

Figure 1a shows transmission electron microscope (TEM) image of as-synthesized CdSe nanorods. The diameter and length of nanorods are 8 ~ 8.5 nm and 30 ~ 35 nm, respectively. UV/Vis steady-state absorption and emission spectra of CdSe nanocrystals were performed, and Figure 1b clearly shows the first exciton peak at 670 nm and band edge emission around 675 nm of CdSe nanorods. The next step would be

blocking the undesired site, namely growing metallic or semiconducting nanocrystals on one end of the CdSe nanorod for protection. Comparing with semiconducting nanoparticles, synthetic conditions of metallic nanoparticles are much more simplified. After literature search, possibilities of introducing In, Bi, Sn, and Au nanoparticles are ruled out since they have been reported as candidates of catalytic droplets in solution-liquid-solid (SLS) reaction.^{53,54} Therefore, platinum (Pt) nanoparticles are chosen to serve as protecting agents. In 2009, Habas *et al.* synthesized Pt-CdS, PtNi-CdS, and PtCo-CdS hybrid nanostructures with controllable size and composition.³⁴ By simply adjusting the amount of precursors, Pt-CdSe matchstick structured nanorods could be obtained. TEM image of Pt-CdSe nanorods is shown in Figure 2a. Judging from the image, most of the nanorods are matchstick structured, with Pt nanoparticles (4 ~ 5 nm) grown preferentially on one tip of the CdSe nanorods. According to Peng's¹⁴ and Mokari's³⁴ report, due to difference of surface energy, the basal polar facets have higher growth rates than the lateral nonpolar facets. Furthermore, nanorods with wurtzite structure are composed of repeating Cd and Se (or S) lattice planes along the (00 ℓ) direction. It is believed that the reactivity is higher on the tip ended up with anion rich facets than that with cation rich facets, which thus offers an opportunity for selective chemistry on different facets. As a consequence, during growth of Pt nanoparticles, low Pt concentration or at the early stage of reaction could lead to



growth on Se (or S) rich facets more easily. Therefore, by controlling the reaction time interval and Pt concentration, matchstick structured Pt-CdSe nanorods could be obtained. Crystallinity of Pt nanoparticles and CdSe nanorods could be evaluated from high resolution transmission electron microscope (HRTEM) image. As shown in Figure 2b, d-spacing along the long axis of nanocrystals is measured as 0.35 nm, attributed to {002} planes of wurtzite structured CdSe, and the d-spacing of the dark nanoparticles is calculated as 0.23 nm, corresponding to {111} facets in face-centered cubic platinum. Note that the angle between lattice planes of Pt and CdSe nanocrystals varies from each hybrid nanorod, indicating that there is no preferred orientation of {111} planes of Pt with respect to {002} facets of CdSe nanorods. In addition, as shown in insert of Figure 2b, selected area X-ray energy dispersive spectroscopy (EDS) performed on three distinct Pt-CdSe nanorods in Figure 2b indicates the appearance of Pt and CdSe composition.

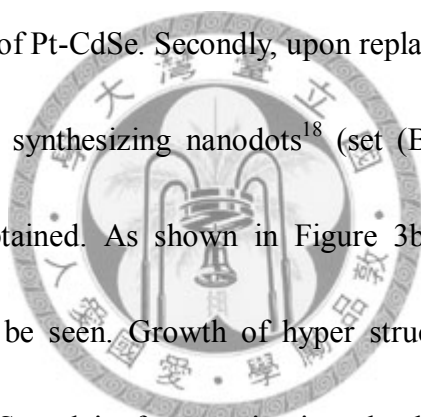
After obtaining matchstick structured hybrid Pt-CdSe nanorods, the challenging issue thereby lies on the growth of the second segment. Axial heterostructured nanorods and nanowires in solution phase are reported by acquiring solution-liquid-solid mechanism^{39,40,48,53,55} or multiple injection method^{13,26,37,38,48,49} until present time. Since Pt nanoparticles would not be suitable for serving as catalytic droplets, in this report, second segment would not grow from site in between the Pt and CdSe (a typical

appearance of SLS mechanism). On the other hand, in multiple injection method, growth of the second composition occurs simultaneously at both tips of CdSe nanorods, thus excluding the chance from being applied in the field of nano p-n junction. Herein we propose a conceptual design, being in a manner different from SLS mechanism and multiple injection method, in which a second segment (CdS nanorod) would grow from the unprotected tip of a Pt-CdSe nanorod. This concept, in combination with traditional methodology of chemical synthesis, could set a good example of rational design in nano architecture.



Starting from the growth mechanism of anisotropic CdSe nanocrystals constructed by Peng's group,¹⁴ Growth of a nanorod is divided into two steps, nucleation and shape evolution. At the stage of nucleation, presence of "magic-sized seeds" occurs at high chemical potential by maintaining high monomer concentration, which is necessary in producing anisotropic semiconducting nanocrystals. Altering the chemical potential as well as the reactivity could be easily achieved by simply changing the type of surfactants. Therefore, chemical potential of the current system, containing Pt-CdSe and precursor for growing a second segment, should be high enough to initiate 1D growth, and more importantly, should be in the same level of reactivity at the unprotected tip of Pt-CdSe nanocrystals. To fulfill the above mentioned statement, firstly, a typical set of surfactants for growing CdS nanorods,⁵⁶ tetradecylphosphonic acid (TDPA) and

trioctylphosphine (TOP), was used. By injection the mixture containing sulfur, TOP, and Pt-CdSe nanorods into stock solution at 320 °C, denoted as (A) set in experimental section, the corresponding result of TEM image is shown in Figure 3a. CdS nanorods are formed without any connection to Pt-CdSe nanocrystals, which means that during CdS growth, difference of chemical potential between precursor for growing CdS and diffusion sphere¹⁴ surrounding the Pt-CdSe nanorods is so large that growth of CdS nanorods occurs outside the diffusion sphere. That is, CdS nanorods grow themselves by neglecting the presence of Pt-CdSe. Secondly, upon replacing TDPA with stearic acid, a traditional surfactant for synthesizing nanodots¹⁸ (set (B) in experimental section), very different result is obtained. As shown in Figure 3b, apparently, whiskers and branched structures could be seen. Growth of hyper structures refers to that during initial stage of reaction, CdS nuclei, after entering into the diffusion sphere, tend to start one dimensional growth at the unblocked tip and at surface along longitudinal direction of CdSe nanorods, regardless of the difference of reactivity between short and long axis of Pt-CdSe. In addition, it should be noted that most of the hierarchical structures in Figure 3b are still anisotropic, indicating the chemical potential of CdS precursor is still in the range of 1D growth. Figure 3a and 3b show two extremes of growing heterojunction nanocrystals. That is, in the case of TDPA and TOP (set A), surface of Pt-CdSe nanorods might be covered thoroughly by surfactants, hence hindering the



growth of second segment. On the other hand, while applying stearic acid and TOP as surfactants (set (B)), the adsorption of surfactants on Pt-CdSe might be too weak to protect the surface of nanorods, thus the hyper-branched structure is produced.

In the aim of tuning reactivity of monomers, previous reports conclude that noncoordinating solvent, namely octadecene (ODE), might serve as an excellent candidate.^{22,25} By simply adjusting the oleic acid/ODE ratio in reaction, high quality nanocrystals could be obtained.²² Accordingly, we tentatively choosed noncoordinating solvent (set (C) in experimental section) for synthesis of CdS nanocrystals on unprotected tip of Pt-CdSe nanorods, and the result is encouraging. As shown in Figure 4a, axial heterostructured Pt-CdSe-CdS nanorods are observed. Comparing the dimension with Pt-CdSe in Figure 2a, increase of length of Pt-CdSe-CdS nanorods is around 10 ~ 15 nm, indicating the anisotropic growth of CdS nanorods on Pt-CdSe nanocrystals. In addition, a slight increase of the diameter (~ 1 nm) is monitored, possibly due to a few monolayers of CdS grown on the side of Pt-CdSe nanorods, which will be discussed later. The other evidence of the axial heterojunction is the absorption spectra (Figure 4b). From Figure 4b, the 670 nm absorption of CdSe still remains unchanged after the reaction of synthesizing Pt-CdSe and Pt-CdSe-CdS, and a new 450 nm absorption band is recognized, corresponding to the band edge of CdS nanocrystals.⁵⁷ Apparently, from absorption experiments, except for CdSe and CdS

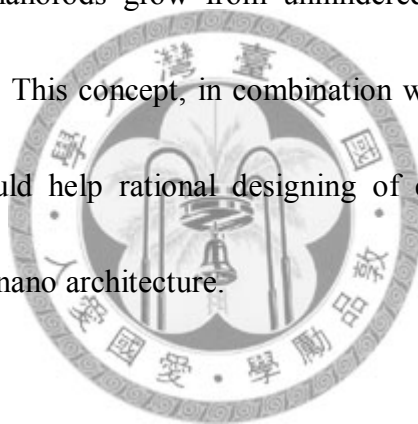
nanocrystals, there is no existence of any other composition produced, such as alloy of CdSe and CdS, in the reaction.

To gain further detailed structural information, HRTEM measurements were performed. Figure 5a shows a HRTEM image of a Pt-CdSe-CdS heterostructured nanorod synthesized by using oleic acid, ODE, and TOP as surfactants. It could be seen that the length of the newly formed CdS nanorods is ~ 15 nm, and the d-spacing is calculated as 0.33 nm, owing to the {002} facets hexagonal CdS. Stacking faults are observed at the interface between the two materials, which might be due to lattice mismatch and fast growth along the c-axis of nanorods. Results of selected area EDS for the site near Pt end (head) and CdS end (tail) of the Pt-CdSe-CdS nanorod are shown in the lower-right and upper-left part of Figure 5a, respectively. The tail part exhibits only the appearance of Cd and S, while the head part reveals the composition of Pt, Cd, Se, and S. In order to view the exact position of sulfur on head part, and to confirm chemically that the Pt-CdSe-CdS nanorods are made up of separate segments of CdSe and CdS, images of electron energy-loss spectroscopy (EELS) were taken. The appearance of Cd, Se, and S could therefore be determined under the respective absorption edges and energy windows (see experimental section). As shown in Figure 5b and 5c, distinct signals of Se and S are clearly monitored, suggesting the axial heterojunction of CdSe and CdS. On the other hand, there seems to be a layer of CdS on

the outer shell of the CdSe nanorod. Combining the results of HRTEM, EDS, and EELS mentioned above, we tentatively propose that upon applying noncoordinating solvents in the system, axial heterostructured Pt-CdSe-CdS nanorods could be synthesized by adjusting the reactivity of monomers. During the reaction, unprotected surfaces of CdSe serve as a template. After the initial stage, namely the nucleation, CdS nuclei are embedded on the unblocked tip and lateral surface of CdSe. CdS precursors at high chemical potential enter the diffusion sphere, and subsequently start fast one dimensional growth from the unprotected end of CdSe. Because of identical wurtzite structure between the two materials, the resultant c-axis of CdSe and that of newly formed CdS nanorods are in the same direction. Relative slow growth on lateral surfaces produces a thin layer of CdS coating on the Pt-CdSe nanorods, which is also pointed out in previous reports about heterojunctions synthesized by using multiple injection method.^{26,55,58} Moreover, increasing time duration for reaction would drive the formation of nanocrystals from 1-D to 3-D growth, and further, to ripening process.¹⁴ We thus extended reaction time from 5 minutes to 1 hour, and the corresponding TEM image is shown in Figure 6. Interestingly, diameter of nanorods increases drastically while the variation of length along long axis is quite small, indicating that growth of axial heterostructured Pt-CdSe-CdS nanorods could be rationalized by the well-known mechanism for growing anisotropic nanorods.^{13-15,23}

4. Conclusion

In summary, based on a conceptual design, axial heterostructured Pt-CdSe-CdS semiconducting nanorods are reported. The role of Pt nanoparticles in matchstick structured Pt-CdSe nanorods is viewed as protecting agents, which allows the selective synthesis on the unblocked tip. In addition, tuning the reactivity of CdS precursors could be fulfilled by employing noncoordinating solvents in reaction. As a result, second segment of CdS nanorods grow from unhindered site, and hence the axial heterostructure is obtained. This concept, in combination with traditional methodology of chemical synthesis, could help rational designing of complex nanomaterials and nanodevices in the field of nano architecture.



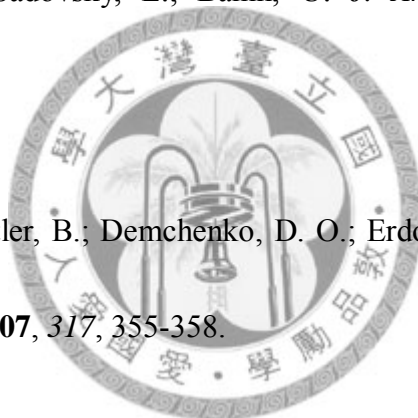
5. References

- (1) Brus, L. E. *J. Chem. Phys.* **1984**, *80*, 4403-4409.
- (2) Murray, C. B.; Norris, D. J.; Bawendi, M. G. *J. Am. Chem. Soc.* **1993**, *115*, 8706-8715.
- (3) Alivisatos, A. P. *J. Phys. Chem.* **1996**, *100*, 13226-13239.
- (4) Alivisatos, A. P. *Science* **1996**, *271*, 933-937.

- (5) Markovich, G.; Collier, C. P.; Henrichs, S. E.; Remacle, F.; Levine, R. D.; Heath, J. R. *Acc. Chem. Res.* **1999**, *32*, 415-423.
- (6) Klimov, V. I.; Mikhailovsky, A. A.; Xu, S.; Malko, A.; Hollingsworth, J. A.; Leatherdale, C. A.; Eisler, H. J.; Bawendi, M. G. *Science* **2000**, *290*, 314-317.
- (7) Tessler, N.; Medvedev, V.; Kazes, M.; Kan, S. H.; Banin, U. *Science* **2002**, *295*, 1506-1508.
- (8) Bakueva, L.; Musikhin, S.; Hines, M. A.; Chang, T. W. F.; Tzolov, M.; Scholes, G. D.; Sargent, E. H. *Appl. Phys. Lett.* **2003**, *82*, 2895-2897.
- (9) Huynh, W. U.; Dittmer, J. J.; Alivisatos, A. P. *Science* **2002**, *295*, 2425-2427.
- (10) McDonald, S. A.; Konstantatos, G.; Zhang, S.; Cyr, P. W.; Klem, E. J. D.; Levina, L.; Sargent, E. H. *Nat. Mater.* **2005**, *4*, 138-142.
- (11) Duan, X. F.; Huang, Y.; Cui, Y.; Wang, J. F.; Lieber, C. M. *Nature* **2001**, *409*, 66-69.
- (12) Gudiksen, M. S.; Lauhon, L. J.; Wang, J. F.; Smith, D.; Lieber, C. M. *Nature* **2002**, *415*, 617-620.
- (13) Manna, L.; Scher, E. C.; Alivisatos, A. P. *J. Am. Chem. Soc.* **2000**, *122*, 12700-12706.
- (14) Peng, Z. A.; Peng, X. G. *J. Am. Chem. Soc.* **2001**, *123*, 1389-1395.

- (15) Peng, Z. A.; Peng, X. G. *J. Am. Chem. Soc.* **2001**, *123*, 183-184.
- (16) Jun, Y. W.; Lee, S. M.; Kang, N. J.; Cheon, J. W. *J. Am. Chem. Soc.* **2001**, *123*, 5150-5151.
- (17) Li, L. S.; Hu, J. T.; Yang, W. D.; Alivisatos, A. P. *Nano Lett.* **2001**, *1*, 349-351.
- (18) Qu, L. H.; Peng, Z. A.; Peng, X. G. *Nano Lett.* **2001**, *1*, 333-337.
- (19) Qu, L. H.; Peng, X. G. *J. Am. Chem. Soc.* **2002**, *124*, 2049-2055.
- (20) Peng, Z. A.; Peng, X. G. *J. Am. Chem. Soc.* **2002**, *124*, 3343-3353.
- (21) Manna, L.; Scher, E. C.; Li, L. S.; Alivisatos, A. P. *J. Am. Chem. Soc.* **2002**, *124*, 7136-7145.
- (22) Yu, W. W.; Peng, X. G. *Angew. Chem. Int. Ed.* **2002**, *41*, 2368-2371.
- (23) Peng, X. G. *Adv. Mater.* **2003**, *15*, 459-463.
- (24) Mokari, T.; Banin, U. *Chem. Mater.* **2003**, *15*, 3955-3960.
- (25) Yu, W. W.; Wang, Y. A.; Peng, X. G. *Chem. Mater.* **2003**, *15*, 4300-4308.
- (26) Milliron, D. J.; Hughes, S. M.; Cui, Y.; Manna, L.; Li, J.; Wang, L. W.; Alivisatos, A. P. *Nature* **2004**, *430*, 190-195.
- (27) Qu, L. H.; Yu, W. W.; Peng, X. G. *Nano Lett.* **2004**, *4*, 465-469.
- (28) Shieh, F.; Saunders, A. E.; Korgel, B. A. *J. Phys. Chem. B* **2005**, *109*, 8538-8542.

- (29) Kumar, S.; Nann, T. *Small* **2006**, *2*, 316-329.
- (30) Mokari, T.; Rothenberg, E.; Popov, I.; Costi, R.; Banin, U. *Science* **2004**, *304*, 1787-1790.
- (31) Mokari, T.; Sztrum, C. G.; Salant, A.; Rabani, E.; Banin, U. *Nat. Mater.* **2005**, *4*, 855-863.
- (32) Salant, A.; Amitay-Sadovsky, E.; Banin, U. *J. Am. Chem. Soc.* **2006**, *128*, 10006-10007.
- (33) Robinson, R. D.; Sadtler, B.; Demchenko, D. O.; Erdonmez, C. K.; Wang, L. W.; Alivisatos, A. P. *Science* **2007**, *317*, 355-358.
- (34) Habas, S. E.; Yang, P.; Mokari, T. *J. Am. Chem. Soc.* **2008**, *130*, 3294-3295.
- (35) Figuerola, A.; Franchini, I. R.; Fiore, A.; Mastria, R.; Falqui, A.; Bertoni, G.; Bals, S.; Tendeloo, G. V.; Kudera, S.; Cingolani, R.; Manna, L. *Adv. Mater.* **2008**, *20*, 1-5.
- (36) Kudera, S.; Carbone, L.; Casula, M. F.; Cingolani, R.; Falqui, A.; Snoeck, E.; Parak, W. J.; Manna, L. *Nano Lett.* **2005**, *5*, 445-449.
- (37) Shieh, F.; Saunders, A. E.; Korgel, B. A. *J. Phys. Chem. B* **2005**, *109*, 8538-8542.



(38) Saunders, A. E.; Koo, B.; Wang, X.; Shin, C. K.; Korgel, B. A. *ChemPhysChem* **2008**, *9*, 1158-1163.

(39) Ouyang, L.; Maher, K. N.; Yu, C. L.; McCarty, J.; Park, H. *J. Am. Chem. Soc.* **2007**, *129*, 133-138.

(40) Dong, A.; Wang, F.; Daulton, T. L.; Buhro, W. E. *Nano Lett.* **2007**, *7*, 1308–1313.

(41) Dong, A.; Tang, R.; Buhro, W. E. *J. Am. Chem. Soc.* **2007**, *129*, 12254–12262.

(42) Carbone, L.; Nobile, C.; Giorgi, M. D.; Sala, F. D.; Morello, G.; Pompa, P.; Hych, M.; Snoeck, E.; Fiore, A.; Franchini, I. R.; Nadasan, M.; Silvestre, A. F.; Chiodo, L.; Kudera, S.; Cingolani, R.; Krahn, R.; Manna, L. *Nano Lett.* **2007**, *7*, 2942-2950.



(43) Talapin, D. V.; Nelson, J. H.; Shevchenko, E. V.; Aloni, S.; Sadtler, B.; Alivisatos, A. *Nano Lett.* **2007**, *7*, 2951-2959.

(44) Hewa-Kasakarage, N. N.; Kirsanova, M.; Nemchinov, A.; Schmall, N.; El-Khoury, P. Z.; Tarnovsky, A. N.; Zamkov, M. *J. Am. Chem. Soc.* **2009**, *131*, 1328–1334.

(45) Zhong, H.; Scholes, G. D. *J. Am. Chem. Soc.* **2009**, *131*, 9170–9171.

(46) Dorfs, D.; Salant, A.; Popov, I.; Banin, U. *Small* **2008**, *4*, 1319-1323.

(47) Menagen, G.; Mocatta, D.; Salant, A.; Popov, I.; Dorfs, D.; Banin, U. *Chem. Mater.* **2008**, *20*, 6900-6902.

(48) Kumar, S.; Jones, M.; Lo, S. S.; Scholes, G. D. *Small* **2007**, *3*, 1633-1639.

(49) He, J.; Lo, S. S.; Kim, J.; Scholes, G. D. *Nano Lett.* **2008**, *8*, 4007-4013.

(50) Fiore, A.; Mastria, R.; Lupu, M. G.; Lanzani, G.; Giannini, C.; Carlino, E.; Morello, G. Giorgi, M. D.; Li, Y.; Cingolani, R.; Manna, L. *J. Am. Chem. Soc.* **2009**, *131*, 2274-2282.

(51) Manna, L.; Scher, E. C.; Alivisatos, A. P. *J. Am. Chem. Soc.* **2000**, *122*, 12700-12706.



(52) Peng, Z. A.; Peng, X. G. *J. Am. Chem. Soc.* **2002**, *124*, 3343-3353.

(53) Wang, F.; Dong, A.; Sun, J.; Tang, R.; Yu, H.; Buhro, W. E. *Inorg. Chem.* **2006**, *45*, 7511-7521.

(54) Kan, S.; Mokari, T.; Rothenberg, T.; Banin, U. *Nat. Mater.* **2003**, *2*, 155-158.

(55) Xi, L.; Boothroyd, C.; Lam, Y. M. *Chem. Mater.* **2009**, *21*, 1465-1470.

(56) Kang, C. C.; Lai, C. W.; Peng, H. C.; Shyue, J. J.; Chou, P. T. *ACS Nano* **2008**, *2*,

750-756.

(57) Kang, C. C.; Lai, C. W.; Peng, H. C.; Shyue, J. J.; Chou, P. T. *Small* **2007**, 3, 1882-1885.

(58) Koo, B.; Korgel, B. A. *Nano Lett.* **2008**, 8, 2490-2496.



Figure 1

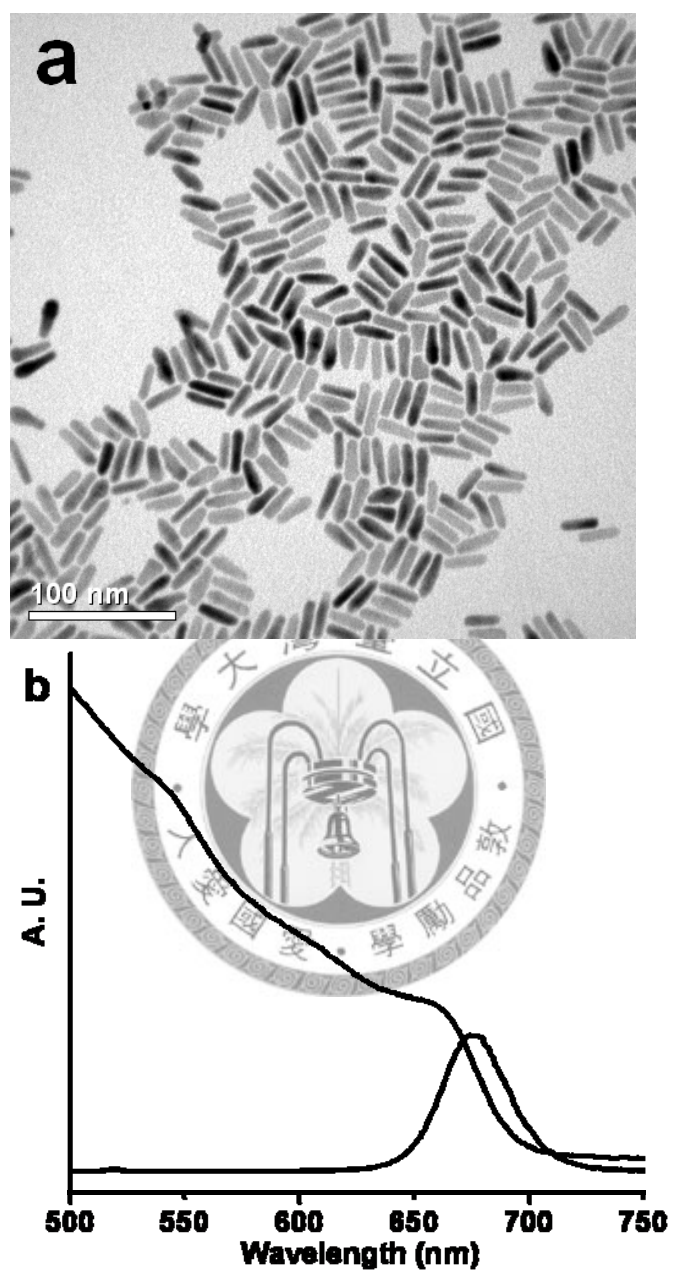


Figure 1. (a) TEM image and (b) UV/Vis steady-state absorption and emission spectra of CdSe nanocrystals.

Figure 2

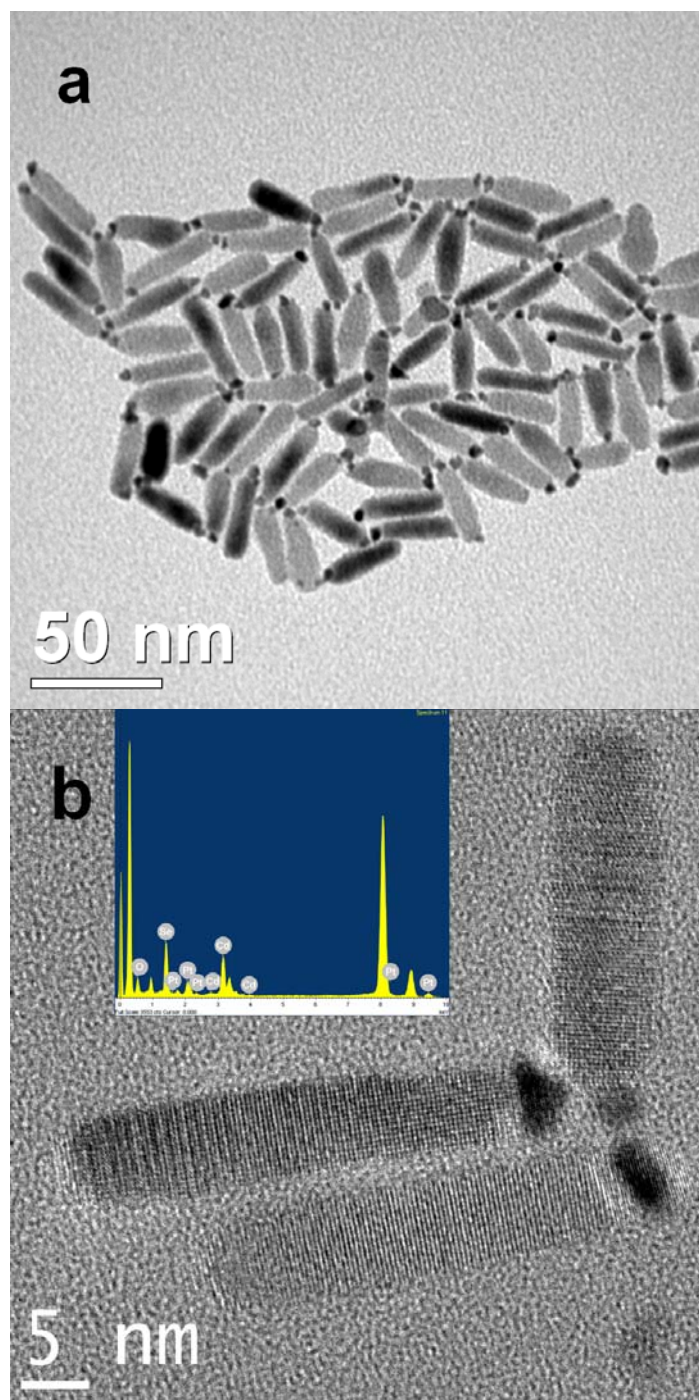


Figure 2. (a) TEM image and (b) HRTEM image of Pt-CdSe nanocrystals. (inset: selected area EDS spectrum of this image.)

Figure 3

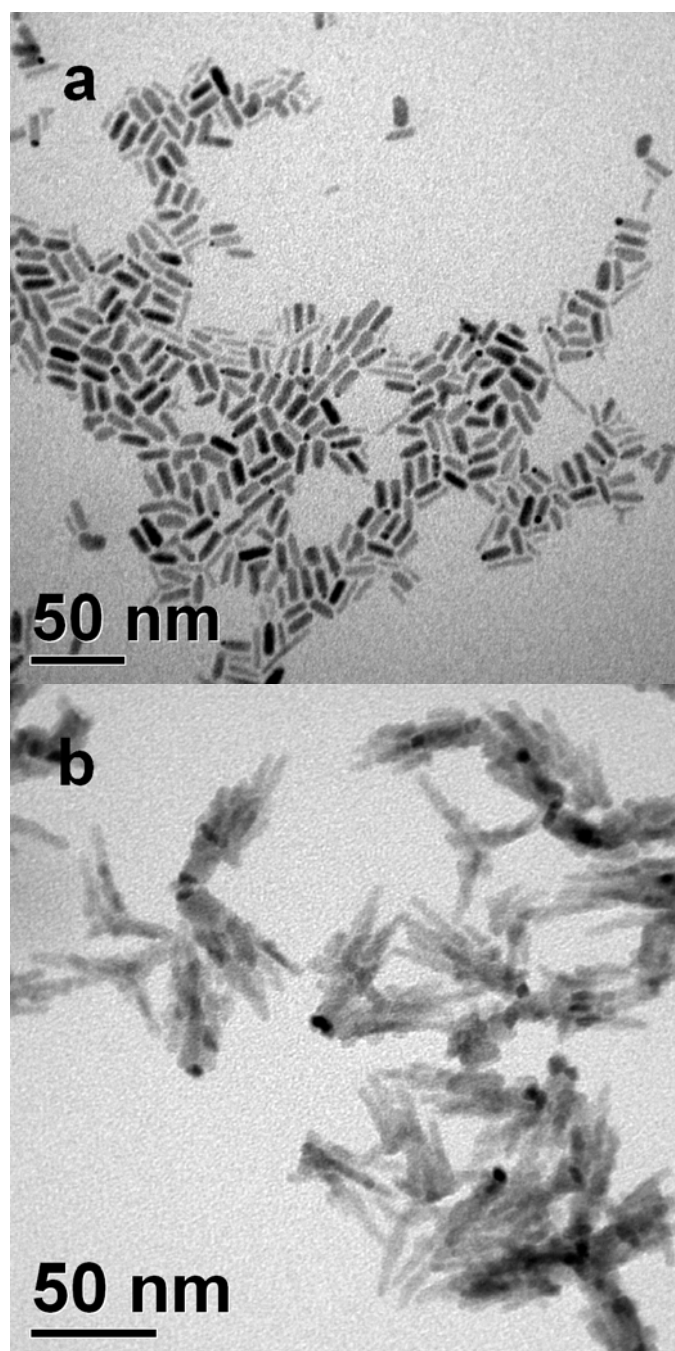


Figure 3. TEM images of nanocrystals synthesized by using (a) TDPA, and TOP. (b) stearic acid and TOP.

Figure 4

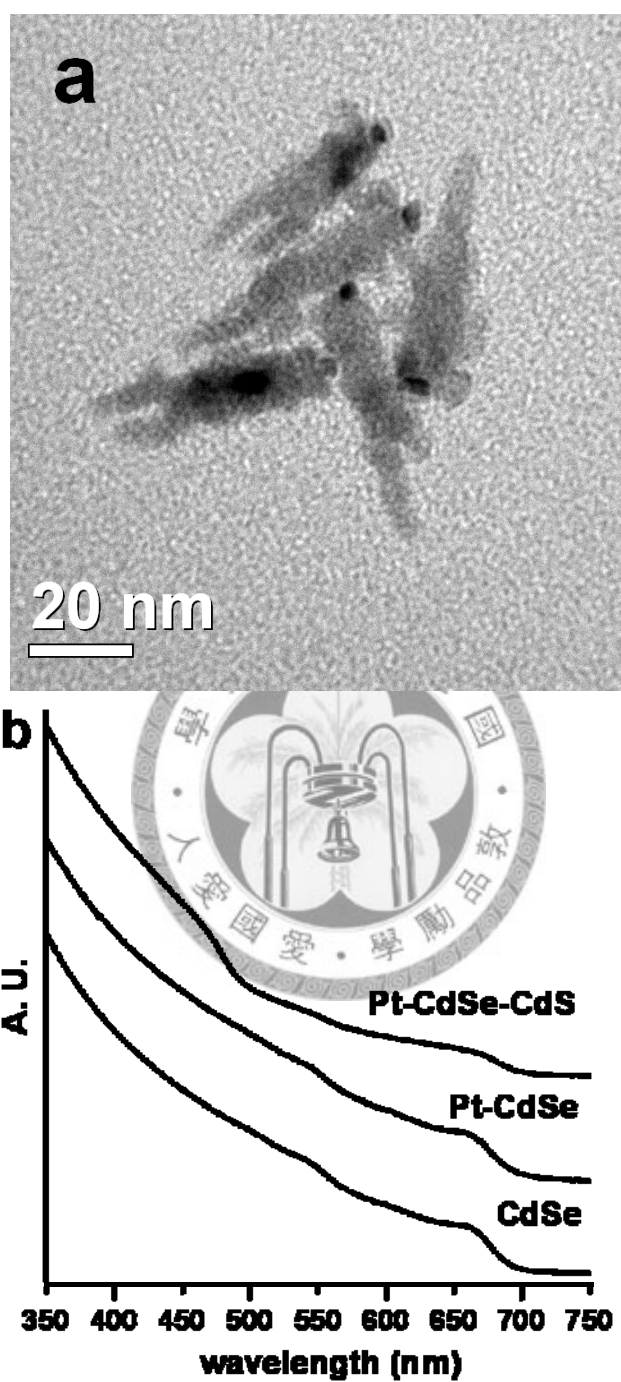


Figure 4. (a) TEM image of Pt-CdSe-CdS nanocrystals synthesized by using oleic acid, ODE, and TOP. (b) UV/Vis steady-state absorption spectra of CdSe, Pt-CdSe, and Pt-CdSe-CdS nanocrystals.

Figure 5

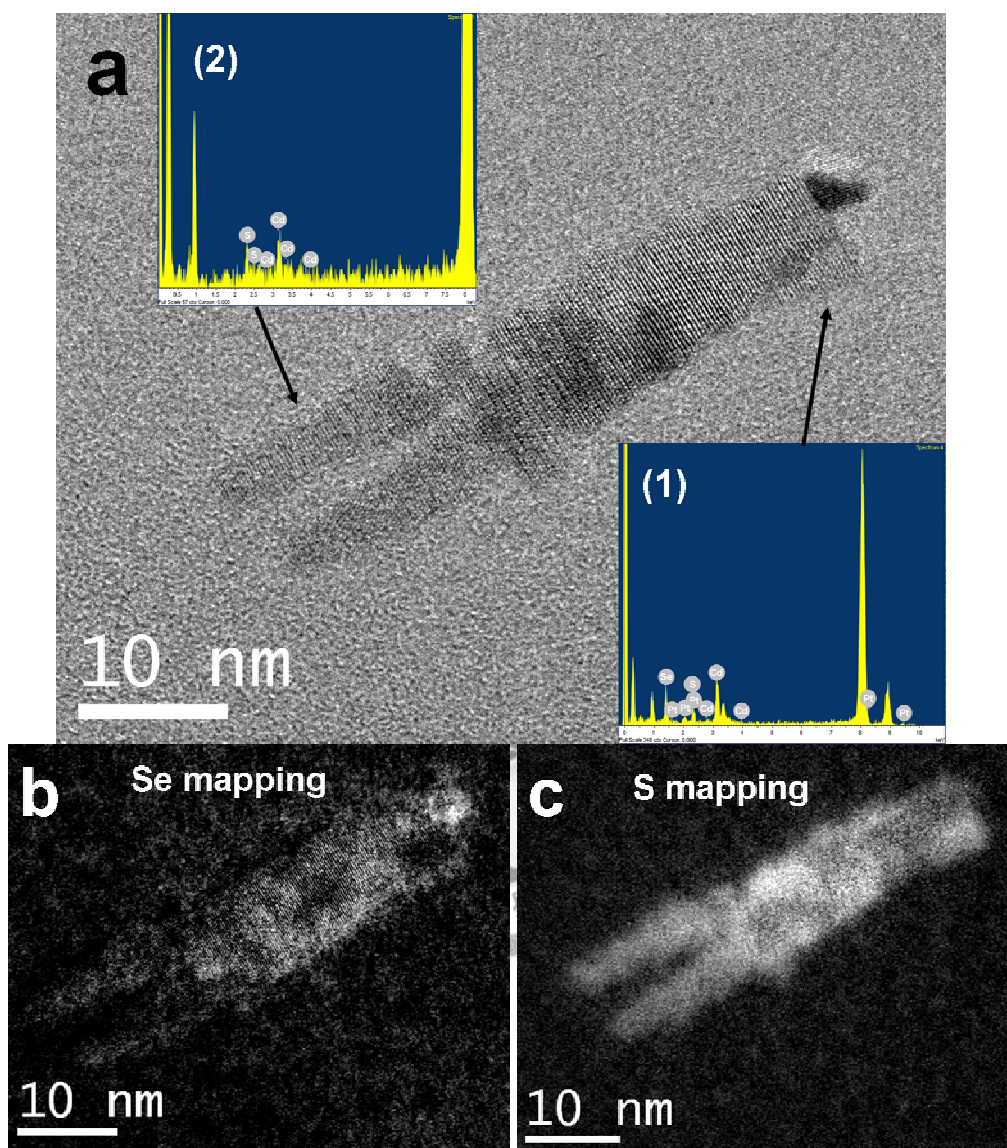


Figure 5. (a) HRTEM image of a Pt-CdSe-CdS heterostructured nanorod synthesized by using oleic acid, ODE, and TOP as surfactants. The inset shows EDS results of (1) head and (2) tail part of the hybrid nanorod. (b) Se and (c) S mapping done by using EELS measurements.

Figure 6

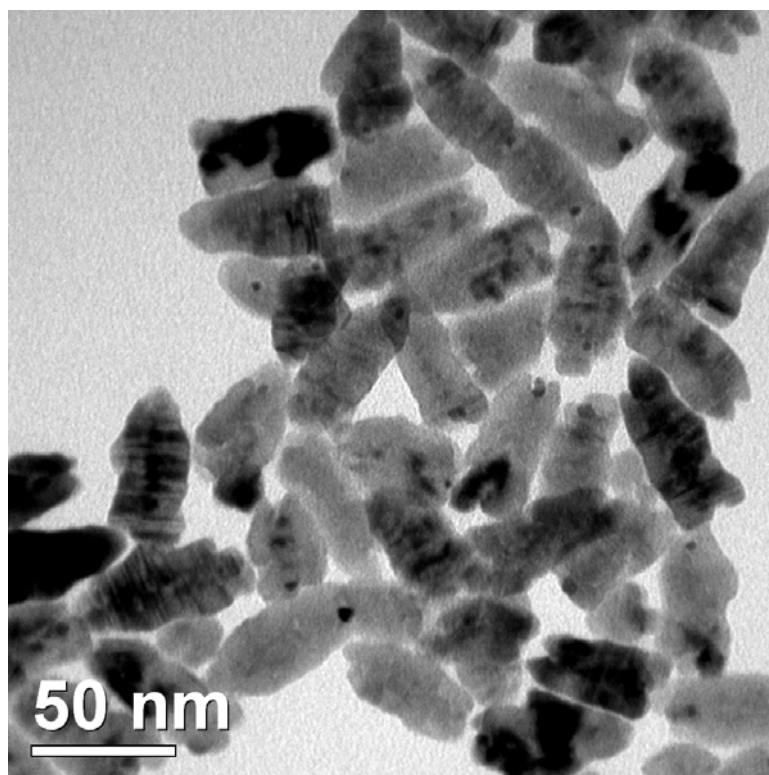


Figure 6. TEM image of Pt-CdSe-CdS nanocrystals synthesized by using oleic acid, ODE, and TOP for 1 hour.

Chapter 6.

Concluding Remarks

In summary, from growth mechanism and methodology of anisotropic nanorods, tuning the morphology of CdS nanocrystals is achieved. Exclusive self-assemblies of TDPA and TOP capped CdS nanorods in the absence of external direction-controlling processes (e.g., external electric field, polymer matrix, or highly oriented pyrolytic carbon) are reported. With concentration higher than 2.0 % weight percent in toluene, the as-prepared CdS nanorods start to corral together. Self-assemblies with outer edges of leaning bundles and an inner part of hexagonal packing perpendicular to the substrate are thus formed with the assistance of the hydrocarbon chains on surfactants or the interactions among nanorods. In addition, by optimizing the type of surfactants and temperature of reaction, CdS nanowires with aspect ratio up to 300 could be obtained. Experimental results imply that the selective-adsorption mechanism could be extended to explain the formation of semiconductor nanowires. Furthermore, a new conceptual design by introducing the protecting agent into the synthesis of semiconducting nanorods has been proposed. By employing noncoordinating solvents, axial heterostructured Pt-CdSe-CdS semiconducting nanorods could be fabricated. The role of Pt nanoparticles in match stick structured Pt-CdSe nanorods is viewed as protecting

agents, which allows the selective synthesis on the unblocked tip. The results and discussion in this report could help developing the complex nanomaterials and nanodevices in the field of nano architecture, which could be extended to applications in nanoscience and nanotechnology.

